

PROBING SINGLE-PARTICLE STRUCTURE NEAR THE ISLAND  
OF INVERSION BY DIRECT NEUTRON KNOCKOUT FROM  
INTERMEDIATE-ENERGY BEAMS OF  $^{26,28}\text{Ne}$  AND  $^{30,32}\text{Mg}$

By

James Russell Terry

A DISSERTATION

Submitted to  
Michigan State University  
in partial fulfillment of the requirements  
for the degree of

DOCTOR OF PHILOSOPHY

Department of Physics and Astronomy

2006

# ABSTRACT

PROBING SINGLE PARTICLE STRUCTURE NEAR THE ISLAND OF  
INVERSION BY DIRECT NEUTRON KNOCKOUT FROM  
INTERMEDIATE-ENERGY BEAMS OF  $^{26,28}\text{Ne}$  AND  $^{30,32}\text{Mg}$

By

James Russell Terry

Nuclear shell structure is observed to evolve with increasing proton-neutron asymmetry, leading to the weakening of magic numbers well-established for stable nuclei and the appearance of new shell gaps. A typical example is given by the neutron-rich region between the oxygen and magnesium isotopes where the  $N = 20$  magic number is broken at  $^{32}\text{Mg}$  and a new shell gap arises at  $N = 16$ . Modern large-scale shell model calculations employing the new SDPF-M effective interaction, which is valid for a broad range of nuclei in this region, propose a mechanism in which a number of nuclear structure phenomena are well reproduced. A transitional region of nuclei in which the  $N = 20$  magic number weakens is suggested to exist between the  $N = 16$  and  $N = 20$  isotones.

Nucleon knockout reactions from intermediate-energy ion beams are well suited for probing the single-particle structure of exotic nuclei. Results are presented from the single-neutron knockout measurement from  $^{26,28}\text{Ne}$  and  $^{30,32}\text{Mg}$ . These nuclei lie in the proposed transitional region between the neutron-rich  $N = 16$  and  $N = 20$  isotones. While no evidence of a broken  $N = 20$  magic number is found for  $^{26}\text{Ne}$ , negative parity states in the  $^{27}\text{Ne}$  and  $^{29,31}\text{Mg}$  knockout residues are populated, yielding direct evidence of negative-parity intruder configurations in the ground states of  $^{28}\text{Ne}$  and  $^{30,32}\text{Mg}$ . Spectroscopic strengths to these negative parity states are deduced and found to be in good agreement with predicted single-particle occupancies, confirming the predictive power of SDPF-M calculations in this region.

## ACKNOWLEDGMENTS

There are quite a large number of individuals and groups to which I owe gratitude for support in completing this dissertation project. I would first like to thank my advisor P. Gregers Hansen for providing the opportunity to be involved in his research program and for sharing his enthusiasm for nuclear physics with me. The conception and development of this project greatly benefited from the many hours he contributed in thought, conversation, and effort. I would also like to thank Thomas Glasmacher for the opportunity to work with the Segmented Germanium Array and to be involved with a number of experiments at the NSCL. I would like to acknowledge his aid in the execution and completion of this dissertation project and for taking on advisory responsibilities during the last year. Also, I would like to thank Alexandra Gade for aid with the analysis and interpretation of measurements presented in this dissertation.

I would like to thank Gregers Hansen and Joachim Enders for allowing me to be involved in the execution and analysis of knockout measurements early in my time at the NSCL. The neutron knockout measurement from  $^{26}\text{Ne}$  was performed as part of an experiment proposed by Gregers and Joachim, and the experience in performing this measurement and analyzing the data was pivotal for the conception and proposal of the subsequent  $^{28}\text{Ne}$  and  $^{30,32}\text{Mg}$  measurements.

The measurements included in this project required a number of devices at the National Superconducting Cyclotron Laboratory, and I would like to acknowledge the lab as a whole for providing the infrastructure necessary to perform these measurements. I would like to thank the Coupled-Cyclotron Facility staff for the high-intensity primary beams provided for a number of measurements included in this work. I would also like to thank the A1900 group, and specifically the A1900 contact for experiment 02025 Thomas Baumann, for development and delivery of the secondary beams. I would like to acknowledge the support of the S800 staff: Daniel Bazin, Alexandra

Gade, and Ken Yoneda, and would also like to acknowledge the support of the SeGA staff physicist Wil Mueller and the entire Gamma group: Chris Campbell, Jennifer Church, Jon Cook, Dan-Cristian Dinca, Joachim Enders, Alexandra Gade, Thomas Glasmacher, Zhiqiang Hu, Ben Perry, Katie Yurkewicz, and Heather Zwahlen. I would also like to acknowledge the help of Andrew Davies and Jean-Luc Lecouey for their help with the setup and execution of the experiment.

Data analysis of the  $^{26}\text{Ne}$  data greatly benefited from collaboration with Jean-Luc Lecouey, Gregers Hansen, and Brad Sherrill. Analysis of the subsequent measurements presented here benefited greatly from collaboration with Daniel Bazin, Matt Bowen, Chris Campbell, Jon Cook, Dan-Cristian Dinca, Alexandra Gade, Thomas Glasmacher, Gregers Hansen, Brad Sherrill, and Heather Zwahlen. I would like to thank Jeff Tostevin for providing the reaction theory for interpreting results from these knockout reactions. Interpretation of the results as a whole includes a comparison with shell model calculations for which I would like to acknowledge the support of Alex Brown as well as Takaharu Otsuka and Yutaka Utsuno.

I would also like to acknowledge the support of my guidance committee: Alex Brown, Mark Dykman, Bernard Pope, and Brad Sherrill along with Gregers Hansen and Thomas Glasmacher. Their guidance was important in shaping the execution, analysis, and interpretation of measurements included in this dissertation.

# Contents

<b>1</b>	<b>Introduction</b>	<b>1</b>
1.1	The Nucleus . . . . .	1
1.2	Magic Numbers and Shell Structure . . . . .	3
1.3	The Nuclear Shell Model . . . . .	4
1.4	Nuclear Structure of Neutron-Rich Nuclei Between N=16 and N=20 . . . . .	8
1.5	Shell Model Predictions for $^{26,28}\text{Ne}$ and $^{30,32}\text{Mg}$ . . . . .	11
1.6	Nucleon Knockout Reactions . . . . .	16
1.6.1	Eikonal Reaction Model for Knockout . . . . .	18
1.6.2	Calculated Unit Cross Sections and Momentum Distributions . . . . .	21
1.6.3	Example Case: Single-Neutron Knockout from $^{12}\text{Be}$ . . . . .	25
<b>2</b>	<b>Method</b>	<b>26</b>
2.1	Overview of Technique . . . . .	26
2.2	Radioactive Ion Beam Production . . . . .	29
2.2.1	Primary Beam . . . . .	30
2.2.2	Fragmentation . . . . .	30
2.2.3	Fragment Separation . . . . .	31
2.3	Experimental Device and Detector Setup . . . . .	31
2.3.1	The S800 Spectrograph . . . . .	32
2.3.2	Segmented Germanium Array (SeGA) . . . . .	39
2.4	Data Acquisition Trigger . . . . .	52
2.4.1	Normalization of $\gamma$ -Ray Intensities . . . . .	53
<b>3</b>	<b>Analysis and Experimental Results</b>	<b>54</b>
3.1	Single-Neutron Removal Data from $^{26}\text{Ne}$ . . . . .	54
3.1.1	Inclusive Cross Section . . . . .	54
3.1.2	Gamma-Ray Analysis . . . . .	54
3.1.3	Longitudinal Momentum Distributions . . . . .	56
3.2	Single-Neutron Removal Data from $^{28}\text{Ne}$ . . . . .	57
3.2.1	Inclusive Cross Section . . . . .	57
3.2.2	Gamma-Ray Analysis . . . . .	58
3.2.3	Longitudinal Momentum Distributions . . . . .	62
3.3	Single-Neutron Knockout from $^{30}\text{Mg}$ . . . . .	64
3.3.1	Gamma-Ray Analysis . . . . .	64
3.3.2	Longitudinal Momentum Distributions . . . . .	72
3.4	Single-Neutron Knockout from $^{32}\text{Mg}$ . . . . .	76

3.4.1	Gamma-Ray Analysis . . . . .	77
3.4.2	Longitudinal Momentum Distribution . . . . .	82
<b>4</b>	<b>Discussion</b>	<b>85</b>
4.1	$^{26}\text{Ne}$ . . . . .	85
4.2	$^{28}\text{Ne}$ . . . . .	87
4.3	$^{30}\text{Mg}$ . . . . .	90
4.4	$^{32}\text{Mg}$ . . . . .	92
<b>5</b>	<b>Summary</b>	<b>96</b>
	<i>Bibliography</i>	<b>98</b>

# List of Figures

1.1	The Chart of Nuclides . . . . .	2
1.2	Single-particle energies for $^{34}\text{Si}$ . . . . .	7
1.3	Observed and calculated level scheme of $^{25}\text{Ne}$ . . . . .	12
1.4	Observed and calculated level scheme of $^{27}\text{Ne}$ . . . . .	13
1.5	Observed and calculated level scheme of $^{29,31}\text{Mg}$ . . . . .	15
1.6	Schematic of typical knockout reaction. . . . .	17
2.1	Schematic of the S800 Spectrograph . . . . .	32
2.2	Summary of corrected longitudinal momentum . . . . .	38
2.3	S800 acceptance window after $\theta_{Im}$ correction . . . . .	40
2.4	Schematic of SeGA crystal . . . . .	42
2.5	Measured photo-peak detection efficiency of SeGA. . . . .	46
2.6	Estimated SeGA energy resolution at 1.3 MeV . . . . .	48
2.7	Simulated SeGA energy resolution vs. half-life . . . . .	50
2.8	Ratio of simulated to measured photo-peak detection efficiency. . . . .	51
3.1	Run-by-run plot of $\sigma_{inc}$ for single-neutron knockout from $^{26}\text{Ne}$ . . . . .	55
3.2	Doppler-reconstructed $\gamma$ -ray energy spectrum for $^9\text{Be}(^{26}\text{Ne},^{25}\text{Ne})\text{X}$ . . . . .	56
3.3	Longitudinal momentum distributions for $^{25}\text{Ne}$ . . . . .	57
3.4	Beam and fragment rates for $^9\text{Be}(^{28}\text{Ne},^{27}\text{Ne})\text{X}$ $\sigma_{inc}$ measurement . . . . .	58
3.5	Gamma-ray energy spectrum in coincidence with $^{27}\text{Ne}$ . . . . .	59
3.6	Projections from $^{27}\text{Ne}$ $\gamma - \gamma$ matrix . . . . .	60
3.7	Momentum distributions for $^{27}\text{Ne}$ . . . . .	63
3.8	Fragment and beam rates for the single-neutron removal from $^{30}\text{Mg}$ . . . . .	65

3.9	Gamma-ray energy spectrum coincident with $^{29}\text{Mg}$ . . . . .	66
3.10	Observed $\gamma$ -ray transitions of $^{29}\text{Mg}$ . . . . .	69
3.11	Low-energy $\gamma$ -ray background from fragments collected with $^{29}\text{Mg}$ . .	71
3.12	Half-life measurement of 1.431-MeV states in $^{29}\text{Mg}$ . . . . .	73
3.13	Momentum distributions for $^{29}\text{Mg}$ . . . . .	74
3.14	Fragment and beam rates for $^9\text{Be}(^{32}\text{Mg}, ^{31}\text{Mg})\text{X}$ . . . . .	78
3.15	Gamma-ray spectrum for $^{31}\text{Mg}$ . . . . .	80
3.16	Observed $\gamma$ -ray transitions of $^{31}\text{Mg}$ . . . . .	81
3.17	Momentum distributions for $^{31}\text{Mg}$ . . . . .	83
4.1	Deduced and calculated level scheme for $^{27}\text{Ne}$ . . . . .	88
4.2	Longitudinal momentum distribution for events populating the ground state of $^{27}\text{Ne}$ . . . . .	90
4.3	Deduced and calculated low-energy level scheme for $^{29}\text{Mg}$ . . . . .	91
4.4	Deduced and calculated level scheme for $^{31}\text{Mg}$ . . . . .	94

# List of Tables

1.1	Neutron single-particle occupancies for $^{26}\text{Ne}$ . . . . .	12
1.2	Neutron single-particle occupancies for $^{28}\text{Ne}$ . . . . .	14
1.3	Neutron single-particle occupancies for $^{30,32}\text{Mg}$ . . . . .	14
1.4	Summary of calculated single-particle cross sections for neutron knock-out from $^{26,28}\text{Ne}$ . . . . .	23
1.5	Summary of calculated single-particle cross sections for neutron knock-out from $^{30,32}\text{Mg}$ . . . . .	24
1.6	Sensitivity of $\sigma_{sp}$ to parameters . . . . .	25
2.1	Summary of $\delta$ -SeGA Configuration . . . . .	41
2.2	Calibrated sources used to measure the photo-peak detection efficiency of SeGA. . . . .	45
2.3	Uncalibrated sources used to measure the photo-peak detection efficiency of SeGA. . . . .	45
3.1	Results for $^{26}\text{Ne}$ . . . . .	55
3.2	Results of $\gamma$ -ray analysis for $^{28}\text{Ne}$ . . . . .	61
3.3	Gamma-ray intensities and branching ratios for $^{29}\text{Mg}$ . . . . .	70
3.4	Contribution with $\gamma$ -ray gates from states populated in $^{29}\text{Mg}$ . . . . .	76
3.5	Gamma-ray intensities and branching ratios for $^{31}\text{Mg}$ . . . . .	82
4.1	Deduced and calculated spectroscopic factors and single-particle occupancies for $^{26}\text{Ne}$ . . . . .	86
4.2	Deduced and calculated spectroscopic factors and single-particle occupancies for $^{28}\text{Ne}$ . . . . .	87
4.3	Deduced spectroscopic strengths and calculated single-particle occupancies for $^{30}\text{Mg}$ . . . . .	93

4.4	Deduced spectroscopic factors and calculated single-particle occupancies for $^{32}\text{Mg}$ . . . . .	95
-----	---	----

# Chapter 1

## Introduction

### 1.1 The Nucleus

The atomic nucleus is comprised of positively charged protons and chargeless neutrons, referred to collectively as nucleons. Nuclear structure phenomena arise from three interactions: the strong, Coulomb, and weak forces. The strong force is a short-range but very strong interaction that binds nucleons together. The Coulomb interaction, while weaker than the strong force, introduces a long-range repulsion between the positively charged protons. Finally, the weak interaction provides a mechanism by which protons may transform into neutrons or vice versa. Ignoring the simplest nuclei like hydrogen, the nucleus is a quantum many-body system characterized by a length scale on the order of  $10^{-15}$  meters – approximately one million times smaller than the atom. However, whereas the level structure of electron states in the atom are determined externally from the well-understood Coulomb potential of the atomic nucleus, within the nucleus there is no external potential, and the constituents are strongly interacting through a force that is not well understood.

A nucleus  ${}^A_Z$  is referenced by both the number of protons  $Z$  and neutrons  $N$  and is often abbreviated as  ${}^A_Z$  or  $Z - A$ , where  $Z$  represents the chemical symbol and  $A = N + Z$  is the mass number, with  $N$  being the number of neutrons. For example

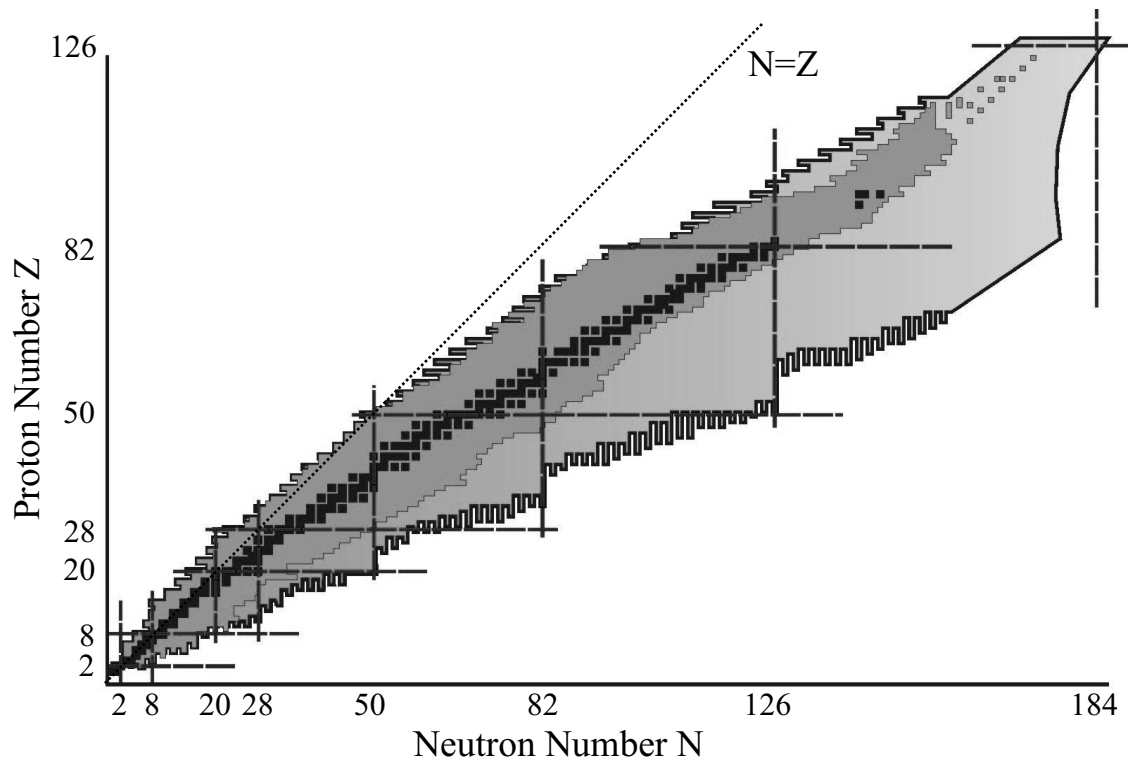


Figure 1.1: The Chart of Nuclides. The proton number  $Z$  increases from bottom to top, and neutron number  $N$  increases from left to right. Stable nuclei are shown in black while known and predicted unstable nuclei are shown respectively in dark and light grey. The  $N = Z$  line as well as the magic numbers are indicated on the figure.

the carbon nucleus with  $N = 6$  is represented by the symbol  $^{12}\text{C}$  or C-12. While  $Z$  defines the chemical identity of an element,  $N$  for a given element varies, and each specific value of  $N$  defines a separate isotope. Along these same lines, nuclei with a fixed  $N$  and with varying  $Z$  are referred to as isotones, while a set of nuclei with fixed  $A$  are referred to as isobars.

Similar to the periodic table for chemistry, nuclei are often arranged on a chart of nuclide, shown in figure 1.1, for which  $N$  increases horizontally from left to right and  $Z$  increases vertically from bottom to top. The geometry of the chart, as shown in figure 1.1 illustrates several important properties of the nuclear system. Only certain combinations of protons and neutrons are stable against radioactive decay. These nuclides are represented by the black boxes in the chart and lie in a region known as the “valley of stability.” The light and dark grey region beyond the valley of

stability represent measured and predicted unstable nuclei. Unstable nuclei consist of combinations of protons and neutrons which are bound but undergo exothermic radioactive reactions such as  $\beta$ - or  $\alpha$ -decay. The boundaries of the grey region in the chart represents the limits of nuclear binding known as the proton and neutron drip-lines for the respective proton-rich and neutron-rich sides of the chart. While the proton drip-line is completely delineated up to  $Z = 31$ , the neutron drip-line is only known up to  $Z = 8$ , and study of the drip-lines presently an active field of research [1]. The drip-lines are often defined with respect to neutron and proton separation energies, denoted  $S_n$  and  $S_p$ , which denote the amount of energy required to remove respectively one neutron or one proton from a nucleus.

## 1.2 Magic Numbers and Shell Structure

Certain combinations of proton and neutron numbers have been found to have enhanced stability relative to surrounding nuclei. This effect was first observed in nuclear mass data. A plot of proton (neutron) separations energies against proton (neutron) numbers for nuclei of fixed proton-neutron asymmetry reveal dramatic discontinuities at  $N=2, 8, 20, 28, 50, 82$ , and  $126$  and  $Z=2, 8, 20, 28, 50$ , and  $82$  – known as magic numbers [2]. Nuclei in which both  $Z$  and  $N$  are magic are called doubly-magic systems, while those in which only one of the two is magic are referred to as semi-magic. The observed discontinuities are analogous to those observed in the ionization energy of atoms upon filling of each major electronic shell and represent the first evidence of shell structure in nuclei. As instrumentation technology advanced, magic nuclei were found to also be characterized by enhanced excitation energy for the first excited state ( $E(2^+)$ ) when compared to neighboring even-even nuclei and reduced transition probability ( $B(E2; 2_1^+ \rightarrow 0_1^+)$ ) between the first excited state and the ground state [3].

More recent measurements employing radioactive ion beam reveal a transient na-

ture in magic numbers [4]. Systematic studies of mass data as well as excitation spectra and strength (when available) clearly indicate the weakening of magic numbers well-established for stable nuclei and the emergence of new magic or semi-magic systems [5,6]. The structure of the more loosely bound exotic or unstable nuclei may differ dramatically from stable nuclei, possibly in the form of halo states or proton/neutron skins. As interactions within the nuclear medium are closely linked to the matter distribution due to the short range of the strong force, one may expect that the changing structure will culminate in a modification of the nuclear potential and consequently of the magic numbers, which are a fingerprint of that potential.

### 1.3 The Nuclear Shell Model

Given that the nucleus is comprised of strongly interacting particles, one may assume that the single-particle structure would be highly chaotic. While this may be the case for highly excited nuclear systems, single-particle excitations clearly play an important role at in the low-lying excitation spectrum. At low excitation energies, the nucleus may be viewed as a Fermi liquid in which nucleon-nucleon interactions are hindered by Pauli blocking, and stable single-particle orbits arise. Given the strong interaction of nucleons with the nuclear medium, the single-particle states are associated with quasi-particles and quasi-holes with physical characteristics that differ from free-nucleons. The nucleus is characterized by a Fermi energy. Low-lying excitations are of the form of either a single-particle excitation or a collective excitation involving many correlated single-particle excitations.

To approximate the true nuclear potential, which consists of  $A(A - 1)$  nucleon-nucleon interactions, a mean potential is subtracted from the two-body interaction. The mean potential is chosen to minimize the off-diagonal matrix elements of the Hamiltonian. The Hamiltonian then consists of a mean potential, from which single-particle orbits are derived, and a residual two-body interaction between these states.

Solutions for the nuclear wavefunction are found by diagonalizing the Hamiltonian matrix, and the off-diagonal terms in the pure single-particle basis lead to nuclear wavefunctions consisting of multiple single-particle configurations. This phenomenon is referred to as configuration mixing.

The dimension of the Hamiltonian is given by the number of single-particle states. As numerical matrix computations are only tractable for finite sized matrices, approximation is required to carry out shell model calculations. An approximation commonly used is the assumption of an inert core. States of some minimum energy below the Fermi energy are assumed to be fully occupied and non-interacting, and the core serves as an effective vacuum in which particle and holes can be added. The core is usually taken as the closest doubly-magic system to the nucleus of interest. While no-core shell model calculations exist [7], a second approximation, truncation, is generally unavoidable. Calculations must be restricted to a subset of the possible single-particle states, referred to as the model or valence space. With an assumed core and truncated model space, phenomenological effective interactions are derived based on fits to deduced nuclear properties. These effective interactions apply to the quasi-particle states within the nucleus and compensate for the assumed core and truncated model space.

Given that the strong force has a very short range, the mean potential closely mimics the nuclear matter distribution and can be approximated by a Wood-Saxon function:  $f_{WS}(x) = V_0 / (1 + \exp((r - r_0)/a))$  where  $V_0$  is the depth,  $r_0$  is the radius parameter, and  $a$  is the diffuseness. However, such a potential fails to reproduce the observed magic numbers. The magic numbers are recovered when a large spin-orbit term is added to the potential which breaks the degeneracy of  $\ell$ -states.

The mean potential is adjusted to reproduce observed single-particles where available [4]. When not available, single-particle energies are taken from Hartree-Fock calculations. The proton and neutron single-particle energy spectra for  $^{34}\text{Si}$  are shown in figure 1.2. The spectra are obtained in a Hartree-Fock calculation using the SkX

Skyrme interaction [8]. The larger 5-10 MeV gaps between the single-particle orbits show the separation between major shells while the subshells are separated by smaller 2-5 MeV gaps. Each shell gap is indicated by the magic number of cumulative nucleons which fill the shells below.

The single-particle states are labeled  $\tau n \ell j$  where  $\tau$  is  $\nu$  for neutron states and  $\pi$  for protons states,  $n$  is the principle quantum number,  $\ell$  is the angular momentum quantum number denoted  $s, p, d, f, g, h \dots$  for  $\ell = 0, 1, 2, 3, 4, 5 \dots$ , and  $j$  is the total angular momentum quantum number of the single particle state. The principle quantum number  $n$  is equivalent to that of the harmonic oscillator potential which is given as  $n = 2n_r + \ell$  where  $n_r$  is the radial quantum number. Each major shell may be labeled by the  $\ell$ -values of the constituent single-particle states such that the first shell is the  $s$  shell, the second is the  $p$  shell, the third is the  $sd$  shell, and so on. Single-particle configurations are often expressed in an exponential form. For example, the lowest-lying normal-filling configuration in  ${}^5\text{He}$  may be written  $(\pi 1s_{1/2})^2(\nu 1s_{1/2})^2(\nu 1p_{3/2})^1$  where the parentheses indicate single-particle states with occupancies given in the exponent. This configuration may also be expressed relative to the closed  $s$ -shell or doubly-magic  ${}^4\text{He}$  system as  $(s)^4(\nu 1p_{3/2})^1$  or  ${}^4\text{He}(\nu 1p_{3/2})^1$ .

Effective interactions are derived with respect to an assumed inert core and model space and consequently are only valid in particular regions of the nuclear chart. For a review of effective interactions for the low to medium mass region of the nuclear chart, see reference [4]. In the present work, the neutron-rich region between  $N = 16$  and  $N = 20$  and with  $Z = 10, 12$  is considered. With respect to normal single-particle ordering, both protons and neutrons fill the  $sd$  shell in this region. Therefore, the Universal SD (USD) interaction [9] is employed to interpret results. The USD interaction assumes inert  ${}^{16}\text{O}$  and  ${}^{40}\text{Ca}$  cores and includes the  $1d_{5/2}$ ,  $2s_{1/2}$ , and  $1d_{3/2}$  orbitals in its model space.

Often for a given nucleus, states are observed at relatively low energy in the excitation spectrum that do not correspond to states predicted from a relevant effective

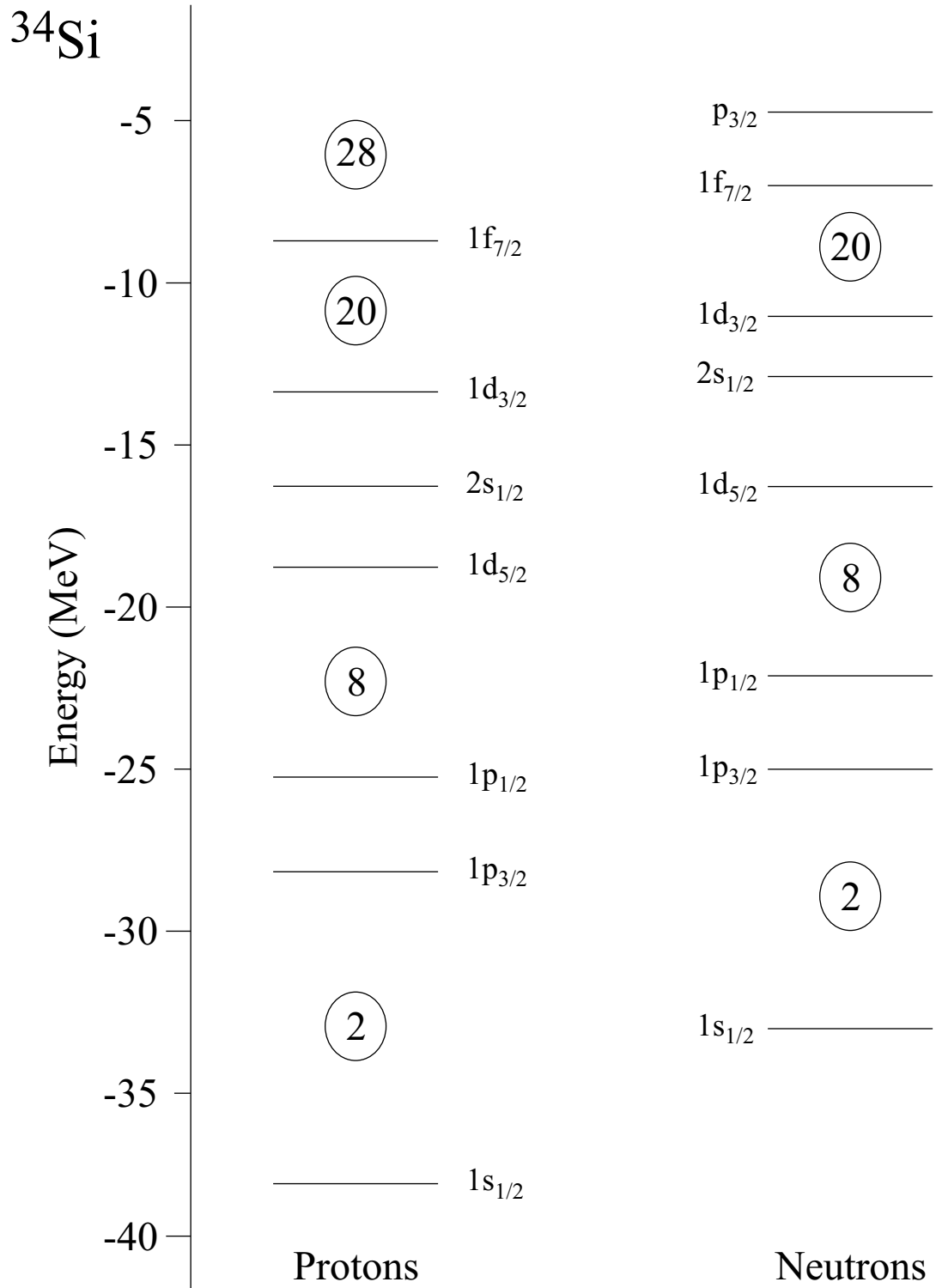


Figure 1.2: Single-particle energies for  $^{34}\text{Si}$ . The single-particle energies are determined in a Hartree-Fock calculations using the SkX Skyrme interaction [8].

interaction. These states are called intruder states and are a result of contributions from beyond the assumed model space. They are often dominated by particle-hole configurations across the next major shell gap or, in other words, configurations in which one or more nucleons are promoted across the shell gap. These configurations are sometimes abbreviated as  $np-nh$  or  $N\hbar\omega$  configurations where  $n$  and  $N$  represent the number of particle promoted to the next shell.

In the present work, intruder states are of central importance, and an effective interactions that goes beyond the  $sd$  model space is required. The recently developed SDPF-M interaction [10] includes the three  $sd$  orbitals as well as the  $1f_{7/2}$  and  $2p_{3/2}$  orbitals from the  $fp$  shell. Development of this interaction, with a much larger model space, is facilitated by the use of a Monte Carlo technique for matrix diagonalization [11] in a class of calculations referred to as Monte Carlo Shell Model (MCSM) calculations [12].

## 1.4 Nuclear Structure of Neutron-Rich Nuclei Between $N=16$ and $N=20$

Neutron-rich nuclei with atomic numbers between  $Z \approx 8$  and  $Z \approx 12$  exhibit dramatic differences in their structure compared to stable isotopes, even at the level of shell closures [13]. While  $^{16}\text{O}$  is a prototypical doubly-magic nucleus with a shell gap of 10 MeV [14], the ground state of  $^{28}\text{O}$ , with canonical magic numbers  $Z = 8$  and  $N = 20$ , is not particle-bound: The  $N = 20$  shell closure is not strong enough to bind  $^{28}\text{O}$ . Contrary to expectations, recent experiments have indicated a pronounced  $N = 16$  subshell closure [5, 15, 16] culminating in the identification of  $^{24}\text{O}$  as a doubly magic nucleus [15] and leading to the revision of the effective interaction for the  $sd$ -shell [10, 13]. Adding one proton to the heaviest particle-bound oxygen isotope ( $^{24}\text{O}$ ) dramatically shifts the neutron drip-line at  $Z = 9$  and allows for the binding of at least six additional neutrons [17]. The  $N = 20$  major shell closure also breaks down for  $^{31}\text{Na}$

and  $^{32}\text{Mg}$  as indicated by an excess of binding energy [18, 19] and by measurements sensitive to collectivity [20–22]. Both observations, supported by theory, indicate a region of  $N \geq 20$  and  $Z \leq 12$ , referred to as the “island of inversion” [23], in which the ground-state wave function is dominated by intruder configurations characterized by particle-hole excitations across the  $N = 20$  shell gap.

These observations have posed a formidable challenge to nuclear structure models. Much effort has been focused on the island of inversion around  $^{31}\text{Na}$ . The onset of deformation along the supposed magic neutron-rich  $N = 20$  isotones was reproduced in a deformed Hartree-Fock calculation in which cross shell excitation to the  $1f_{7/2}$  orbital is allowed [24]. This result was further confirmed by shell-model calculations with an  $(1d_{5/2})^6(2s_{1/2})^2(1d_{3/2})^n + (1d_{5/2})^6(2s_{1/2})^2(1d_{3/2})^n - 2(1f_{7/2})^2$  neutron configuration space [25]. A more complete calculation including both the  $1f_{7/2}$  and  $2p_{3/2}$  single-particle states was later carried out with a  $(sd)^n + (1d_{5/2})^6(2s_{1/2})^2(1d_{3/2})^n - 10(1f_{7/2}, 2p_{3/2})^2$  neutron configuration space [26]. For this calculation, the energy of the  $2\hbar\omega$  configuration is determined to be  $\approx 3$  MeV higher than that of the  $0\hbar\omega$  configuration. However, for the  $2\hbar\omega$  configuration, the energy gained in residual particle-hole and pairing interactions, referred to as correlation energy, is greater than the  $2\hbar\omega - 0\hbar\omega$  splitting for  $^{30}\text{Ne}$ ,  $^{31}\text{Na}$ , and  $^{32}\text{Mg}$ . This result clearly demonstrates that effects such as correlation energy are just as important as the spacing of single-particle states in explaining the breakdown of shell gaps.

Proposed boundaries of  $10 \leq Z \leq 12$  and  $20 \leq N \leq 22$  are established for the island of inversion by means of shell-model calculations incorporating the entire  $fp$ -shell into the model space [23]. The effective interaction used by Warburton *et al.* is constructed to match measured properties of a wide range of nuclei within the model space and, therefore, allows for a systematic study of the transition into the island of inversion. With this interaction, the existence of the island of inversion around  $^{31}\text{Na}$  is explained in terms of not only a reduced  $N = 20$  shell gap but also in terms of increased pairing and proton-neutron interaction energies.

One difficulty in calculations discussed so far, pointed out by Warburton *et al.* [23], is the “ $n\hbar\omega$  truncation catastrophe” in which free mixing within a truncated model space consisting of say  $0\hbar\omega + 2\hbar\omega$  configurations leads to inaccuracies in binding energies. This obstacle is overcome in the more recent Monte Carlo shell model (MCSM) scheme [12]. MCSM calculations using the SDPF-M interaction employ a numerical scheme which renders large-dimension shell-model calculations tractable and thereby allows for unrestricted mixing of  $n\hbar\omega$  configurations within the  $(sd)(1f_{7/2})(2p_{3/2})$  configuration space. As with the calculations of Warburton *et al.* the SDPF-M interaction is formulated to reproduce observed properties over a broad range of nuclei.

Results of SDPF-M calculations are applicable both within the island of inversion and in the surrounding transitional regions and are compared to the several structural phenomena observed in the neutron-rich  $N = 16-20$  region. The SDPF-M interaction is very similar to the USD interaction over a broad range of  $sd$  nuclei since the SDPF-M interaction employs the USD interaction to handle the  $sd-sd$  configuration mixing. Both SDPF-M and USD predict an enhanced  $N = 16$  subshell gap culminating in a doubly-magic  $^{24}\text{O}$  [27]. For  $^{29}\text{F}$ , SDPF-M results include a considerable 4p-4h component in the ground state in addition to enhanced pairing which leads to a bound ground state, explaining the puzzling extension of the drip-line at  $Z = 9$  [28].

SDPF-M calculations have also proven accurate in reproducing the observed weakening of  $N = 20$  magic number. The calculated two-neutron separation energies,  $E(2_1^+)$ , and  $B(E2; 2_1^+ \rightarrow 0_1^+)$  for a number of nuclei in this region, including  $^{32}\text{Mg}$ , are found to be in agreement with deduced values [10]. Of equal importance, it is noted that SDPF-M results suggests a less definite boundary to the island of inversion around  $^{31}\text{Na}$ , suggesting a possible transitional region [10]. For  $N > 17$ , transitions from normal- to intruder-dominance have been observed for magnesium and sodium isotopes. While  $^{30}\text{Mg}$  ( $N = 18$ ) is well-described without considering cross-shell configurations [29, 30], at  $N = 19$  the low-energy level structure [31, 32] and the recently measured magnetic moment of its ground state [33] indicate a strong admixture of

intruder configurations in  $^{31}\text{Mg}$ . Therefore, for  $Z = 12$  isotopes there appears to be a sharp transition at  $N = 19$  into the island of inversion. For sodium with just one proton less, recent systematic calculations [34] which agree with measured observables for this isotopic chain suggest a broader transitional region. The  $N = 19$  nuclide  $^{30}\text{Na}$  is concluded to lie within the island of inversion while measurements for  $^{29}\text{Na}$ , predicted to be outside of the island, indicate a significant intruder admixture. Sufficient data does not exist to systematically track the transition in the neon isotopic chain. However, already at  $N = 18$ ,  $^{28}\text{Ne}$  shows characteristics indicating that it is on the boundary of the island of inversion [29, 35].

In the present work, the single-particle structure of the ground state of the neutron-rich  $^{26,28}\text{Ne}$  and  $^{30,32}\text{Mg}$  is probed by single-neutron knockout from intermediate energy ion beams. SDPF-M shell model calculations predict varying admixtures of  $N = 20$  cross-shell intruder configurations in the ground state of these nuclei [10], and the goal of this study is to directly observe and quantify those admixtures for comparison with shell model predictions.

## 1.5 Shell Model Predictions for $^{26,28}\text{Ne}$ and $^{30,32}\text{Mg}$

In discussing shell model results in the region near the  $^{31}\text{Na}$  island of inversion, both the USD and SDPF-M effective interactions are employed. Since the USD model space does not include  $fp$  orbitals, shell-breaking effects are not included in calculations using this interaction. Differences between USD and SDPF-M predictions near the island of inversion highlight the influence of cross shell intruder effects.

The USD and SDPF-M calculations for the excitation spectrum of  $^{25}\text{Ne}$  are shown in figure 1.3 while the predicted neutron single-particle occupancies are shown in table 1.1. Both interactions predict an enhanced  $N = 16$  subshell gap at  $^{26}\text{Ne}$ . In the context of the present measurement, this enhancement leads to a small occupancy in the  $1d_{3/2}$  single-particle state and small cross sections to  $3/2^+$  states in direct

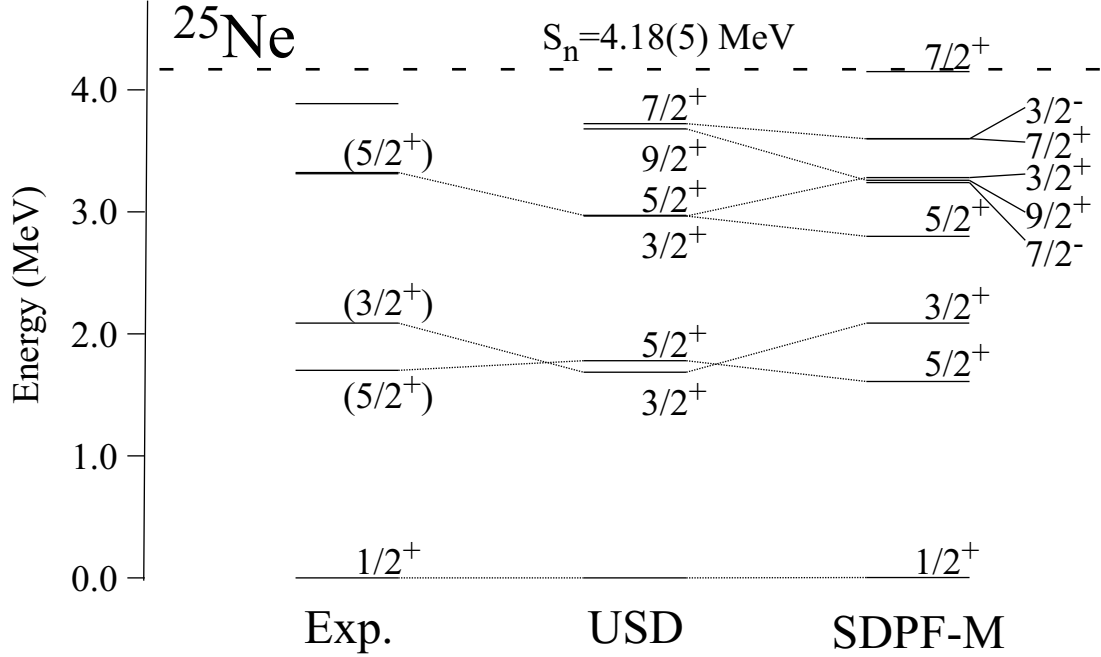


Figure 1.3: Observed and calculated level scheme of  $^{25}\text{Ne}$ . Calculated level schemes using the USD and SDPF-M interaction are compared to the observed level structure. Spin and parity assignments are taken from refs. [36, 37]

$nlj$	USD	SDPF-M
$1d_{5/2}$	5.67	5.68
$2s_{1/2}$	1.61	1.74
$1d_{3/2}$	0.72	0.48
$1f_{7/2}$	—	0.08
$2p_{3/2}$	—	0.02

Table 1.1: Neutron single-particle occupancies for  $^{26}\text{Ne}$ . Occupancies are calculated using the USD and SDPF-M interactions. USD calculations do not include  $fp$  single-particle states and, therefore, give no prediction for their occupancy.

neutron stripping reactions. More importantly, the SDPF-M calculation suggests a very small occupancy in  $fp$  shell single particle states for the  $^{26}\text{Ne}$  ground state. The aim of the present work is to probe this state to quantitatively assess the extent of intruder content.

Similar calculations for the  $^{27,28}\text{Ne}$  nuclei are presented in figure 1.4 and table 1.2. Figure 1.4 clearly shows differing results from the USD and SDPF-M calculations. While USD predictions suggest only two bound states, SDPF-M predictions indicate

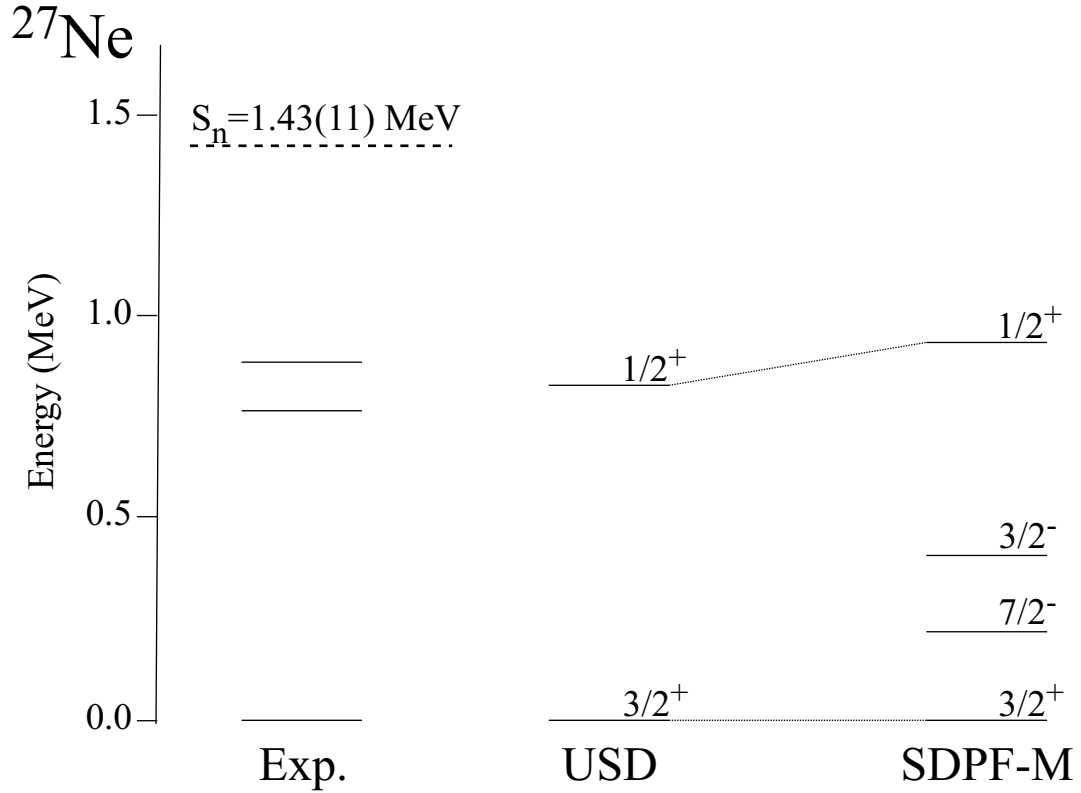


Figure 1.4: Observed and calculated level scheme of  $^{27}\text{Ne}$ . Calculated level schemes using the USD and SDPF-M interactions are compared to the observed level structure. The observed level scheme is taken from the present work.

four. The SDPF-M ground state and 0.9 MeV state are in agreement in spin, parity, and energy with the USD-predicted  $3/2^+$  ground state and  $1/2^+$  excited state. In fact, the summed occupancy in  $fp$  shell single particle orbitals is rather small, indicating the dominance of  $sd$  shell configurations for these states. However, SDPF-M also predicts two negative parity bound states which are clearly intruders. Already at  $N = 17$ , SDPF-M calculations predict degenerate  $0\hbar\omega$  and  $n\hbar\omega$  states. The  $fp$  occupancy in the  $^{28}\text{Ne}$  ground states is substantial. Both USD and SDPF-M predictions are shown in table 1.2. While the  $1d_{5/2}$  and  $2s_{1/2}$  occupancies are very similar, SDPF-M results suggest that approximately half of the remaining neutrons occupy states in the  $fp$  shell where USD calculations must place these in the  $1d_{3/2}$  orbit.

Results of the SDPF-M calculations for level schemes of  $^{29,31}\text{Mg}$  are shown in figure 1.5 while results for the neutron single-particle occupancies in the ground states

State	USD	SDPF-M
$1d_{5/2}$	5.88	5.83
$2s_{1/2}$	1.93	1.87
$1d_{3/2}$	2.18	1.18
$1f_{7/2}$	—	0.89
$2p_{3/2}$	—	0.24

Table 1.2: Neutron single-particle occupancies for  $^{28}\text{Ne}$ . Occupancies are calculated using the USD and SDPF-M interactions. USD calculations do not include  $fp$  single-particle states and, therefore, give no prediction for their occupancy.

State	$^{30}\text{Mg}$	$^{32}\text{Mg}$
$1d_{5/2}$	5.77	5.83
$2s_{1/2}$	1.81	1.90
$1d_{3/2}$	1.82	2.12
$1f_{7/2}$	0.52	1.83
$2p_{3/2}$	0.08	0.32

Table 1.3: Neutron single-particle occupancies for  $^{30,32}\text{Mg}$ . Occupancies are calculated using the SDPF-M interaction.

of  $^{30,32}\text{Mg}$  are given in table 1.3. The calculated separation between the normal and intruder states is approximately 0.5 MeV for  $^{29}\text{Mg}$  while for  $^{31}\text{Mg}$  the intruder and normal states are degenerate. Results of  $\beta$ -decay and  $\beta$ -delayed neutron measurements indicate that for both nuclei the first two excited states above the low-lying doublet have negative parity, in agreement with SDPF-M predictions. These previous measurements are consistent with a considerable influence of intruder states at low-excitations in  $^{29,31}\text{Mg}$ . The calculated single-particle occupancies reflect the dramatic change in structure occurring between  $^{30}\text{Mg}$  and  $^{32}\text{Mg}$  where the latter lies within the island of inversion and the former does not. For  $^{30}\text{Mg}$  the  $fp$  shell occupancy of 0.6 neutrons is modest but not negligible. However, adding two neutrons to the system which by normal filling would occupy states in the  $sd$  shell, the  $sd$  occupancy remains virtually unchanged as the additional neutrons occupy  $fp$  states.

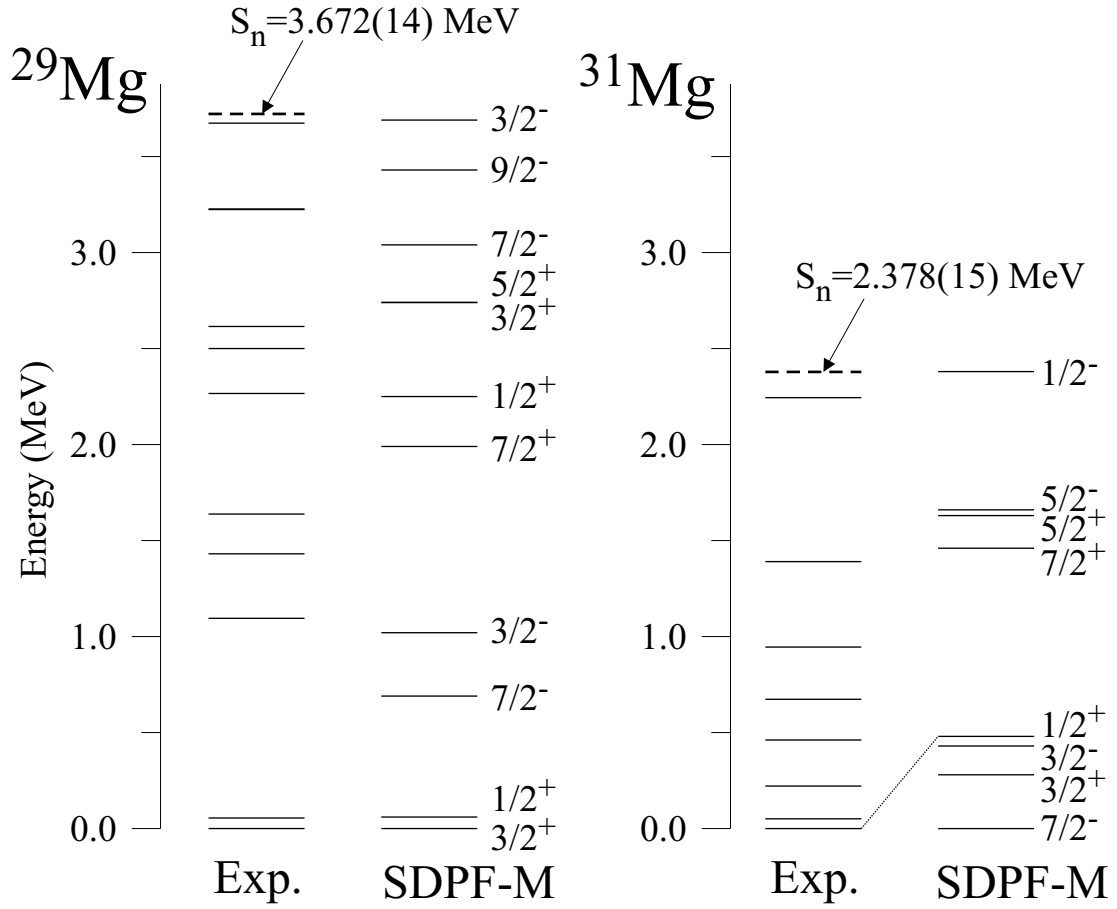


Figure 1.5: Observed and calculated level scheme of  $^{29,31}\text{Mg}$ . Calculated level schemes using the SDPF-M interaction are compared to the observed level structure. The observed level scheme is taken the Evaluated Nuclear Structure Data File (ENSDF) [38].

## 1.6 Nucleon Knockout Reactions

Nucleon knockout experiments in inverse kinematics are sensitive to the occupation number of single-particle orbitals [39, 40], and represent a selective spectroscopic tool to investigate the evolution of shell closures in rare isotopes. This method allows for detailed spectroscopy of the ground state wavefunction and provides a quantitative measure of intruder content. Intruder configurations are observed in this direct reaction through the measurement of significant spectroscopic strength to states in the reaction product with the same parity as the intruding shell. Further, the strength of the feeding quantifies the extent of the admixture of intruder configurations.

A schematic illustration of a typical knockout reaction is shown in figure 1.6. This reaction is defined as an event in which a mass  $A$  nucleus impinges on a light nuclear target, and a mass  $A-1$  reaction residue, often in an excited state, is observed moving at approximately projectile velocity in the exit channel. Detection of  $\gamma$ -rays coincident with knockout events allow tagging of individual final states populated in the reaction. To simplify the mechanics of the reaction, the incident nucleus typically has kinetic energy greater than approximately 50 MeV/nucleon.

Since the removed nucleon is typically not observed, this reaction is a highly inclusive process, encompassing a number of breakup channels. The two dominant channels, stripping and diffractive breakup, are illustrated in figure 1.6. In the stripping reaction, the removed nucleon is absorbed by the target while, in diffractive breakup, both the nucleon and residual core interact elastically with the target leaving the core-nucleon system in an unbound state.

Knockout reactions are peripheral reactions in which the nuclear wavefunction is probed at the surface of the nucleus. This is guaranteed by the criteria that the  $A-1$  residual core must survive and move forward with approximately the same velocity as the incident nucleus. Using the phenomenological formula for the mean nuclear radius  $r(A) = c A^{1/3}$  fm and a black-disk, or touching-spheres, approximation for the

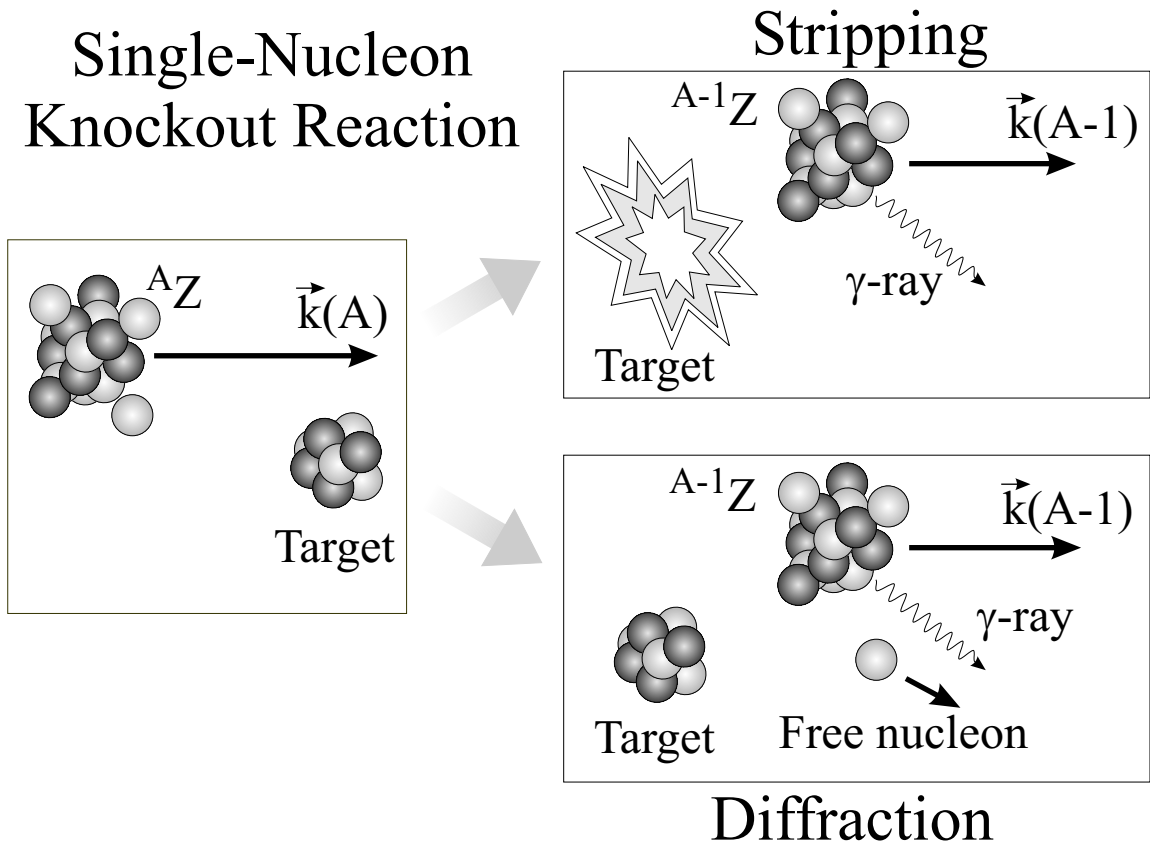


Figure 1.6: Schematic of typical knockout reaction. Initially, the projectile and target approach at a high relative velocity. In the final state, one or few nucleons have been removed from the projectile, and the resulting reaction fragment moves forward at approximately the initial projectile velocity. The fragment may be in an excited state and would decay by particle or photon emission.

core-target and nucleon-target interaction, only  $33/A$  % of the radius within the nuclear interior is probed. This is only about 1% for the  $A=30$  mass region. This peripheral condition assures that the majority of the inclusive knockout cross section results from the removal of valence nucleons leading to the population of relatively low-energy single-particle states in the residue.

There are two basic observables in a knockout measurement: partial cross sections to individual states of the residue and longitudinal momentum distributions of the residue. Given the direct nature of this reaction, the partial cross sections carry spectroscopic information about the wavefunction of the projectile. The high-energy at which the incident projectile interacts with the target leads to a short interaction time between the residual core and the target. Therefore, the momentum distributions of the residue is closely linked to that of the removed nucleon. The width of this distribution is sensitive to the spatial extent of the removed nucleon and therefore its angular momentum quantum number. For an overview of knockout reactions, including details of the reaction model, applications to the study of nuclear structure, and recent results, see Ref. [39].

### 1.6.1 Eikonal Reaction Model for Knockout

The knockout reaction is treated in a three-body model comprised of a target, nucleon, and core. Applicability of this model therefore requires the validity of a pre-formation assumption of the core-nucleon system in the projectile. Cross sections calculated in this model are referred to as single-particle or unit cross sections as the core-nucleon wavefunction is normalized to unity indicating that exactly one nucleon occupies the single-particle state. In reality, the normalization of the wavefunction ranges anywhere from zero for an unoccupied state to  $2J + 1$  for a fully occupied state, and this normalization represents a sensitivity to the single-particle structure within the knockout cross section.

The structure sensitivity is illustrated in equation 1.1 where the left side represents

the knockout cross section for populating the  $i^{th}$  core state. The reaction mechanism enters the equation in the form of a single-particle cross section while the structure contribution takes the form of a spectroscopic factor that, from a many-body perspective, represents the overlap between the initial state in the projectile and the  $k = (nlj)$  single-particle state coupled to the  $i^{th}$  core state. For spin and parities  $0^+$  and  $J^\pi$  for the initial and core states, the summation reduces to terms which include only single particle states with  $J^\pi$  spin and parity. Spectroscopic factors are deduced from the present measurements assuming an active valence space which includes the  $1d_{5/2}$ ,  $2s_{1/2}$ ,  $1d_{3/2}$ ,  $1f_{7/2}$ , and  $2p_{3/2}$  single-particle states. Spectroscopic factors to other single-particle states are assumed to be negligible. Therefore, the summation in equation 1.1 reduces to a single term.

$$\sigma_i = \sum_k C^2 S_i(k) \sigma_{sp}(S_n, k) \quad (1.1)$$

For nucleon knockout in inverse kinematics from high-energy projectiles, the reaction process is modeled subject to the sudden and Eikonal approximations. In applying the sudden approximation the interaction time between the projectile and the target is assumed to be short such that the probability of multi-step processes occurring is negligibly small. These multi-step processes include dynamical excitation of intrinsic core and nucleon degrees of freedom in addition to those of the core-nucleon system. In applying the Eikonal approximation the deflection of the projectile trajectory due to interaction with the target is assumed to be negligible.

The initial state of the system in the center of mass frame given by  $\phi_o(\vec{r})$  where  $\vec{r}$  is the relative coordinate between the core and nucleon. After interaction with the target, applying the Eikonal and sudden approximations, the initial state is modified by Eikonal phases for the core and the nucleon,  $S_c$  and  $S_n$ , with no explicit modification of the relative wavefunction. Calculation of the knockout cross section and longitudinal momentum distributions are performed according to equations 9-10

(diffractive breakup) and 11-12 (stripping) of reference [41].

The core-target and nucleon-target interactions, treated using semi-classical Eikonal or Glauber theory, enter in the form of phase shifts calculated assuming a linear trajectory as shown in equation 1.2.

$$S_i(\vec{b}) = \exp\left(\frac{-i}{\hbar v} \int_{-\infty}^{\infty} V_{i,t}(\vec{b}, z) dz\right) \quad (1.2)$$

The eikonal phase shift is dependent on the two-dimensional impact parameter  $\vec{b}$  of the  $i^{th}$  body, either the core or the nucleon, and the interaction potential between the target and the  $i^{th}$  body. The interaction potential is derived from the density-folded nucleon-nucleon interaction cross section according to equation 1.3.

$$V(\vec{b}, z) = -\frac{\hbar v}{2} \int \sigma_{NN}(\alpha_{NN} + i) \rho_i(\vec{r} - (\vec{b}, z)) \rho_t(\vec{r} - (\vec{b}, z)) d^3\vec{r} \quad (1.3)$$

In equation 1.3,  $\rho_i$  and  $\rho_t$  represent the nucleon number density distribution for the  $i^{th}$  body and the target, respectively, while  $\sigma_{NN}$  and  $\alpha_{NN}$  are the free nucleon-nucleon interaction cross section and the ratio of the imaginary to real part of the nucleon-nucleon scattering amplitude. The nuclear density can be modelled as a Gaussian distribution for low-mass nuclei with an rms radius inferred from total reaction cross sections. However, uncertainty in or lack of data for the rms radii of more exotic nuclei has led to the use of values taken from Hartree-Fock calculations, known to reproduce a number of observables in the mass regions of interest.

The core-nucleon interaction is derived from a two-body Wood-Saxon potential. The potential, given in equation 1.4, has three parameters: the well depth  $V_0$ , the radius coefficient  $R_0$ , and the diffuseness  $a$ . (The  $A$  parameter in equation 1.4 represents the mass number of the core.) Given parameters  $a$  and  $R_0$ , the well depth  $V_0$  is chosen to reproduce the known binding energy of the system, which is calculated as the sum of the nucleon separation energy of the mass  $A$  system and the excitation energy of the mass  $A-1$  system.

$$V(r) = -V_0 \left( 1 + \exp \left( \frac{r - R_0 A^{1/3}}{a} \right) \right)^{-1} \quad (1.4)$$

In early work employing knockout reactions, the  $a$  and  $R_0$  shape parameters of the Wood-Saxon potential were fixed so as not to introduce artificial trends in systematics from these measurements. More recently,  $R_0$  has been adjusted to match rms radii for single-particle states obtained in a Hartree-Fock calculation using the Skyrme interaction SKX [8]. For these calculations the core density is also taken from the Hartree-Fock calculation as opposed to the assumed Gaussian distribution discussed above. A reasonable value between 0.5 and 0.7 is chosen for the diffuseness. However, the diffuseness has been shown to have little impact on the results of the calculation when the rms radius is fixed [37].

### 1.6.2 Calculated Unit Cross Sections and Momentum Distributions

Unit cross sections and momentum distributions are calculated within the Eikonal reaction theory discussed in section 1.6.1. Eikonal phases  $S_n$  and  $S_c$  are calculated with the incident energy and the core and target densities as input. The reaction target used for all four measurements is a 376 mg/cm<sup>2</sup> beryllium plate. The density distribution of the low-mass <sup>9</sup>Be is assumed to be Gaussian with an rms radius of 2.36 fm [42, 43]. The core density distributions are taken from Hartree-Fock calculations using the SKX Skyrme interaction [8]. The Hartree-Fock rms radius of each knockout residue, denoted  $R_{rms}^{\rho, (H - F)}$ , is given in the respective reaction header in tables 1.4 and 1.5.

For each neutron-removal reaction studied, the incident energy is calculated from the beam momentum measured in the dipole just before the reaction target. Energy loss is calculated through half of the reaction target using ATIMA code [44]. Uncertainty in this parameter is dominated by the 1% uncertainty in the absolute magnetic

rigidity  $B\rho$  in the dipole due to uncertainty in the bending radius  $\rho$ . Although the reaction occurs at a range of energies, the mid-target energy is used since the cross section is approximately linear over the energy-loss ranges. The mid-target beam energies and calculated energy losses in the 2 mm thick beryllium target are given in the reaction header for each measured reaction in tables 1.4 and 1.5. The first two columns give the energy of the core state and the binding energy of the neutron that is removed to populate this state. The third column gives the assumed quantum state of the removed neutron. The  $n$  and  $\ell$  are important for calculating both the Hartree-Fock rms radius and the core-nucleon wavefunction, while the  $j$  quantum number plays a smaller role in determining the Hartree-Fock radius and has no direct effect on the shape of the core-nucleon wavefunction. The calculated Hartree-Fock radii along with the resulting Wood-Saxon parameters and the rms radius of the core-nucleon wavefunction are given in the center columns of tables 1.4 and 1.5.

The core-nucleon interaction is modeled with a two-body Wood-Saxon potential as discussed in section 1.6.1. The rms radius of each single-particle state is taken from a Hartree-Fock calculation using the SKX Skyrme interaction [8]. The neutron binding energy for each populated core state is taken as the sum of the neutron separation energy of the initial mass- $A$  ground state and the excitation energy of the final state in the mass- $(A-1)$  knockout residue. When determining the Hartree-Fock rms radius, the binding energy of the single-particle state of interest is fixed to the known neutron binding energy. Further, the depth of the Wood-Saxon potential is chosen to give the corrected binding energy. A summary of the core-nucleon interaction calculation is given in tables 1.4 and 1.5 for each of the neutron knockout reactions studied.

With the Eikonal phases and core-nucleon wavefunction, the unit neutron knockout cross sections are calculated for each final core state. Results of this calculation are given in columns 8-10 of tables 1.4 and 1.5. The contributions from the stripping (str) and diffractive breakup (dif) are given separately, and the sum of these two gives the total calculated single-particle cross section  $\sigma_{sp}$ . The differential cross

$E_{level}^{(core)}$ (MeV)	BE (MeV)	$n\ell_j$	$R_{rms}^{(HF)}$ (fm)	$R_0$ (fm)	$a$ (fm)	$R_{rms}$ (fm)	$\sigma_{sp}^{(str)}$ (mb)	$\sigma_{sp}^{(dif)}$ (mb)	$\sigma_{sp}$ (mb)	$P_{//,rms}^{(lab)}$ (MeV/c)
<b><math>{}^9\text{Be}({}^{26}\text{Ne}, {}^{25}\text{Ne})\text{X}</math></b>										
$E_{mid}=82.6(17)$ MeV/u		$\Delta E=258$ MeV			$R_{rms}^{\rho,(H-F)}=2.94$ fm					
0.000	5.530	$2s_{1/2}$	3.806	1.074	0.7	3.881	22.2	8.6	30.8	44.1
1.703	7.232	$1d_{5/2}$	3.461	1.222	0.7	3.530	14.9	4.4	19.3	92.6
2.090	7.620	$1d_{3/2}$	3.431	1.218	0.7	3.499	14.5	4.2	18.7	93.9
3.316	8.845	$1d_{5/2}$	3.387	1.231	0.7	3.454	13.8	3.9	17.7	95.7
<b><math>{}^9\text{Be}({}^{28}\text{Ne}, {}^{27}\text{Ne})\text{X}</math></b>										
$E_{mid}=82.3(16)$ MeV/u		$\Delta E=258$ MeV			$R_{rms}^{\rho,(H-F)}=3.06$ fm					
0.000	3.900	$2s_{1/2}$	4.140	1.067	0.7	4.216	25.1	10.8	36.0	49.2
0.000	3.900	$2p_{3/2}$	4.172	1.034	0.7	4.249	25.3	10.5	35.8	64.0
0.000	3.900	$1d_{3/2}$	3.729	1.304	0.7	3.797	16.3	5.3	21.7	97.6
0.000	3.900	$1f_{7/2}$	3.667	1.188	0.7	3.734	15.1	4.7	19.8	129.3
0.900	4.800	$2s_{1/2}$	3.974	1.087	0.7	4.047	22.3	9.1	31.4	51.7
0.900	4.800	$2p_{3/2}$	4.031	1.045	0.7	4.105	22.8	9.0	31.8	66.6
0.900	4.800	$1d_{3/2}$	3.648	1.195	0.7	3.715	15.3	5.1	20.4	98.0
0.900	4.800	$1f_{7/2}$	3.622	1.193	0.7	3.688	14.4	4.3	18.7	131.4

Table 1.4: Summary of calculated single-particle cross sections for neutron knockout from  ${}^{26,28}\text{Ne}$ . The left-most two columns give the excitation energy of the final state and the binding energy of the removed nucleon. The next five columns list the assumed single-particle state from which the neutron is removed along with the rms radius determined in a SkX Hartree-Fock calculation [8]. This group of five columns also includes Wood-Saxon parameters that match the Hartree-Fock radius and the resulting rms radius of the Wood-Saxon wavefunction. The calculated single particle cross sections for the stripping, diffractive, and total knockout cross section are listed in the next three columns. The last column gives the width (FWHM) of the longitudinal momentum distribution.

section with respect to the longitudinal component of the core momentum is also calculated as described in section 1.6.1. The rms width of each distribution is given in the last column of tables 1.4 and 1.5.

To check the sensitivity of the calculated single-particle cross sections to input parameters, each parameter is varied in the  ${}^{28}\text{Ne}$  ground state calculation for each  $\ell$ -value from zero to three. In separate calculations, the diffuseness was adjusted from 0.7 to 0.6; the core-nucleon rms radius was scaled down by 5%; and the incident energy was increased by 3%. Also in a separate calculation, the core density profile

$E_{level}^{(core)}$ (MeV)	BE (MeV)	$n\ell_j$	$R_{rms}^{(HF)}$ (fm)	$R_0$ (fm)	$a$ (fm)	$R_{rms}$ (fm)	$\sigma_{sp}^{(str)}$ (mb)	$\sigma_{sp}^{(dif)}$ (mb)	$\sigma_{sp}$ (mb)	$P_{//,rms}^{(lab)}$ (MeV/c)
<b><math>{}^9\text{Be}({}^{30}\text{Mg}, {}^{29}\text{Mg})\text{X}</math></b>										
$E_{mid} = 86.9(17)$ MeV/u		$\Delta E = 357$ MeV			$R_{rms}^{\rho, (H-F)} = 3.06$ fm					
0.000	6.363	1d <sub>3/2</sub>	3.599	1.208	0.7	3.661	13.7	4.2	17.9	101.2
0.055	6.418	2s <sub>1/2</sub>	3.797	1.116	0.7	3.862	18.5	6.8	25.3	56.0
1.095	7.458	2p <sub>3/2</sub>	3.741	1.031	0.7	3.805	17.0	5.8	22.8	73.2
1.431	7.794	1f <sub>7/2</sub>	3.583	1.219	0.7	3.644	12.9	3.5	16.4	135.5
1.638	8.001	1d <sub>5/2</sub>	3.565	1.247	0.7	3.626	13.1	3.8	16.9	103.3
1.638	8.001	1d <sub>3/2</sub>	3.510	1.215	0.7	3.570	12.4	3.6	16.0	104.5
2.283	8.646	1d <sub>5/2</sub>	3.535	1.250	0.7	3.595	12.7	3.6	16.3	104.4
2.500	8.863	1d <sub>5/2</sub>	3.526	1.251	0.7	3.586	12.6	3.6	16.1	104.7
2.615	8.978	2s <sub>1/2</sub>	3.591	1.155	0.7	3.652	15.4	5.1	20.5	60.4
3.227	9.590	1d <sub>5/2</sub>	3.496	1.254	0.7	3.556	12.1	3.4	15.5	105.9
3.227	9.590	1d <sub>3/2</sub>	3.440	1.220	0.7	3.499	11.5	3.1	14.6	107.2
<b><math>{}^9\text{Be}({}^{32}\text{Mg}, {}^{31}\text{Mg})\text{X}</math></b>										
$E_{mid} = 76.6(15)$ MeV/u		$\Delta E = 393$ MeV			$R_{rms}^{\rho, (H-F)} = 3.15$ fm					
0.000	5.809	2s <sub>1/2</sub>	3.915	1.121	0.7	3.978	18.5	7.4	25.9	54.2
0.051	5.860	1d <sub>3/2</sub>	3.680	1.205	0.7	3.739	13.0	4.3	17.4	97.4
0.221	6.030	2p <sub>3/2</sub>	3.982	1.079	0.7	4.046	19.0	7.3	26.3	59.1
0.461	6.270	1f <sub>7/2</sub>	3.672	1.202	0.7	3.731	12.3	3.7	16.0	129.5
0.945	6.754	2s <sub>1/2</sub>	3.814	1.138	0.7	3.875	17.0	6.5	23.4	56.0
2.244	8.053	1d <sub>5/2</sub>	3.626	1.255	0.7	3.684	12.1	3.8	15.9	100.4

Table 1.5: Summary of calculated single-particle cross sections for neutron knockout from  ${}^{30,32}\text{Mg}$ . The left-most two columns give the excitation energy of the final state and the binding energy of the removed nucleon. The next five columns list the assumed single-particle state from which the neutron is removed along with the rms radius determined in a SkX Hartree-Fock calculation [8]. This group of five columns also includes Wood-Saxon parameters that match the Hartree-Fock radius and the resulting rms radius of the Wood-Saxon wavefunction. The calculated single particle cross sections for the stripping, diffractive, and total knockout cross section are listed in the next three columns. The last column gives the width (FWHM) of the longitudinal momentum distribution.

$\ell$	$\sigma_{sp}$ (mb)	$\frac{\partial\sigma_{sp}}{\partial a}$ (mb/fm)	$\frac{\partial\sigma_{sp}}{\partial R_{c-n}}$ (mb/fm)	$\frac{\partial\sigma_{sp}}{\partial R_c}$ (mb/fm)	$\frac{\partial\sigma_{sp}}{\partial E_{inc}}$ (mb/MeV/u)	$\delta a$ (fm)	$\delta R_{c-n}$ (fm)	$\delta R_c$ (fm)	$\delta E_{inc}$ (MeV/u)	$\delta\sigma_{sp}$ (mb)
0	36.0	-5.6	28.7	-11.5	-0.57	0.1	0.2	0.2	1.6	6.3
1	35.8	-4.5	28.7	-11.8	-0.57	0.1	0.2	0.2	1.6	6.3
2	21.7	-5.3	15.4	-9.1	-0.30	0.1	0.2	0.2	1.6	3.6
3	19.8	2.6	18.6	-8.9	-0.30	0.1	0.2	0.2	1.6	4.2

Table 1.6: Sensitivity of  $\sigma_{sp}$  to parameters. The sensitivity of the  $\ell=0-3$  single-particle cross sections for the  ${}^9\text{Be}({}^{28}\text{Ne}, {}^{27}\text{Ne}(\text{gs}))\text{X}$  reaction is deduced in a finite-difference analysis.

was changed from the Hartree-Fock calculated distribution to a Gaussian distribution with an rms radius scaled down by 5% from the Hartree-Fock value. The numerically determined sensitivities are given in table 1.6.

### 1.6.3 Example Case: Single-Neutron Knockout from ${}^{12}\text{Be}$

Previous measurements have been performed to study shell closures in exotic nuclei using single-neutron removal. One such example is the single-neutron knockout measurement from the  $N = 8$   ${}^{12}\text{Be}$  [45]. A level inversion is observed in the ground state of  ${}^{11}\text{Be}$  suggesting a weakened  $N = 8$  magic number for neutron-rich nuclei. To determine if the magic number is restored at  $N = 8$ , the single-neutron knockout reaction is applied to probe the single-particle structure of the  ${}^{12}\text{Be}$  ground state. If a strong  $N = 8$  shell closure exists at  ${}^{12}\text{Be}$ , the single-particle structure of the ground state should consist to a large extent of  $p$  shell neutron configurations with negative parity  $1/2^-$  and  $3/2^-$  state populated in the  ${}^{11}\text{Be}$  residue. However, results of the measurement show a strong population of the  $1/2^+$  ground state of  ${}^{11}\text{Be}$ . This qualitative results alone reveals the existence of a substantial intruder component in the  ${}^{12}\text{Be}$  ground state. However, comparison with the Eikonal reaction theory gives an observed spectroscopic strength of  $\approx 0.4-0.5$ . This quantifies the minimum occupancy in the  $sd$  shell, and comparison with structure calculations give a quantitative interpretation of the physics behind the weakened shell closure [45].

# Chapter 2

## Method

### 2.1 Overview of Technique

Nucleon knockout measurements are realized by transporting a radioactive ion-beam which includes the nuclide of interest  ${}^A_Z$  to the S800 spectrograph where it interacts with a light nuclear target. The reaction residues are magnetically analyzed in the S800 while coincident  $\gamma$  radiation is detected in the Segmented Germanium Array (SeGA), mounted around the reaction target. The single-neutron knockout reaction is tagged by detection of the  ${}^{A-1}_Z$  residue moving at approximately the velocity of the incident particle. The two most important observables in this work are partial cross sections to individual final states and longitudinal momentum distributions of reaction residues populating those states. The cross sections, along with a reaction model, provide spectroscopic information on the ground state of the parent nucleus, while momentum distributions provide information about the quantum state of the removed nucleon and also serve to verify the accuracy of the reaction model.

The partial cross sections are extracted in two steps. First, the inclusive cross section of the reaction is measured. This cross section is then multiplied by the branching ratio  $b_i$  to the final state of interest  $i$  to obtain the partial cross section  $\sigma_i$ , as illus-

trated in equation 2.1.

$$\sigma_i = b_i \sigma_{inc} \quad (2.1)$$

The inclusive cross section is the ratio of the reaction residue or fragment yield to the number of incident parent or beam nuclei, with target parameters included as shown in equation 2.2.

$$\sigma_{inc} = \frac{N_f}{N_b} \frac{1}{n x} \quad (2.2)$$

$N_f$  and  $N_b$  in equation 2.2 represent the reaction fragment yield and number of incident beam particles while  $n$  and  $x$  are the target number density and thickness. A 375 mg/cm<sup>2</sup> beryllium target is used in all measurements included in the present study. This target material and thickness gives a target factor of  $1/nx = 39.9(20)$  mb, where the uncertainty is dominated by the 5% tolerance in thickness quoted by the vendor.

The fragment yield and number of beam particles are then obtained according to equation 2.3.

$$N_i = \frac{N_{obs} DS}{N_{norm} \ell \epsilon} \quad (2.3)$$

The numerator includes the number of observed particles  $N_i$  and a down-scale factor  $DS$ , while the denominator includes a normalization factor  $N_{norm}$ , the data acquisition live time  $\ell$ , and a particle detection and identification efficiency  $\epsilon$ . The normalization factor  $N_{norm}$  is taken from the secondary beam rate measured with a beam timing scintillator placed upstream of the reaction target and integrated over the respective durations of data collection for  $N_b$  and  $N_f$ . This normalization is required because the number of incident beam particles and the reaction fragment yield are measured at different magnetic field settings in the spectrograph and, therefore, not simultaneously.

The detection efficiency depends on the efficiency of a number of detectors and is found to be sensitive to variations in the secondary beam rate. Data for the number of beam particles is collected at a much lower secondary beam rate, during data

collection runs referred to as normalization runs. During normalization runs, the spectrograph is set to transport the secondary beam to the focal plane, which has a maximum rate limit of  $\sim 6000$ - $10000$  particles/s. The low beam rate during normalization runs along with a simpler particle identification lead to a particle detection and identification efficiency that does not significantly deviate from 100%. This is not the case for the reaction fragment yield, measured in data collection runs referred to as fragment runs.

With the inclusive cross section measured, the fractional branching to individual final states must be determined to obtain partial cross sections. Final states are tagged during fragmentation runs by detection of de-excitation  $\gamma$ -rays. Gamma-ray intensities are extracted and normalized to the total number of reactions occurring during the data collection period. As states may be populated indirectly in  $\gamma$ -ray cascades, branching ratios to individual final states are determined by intensity balancing. Known level schemes are useful in this last step. However, as in the  $^{28}\text{Ne}$  case of this work, intensity balancing can be performed with no previous knowledge in cases where the  $\gamma$ -ray spectrum is simple.

As a final step, the branch to the ground state is determined by subtraction of the summed branches to all observed excited states. In performing this final step, one must always be aware of the possibility of populating excited states that are not tagged by coincident gamma radiation. This can occur, for instance, when long-lived excited states are populated and decay far away from the  $\gamma$ -ray detection array or when a populated excited state decays by emission of a  $\gamma$ -ray with energy either above or below the energy thresholds of the detector array. In such cases, the extracted “ground state” intensity includes contributions from both the ground state and any unobservable excited states. While analysis of the ground state momentum distribution may reveal untagged feeding to excited states, there is no absolute means by which such a scenario can be identified. Therefore, the possibility of unobserved indirect feeding to the ground state must always be considered while interpreting

results.

Momentum distributions corresponding to specific final states can also be extracted by tagging with observed  $\gamma$  radiation. Since  $\gamma$ -ray spectra obtained in knockout measurements often include a significant continuum distribution, a subtraction must be performed to obtain an accurate momentum distribution. Raw momentum distributions are extracted by gating on the photo-peak of interest and on a background-dominated region in the  $\gamma$ -ray spectrum. The background is taken from energies above the photo-peak to avoid the Compton-continuum of the transition of interest, but the proximity of the background gate to the photo-peak is sometimes limited by the complexity of the  $\gamma$ -ray spectrum. The background distribution is normalized, by analysis of the  $\gamma$ -ray spectrum, to match the estimated background contribution within the photo-peak gate and then subtracted from the photo-peak-gated distribution, yielding the true momentum distribution for the gated  $\gamma$ -ray transition. The ground state distribution is extracted by subtraction of all observed excited state distributions from the inclusive. This procedure is subject to the same pitfalls discussed in the previous paragraph. In more complex cases, distributions can likely not be extracted for all populated excited states. In these cases, the ground state distribution can not be accurately determined by the above prescription.

## 2.2 Radioactive Ion Beam Production

Radioactive ion beams (RIB) are produced at the Coupled Cyclotron Facility (CCF) at the National Superconducting Cyclotron Laboratory (NSCL). RIB production is achieved by fragmentation of a stable primary beam, and proceeds in three steps: primary beam production, fragmentation, and separation.

### 2.2.1 Primary Beam

Primary beam production begins inside the superconducting electron cyclotron resonance ion source (SC-ECR). Stable atoms in a gaseous state are ionized by collisions with fast-moving electrons which are driven by microwaves. Ions are extracted from the SC-ECR, and a single charge state is selected and transported to the first cyclotron.

The CCF makes use of a pair of cyclotrons, the K500 and K1200, to produce primary beams which have higher energies than are possible with a system employing a single cyclotron. Cyclotrons use a combination of static dipole magnetic fields and radio-frequency (RF) modulated electric fields to accelerate charged particles. The K number for each cyclotron refers to the maximum energy (in MeV) to which a beam of protons can be accelerated. However, for a given ion the maximum energy is proportional to the charge-squared-to-mass ( $Q^2/A$ ) ratio, the proton being the ideal case.

Acceleration in the coupled-cyclotron proceeds by first accelerating ions from the source to approximately 10% of the speed of light in the K500 cyclotron. This beam is then transported to the K1200 cyclotron. Upon injection into the K1200, the beam passes through a carbon stripper foil, in which a number of electrons are removed from the injected ions, increasing the  $Q/A$  ratio. The higher charge states created in this stripping process allow the K1200, in the final stage of primary beam production, to accelerate the primary beam to high energies on the order of 100-150 MeV/nucleon.

### 2.2.2 Fragmentation

After primary beam production, radioactive ions are produced by fragmentation of the primary beam. The primary beam is impinged on a production target, usually a thick beryllium plate, and a fraction of the nuclei in the primary beam collide with nuclei in the target. In these collisions the projectile nucleus shatters or fragments.

In most cases, the byproducts of this reaction include an exotic, or unstable, nucleus moving at approximately projectile velocity and with mass comparable to the incident primary beam particle.

### **2.2.3 Fragment Separation**

The fragmentation process results in a radioactive beam which includes a large number of nuclides. In most cases, the nucleus or nuclides of interest must be separated from the rest by electromagnetic analysis. This is achieved using the A1900 fragment separator [46]. The A1900 employs four  $45^\circ$  dipoles and a number of large-bore focusing magnets to achieve magnetic separation of the fragmented beam while preserving intensity. Upon magnetic analysis in the separator, the many species within the fragmented beam are spatially separated and the nucleus of interest is selected by use of collimating slits. The resulting ion beam is referred to as the secondary beam. In many cases, the nucleus of interest cannot be completely separated from other species in the fragmented beam. The secondary beam is then still a multi-component or cocktail beam but contains many less contaminants than the initial fragmented beam.

## **2.3 Experimental Device and Detector Setup**

After separation, the secondary beam is transported to the S800 spectrograph [47, 48] where it interacts with a reaction target situated at the target position, shown in figure 2.1. Subsequent reaction residues are analyzed in the spectrograph while coincident  $\gamma$  radiation is detected in the Segmented Germanium Array (SeGA) [49] mounted around the target.

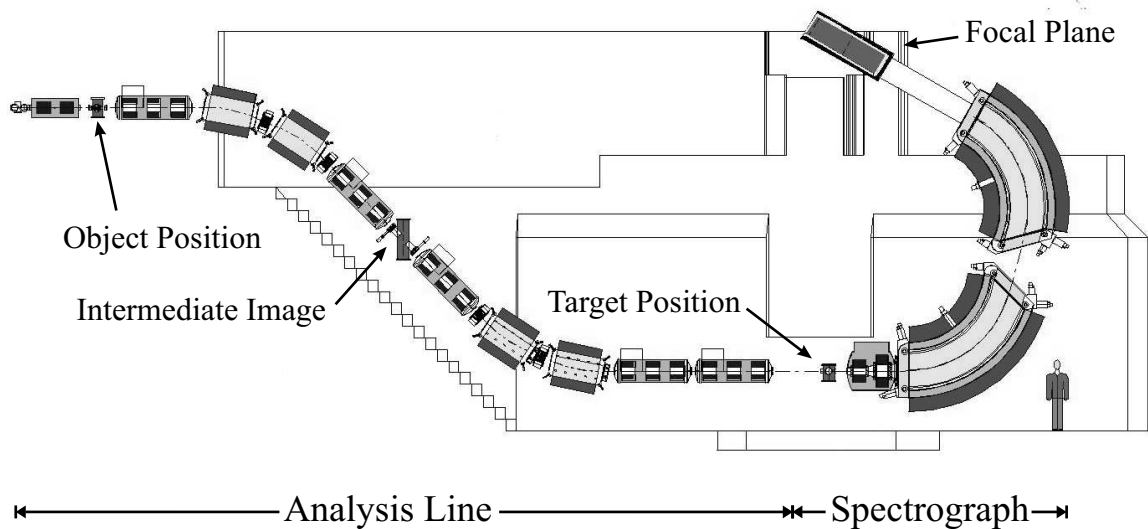


Figure 2.1: Schematic of the S800 Spectrograph.

### 2.3.1 The S800 Spectrograph

The S800 is a high-resolution magnetic spectrograph with a large acceptance, 20 msr angular and 5% momentum. As shown in figure 2.1, the spectrograph consists of two sections: the analysis line and the spectrograph. The analysis line can be operated in two optics modes: focused and dispersion-matched.

In focused mode, the analysis line is achromatic. This leads to a chromatic image at the focal plane of the spectrograph in which the momentum width of the incident beam is reflected in the resolution. This mode allows for a relatively large momentum acceptance of approximately  $\pm 2\%$ . However, tracking of the incident beam is necessary to recover momentum resolution at the focal plane of the spectrograph.

In dispersion matched mode, the optics of the entire device, analysis line and spectrograph, are set to be achromatic at the spectrograph focal plane, cancelling the momentum spread of the incident beam. In this mode, the beam is dispersed at the target position. The dispersion, which is approximately 10 cm per % momentum spread, leads to a constraint of approximately 0.5% full-width in momentum acceptance assuming a 5 cm wide reaction target.

## S800 Detector Setup

The detector setup for the S800 includes detectors located at the focal plane and the intermediate image. The focal plane detector setup, described in reference [47], provides particle identification and trajectory data at the focal plane. Progressing downstream, the setup includes two position-sensitive Cathode-readout Drift Chambers (CRDCs) separated by approximately one meter. The CRDCs each provide a two-dimensional position measurement and together provide a measure of particle trajectory. The CRDCs are followed by a segmented ionization chamber (IC) used to detect the energy loss of charged particles traversing the active volume of the detector. Finally, the IC is followed by three large-area plastic scintillators of thickness 5, 10, and 20 cm, progressing downstream. The signal from the 5-cm scintillator is used to trigger the S800 data acquisition.

The intermediate image detector setup includes two Parallel-plate Avalanche Counters (PPACs). Similar to the focal plane CRDCs, the PPACs each provide a two-dimensional position measurement and together provide a measure of the particle trajectory at the intermediate image. This trajectory is used to recover momentum resolution in experiments in which focused-mode optics are employed.

## Particle Identification

Particle identification (PID) is achieved on an event-by-event basis using a  $\Delta E$ -TOF method. The magnetic rigidity ( $B\rho$ ) in the spectrograph, which is directly proportional to the ratio of momentum to charge ( $p/Q$ ), is limited to a range of  $\pm 3\%$ . Therefore, ignoring deviations due to relativistic effects, the TOF spectrum for a beam of particles detected in the S800 focal plane would separate into loci corresponding to specific  $Q/A$  ratios. Energy loss  $\Delta E$  of a particle with charge  $Q$  when passing through a volume of material is known to be approximately proportional to  $Q^2$ . Therefore, a matrix of  $\Delta E$  versus TOF plotted for particles detected at the focal plane of the spectrograph should consist of loci corresponding to specific values of

$Q$  and  $A$ . For the nuclides discussed in the present work, the high secondary beam energy and relatively low atomic number  $Z$  allow for the assumption that  $Q = Ze$ , i.e. no charge states are considered.

While the  $\Delta E$  is measured in the focal plane ionization chamber, the TOF is measured between the first scintillator in the S800 focal plane and one of two plastic scintillators placed in the beam line upstream of the S800 analysis line: one at the A1900 extended focal plane (XFP) and one at the object of the S800 (OBJ). Since the data acquisition triggers on the focal plane scintillator, the TOF is measured as the duration between the trigger signal and the XFP and OBJ signals delayed by a fixed amount of time. Therefore, in plots of TOF, duration increases toward the left.

The large momentum acceptance of the spectrograph allows for a relatively large spread in TOF, possibly impacting the PID resolution. This resolution can be recovered by correcting the TOF for trajectory dependence. This is only necessary when the fragment of interest has broad position and angular distributions in the dispersive direction. For example, for a field setting in which unreacted secondary beam particles are transported to the focal plane, the detected fragments are well-confined in space and angle, and no trajectory correction is necessary for the TOF. Most reaction channels, including single-neutron removal, require trajectory corrections to produce a well-resolved PID.

### **Particle Identification Efficiency**

For fragment runs, PID requires data for  $\Delta E$ , OBJ-E1 TOF, and the trajectory of the particle at the focal plane. The efficiency of the PID is the product of the efficiencies of the timing scintillators, the ion chamber, and the focal plane CRDCs. The ion chamber and the E1 scintillator are assumed to be 100% efficient for particles with  $Z=10,12$ . These detectors in conjunction with the XFP scintillator are used to create an auxiliary PID for assessing the efficiency of the OBJ scintillator and the CRDCs. For the auxiliary PID a selection cut is made in  $\Delta E$ -XFP TOF.

A dispersive position is extracted from the up and down E1 scintillator signals with  $X_{\text{sc}} = \ln(E1(\text{up})/E1(\text{dn}))$ . A second cut is made in XFP TOF- $X_{\text{sc}}$ . Although the auxiliary PID is not as pure as the primary PID, it is sufficient to estimate the efficiency. The OBJ efficiency and the correlated efficiency for both CRDCs is extracted within the the auxiliary PID. An additional correction is included to account for the correlated XFP-OBJ efficiency.

### Momentum Reconstruction

As opposed to actively correcting aberrations in the magnetic field of the spectrograph, analytical techniques are employed to reconstruct particle trajectories at the target position. This analytical technique makes use of measured maps of the field in the spectrograph as input into the COSY infinity code [48, 50]. Using COSY infinity, inverse maps are calculated which relate the measured particle trajectory at the focal plane to the trajectory at the reaction target as shown in equation 2.4.

$$\begin{pmatrix} a_t \\ y_t \\ b_t \\ d_t \end{pmatrix} = S^{-1} \begin{pmatrix} x_f \\ a_f \\ y_f \\ b_f \end{pmatrix} \quad (2.4)$$

In equation 2.4,  $x$  ( $y$ ) represents the dispersive (non-dispersive) position,  $a$  ( $b$ ) represents the dispersive (non-dispersive) angle,  $d$  represents the deviation of the energy from the central energy of the spectrograph, and the subscript  $f$  and  $t$  represent focal plane and target parameters, respectively. All inverse maps are calculated to fifth order since higher order terms give corrections comparable to deviations stemming from the position resolution of the CRDCs.

To accurately reconstruct the particle trajectory at the reaction target, the focal plane CRDCs must be properly calibrated. The non-dispersive position is measured by drift time of ionization electrons, while the dispersive position is measured from

the distribution of image charges of the avalanche on pads mounted along the anode wire. The CRDCs are calibrated by collimating a beam of particles with a mask. The absolute positions of the holes in the mask are known, and a relationship between pad number (drift time) and dispersive (non-dispersive) position is extracted by means of a statistical fit. The pitch of the pads is known and is, therefore, fixed in the fit.

### Acceptance Corrections

When measuring cross sections and longitudinal momentum distributions, the acceptance of the spectrograph must be considered. The angular distribution of the knockout fragments should be azimuthally symmetric. However, the acceptance of the focal plane is not symmetric in this dimension. Therefore, acceptance is calculated as a function of longitudinal momentum  $P_{//}$  and scattering (polar) angle  $\theta_{sc}$  and applied on an event-by-event basis to account for acceptance losses.

The acceptance is calculated in a Monte Carlo simulation in which particles of mass  $A$  and charge  $Q$  are tracked through the known geometry and fields of the spectrograph. Particles are assumed to start at the target position and a relevant region of the  $(P, \theta, \phi)$  space is sampled where  $P$ ,  $\theta$ , and  $\phi$  are the momentum, dispersive angle, and non-dispersive angle, respectively. From the Monte Carlo data, a two-dimensional matrix of acceptance is generated with longitudinal momentum and total scattering angle on the axes.

Previous analyses and also the analysis of the single-neutron removal from  $^{26}\text{Ne}$  in the present study employ a more simple procedure to estimate the acceptance correction. A Monte Carlo simulation is used as discussed above, but the transverse component of the momentum is sampled from a distribution which is taken from the data and is assumed to be the same for all longitudinal momenta. In the procedure discussed above, used for the  $^{28}\text{Ne}$  and  $^{30,32}\text{Mg}$  analyses, the dependence of the angular distribution of the reaction fragments on the longitudinal momentum is explicitly taken into account.

Plotted as a function of  $P_{//}$ , the limits of acceptance are defined, for the purposes of the present measurements, as the region in which calculated corrections are less than 50%, i.e. two-thirds of the fragments reach the focal plane. Corrections due to the acceptance of the spectrograph can be treated in two regimes: calculated corrections within the acceptance and extrapolated corrections beyond the acceptance. The former are treated quantitatively according to the above discussed prescription. However, the extrapolated correction relies on knowledge of the behavior of the  $P_{//}$  distribution beyond the limits of acceptance. Although the high- $P_{//}$  side of these distributions have shown good agreement with model predictions, the low- $P_{//}$  side often includes tails which noticeably deviate from predictions. This deviation limits the accuracy of the extrapolated correction.

### Momentum reconstruction and acceptance in Focused Mode

For the  $^{28}\text{Ne}$  and  $^{30,32}\text{Mg}$  measurements, the S800 spectrograph was operated in focused-mode. In this mode, unlike the dispersion-matched setting, the beam is focused at the reaction target. This allows for a momentum acceptance as high as 2% FWHM. However, with this setting there is no optical compensation for the momentum spread of the incoming secondary beam. Therefore, the momentum of the projectile must be measured to achieve reasonable resolution in the momentum distribution of the reaction products.

In focused mode, the momentum of secondary beam particles is proportional to their dispersive angle  $\theta_{Im}$  at the intermediate image. According to optics calculations the proportionality is approximately 52 mrad/%. The  $\theta_{Im}$  angle is measured at the intermediate image with a pair of position-sensitive PPACs, and the proportionality is calibrated experimentally using data from normalization runs.

During normalization runs, the magnetic rigidity of the spectrograph is set to guide the secondary beam to the focal plane after passing through the reaction target. Figure 2.2 shows plots of the longitudinal momentum  $P_{//}$  measured at the focal plane

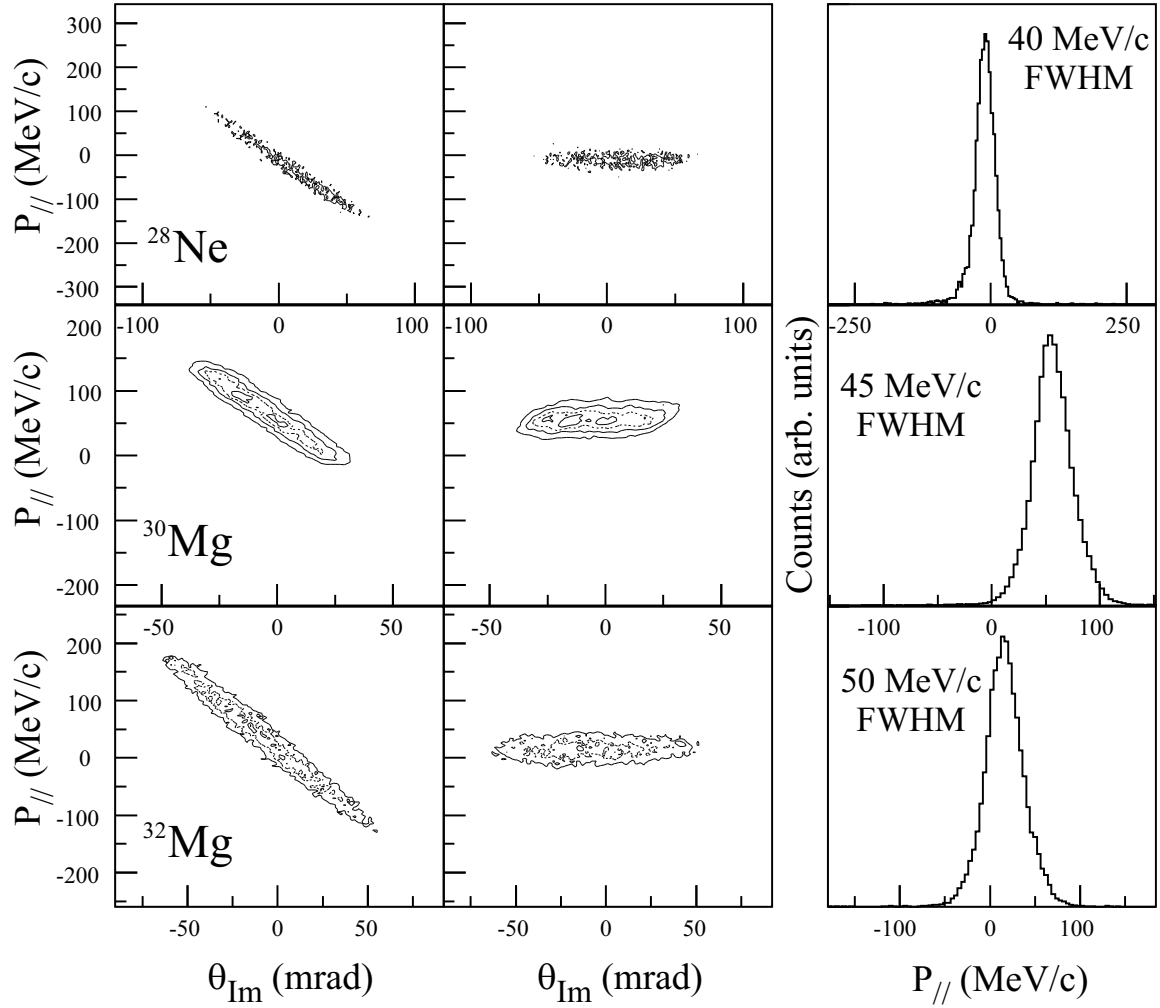


Figure 2.2: Summary of corrected longitudinal momentum for  $^{28}\text{Ne}$  (upper)  $^{30}\text{Mg}$  (middle)  $^{32}\text{Mg}$  (lower). The column on the left show plots of longitudinal momentum versus the dispersive angle  $\theta_{Im}$  at the intermediate image. The center column shows plots of the corrected longitudinal momentum as a function of  $\theta_{Im}$ . The column on the right gives corrected longitudinal momentum distributions and are inset with the measured momentum resolution for each beam.

as a function of the dispersive angle measured at the intermediate image for  $^{28}\text{Ne}$  and  $^{30,32}\text{Mg}$ . A corrected longitudinal momentum is defined by

$$P_{//}^{\text{CORR}} = P_{//} + \alpha \theta_{Im} \quad (2.5)$$

where  $\alpha$  is a correlation coefficient to be determined for each setting.

The coefficients are determined for each setting by minimizing the width of the

corrected longitudinal momentum distribution, also shown in figure 2.2. They are found to be 2.1, 2.5, and 2.6  $\frac{\text{MeV}/c}{\text{mrad}}$  for  $^{28}\text{Ne}$ ,  $^{30}\text{Mg}$ , and  $^{32}\text{Mg}$ , respectively. For comparison to the estimated 52 mrad/% from the optics calculations, these values correspond to 52, 47, and 45 mrad/%, respectively. The corrected distributions give a direct measure of the momentum resolution: 40, 45, and 50 MeV/c (FWHM) for the  $^{28}\text{Ne}$ ,  $^{30}\text{Mg}$ , and  $^{32}\text{Mg}$  measurements, respectively.

The correction based on  $\theta_{Im}$  to the longitudinal momentum distribution leads to an acceptance effect beyond that described in section 2.3.1. The acceptance window shifts as a function of image angle as shown in figure 2.3. This effect is treated in a geometric approach. The acceptance takes the form of a parallelogram in the corrected  $P_{//}$  vs.  $\theta_{Im}$  matrix. The diagonal lines are defined by acceptance limits determined as described in 2.3.1. Projecting onto the corrected  $P_{//}$  axis within this matrix, the center of the distribution is free of any cuts in  $\theta_{Im}$ . However, the wings of the corrected momentum distribution are subject to sharp cuts in  $\theta_{Im}$  and acceptance corrections are necessary. The acceptance correction is determined as a function of the corrected momentum by first determining the region of  $\theta_{Im}$  acceptance and then integrating the inclusive  $\theta_{Im}$  distribution over this region to find the fraction of the distribution included. This fraction is a good approximation of the fractional acceptance for the given corrected momentum. Similar to the limit defined in section 2.3.1, an acceptance region is defined in which at least two-thirds of the  $\theta_{Im}$  distribution is sampled, i.e. the correction is no more than 50%.

### 2.3.2 Segmented Germanium Array (SeGA)

The segmented germanium array (SeGA) [49] is placed around the reaction target for detection of coincident  $\gamma$ -ray radiation. SeGA is an array of eighteen cylindrical 32-fold segmented high-purity germanium detectors designed for detection of  $\gamma$ -rays emitted from high velocity sources. Each crystal is 7 cm in diameter and 8 cm long with segmentation into eight slices and four quadrants as is shown in figure 2.4. In

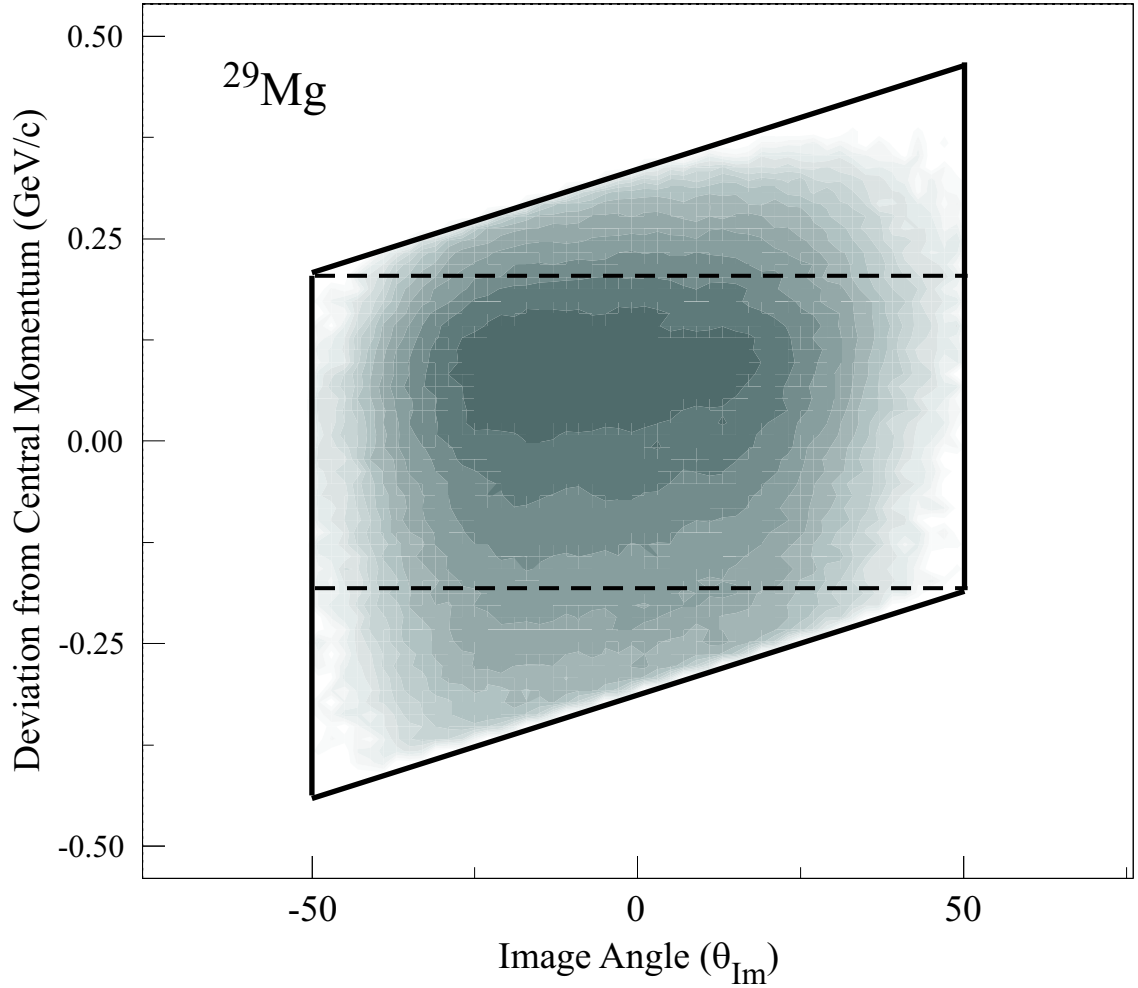


Figure 2.3: S800 acceptance window after  $\theta_{Im}$  correction. The corrected longitudinal momentum is plotted against the intermediate image angle  $\theta_{Im}$ . The acceptance window takes the form of a parallelogram in this matrix. No acceptance corrections are needed between the dashed lines, but corrections are applied outside of this region.

Det.	$\theta$ [deg]	$\phi$ [deg]	Det.	$\theta$ [deg]	$\phi$ [deg]	Det.	$\theta$ [deg]	$\phi$ [deg]
1	24	180	9	29	91	17	24	1
2	40	131	10	78	91	18	60	61
3	90	112	11	126	90	19	139	46
4	147	143	12	126	272	20	147	323
5	139	228	13	78	270	21	90	292
6	60	241	14	29	271	22	40	310

Table 2.1: Summary of  $\delta$ -SeGA configuration. Detectors are numbered from 1 to 22 with 7, 8, 15, and 16 providing spare electronics channels. Positions of the center of each crystal are reported here. The inclination with respect to the beam axis is given as  $\theta$  while the azimuthal angle is represented by  $\phi$ . The beam axis is at  $\theta = 0$ , and  $\phi = 0$  is defined as up, i.e. opposite to gravity.

most cases, the array is configured such that the full length of the symmetry axis of each crystal is approximately equidistant from the  $\gamma$ -ray source, usually the reaction target, and at constant azimuth with respect to the source trajectory, usually the beam axis.

### Configurations of the Array

Two configurations of the array are employed during this work. For the  $^{26}\text{Ne}$  single-neutron removal measurement, SeGA is arranged in the classic configuration, while, for the  $^{28}\text{Ne}$  and  $^{30,32}\text{Mg}$  measurements the  $\delta$  configuration was used. In the classic configuration, the array is arranged in two rings with eight detectors at  $37^\circ$  with respect to the beam axis and ten detectors at  $90^\circ$ . During the  $^{26}\text{Ne}$  measurement, only fifteen detectors were available, and the array consisted of seven  $37^\circ$  detectors and 8  $90^\circ$  detectors. The  $\delta$ -configuration, which is designed for the measurement of angular distributions of  $\gamma$ -rays from fast-moving sources, consists of eighteen detectors arranged in nine angle pairs as shown in table 2.1. During the  $^{28}\text{Ne}$  and  $^{30,32}\text{Mg}$  measurements all eighteen detectors were installed and used.

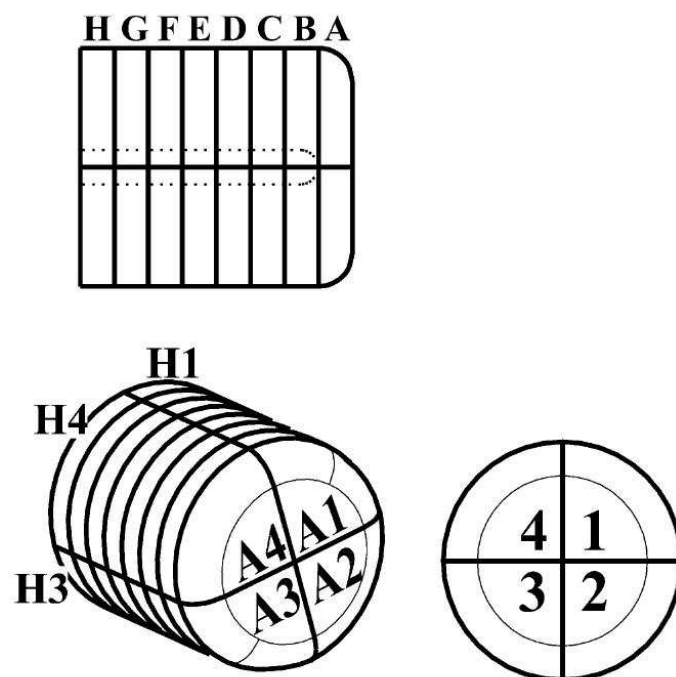


Figure 2.4: Schematic of SeGA crystal. The cylindrical high-purity germanium crystal is electronically segmented into eight slices, labeled A-H, and four sections, labeled 1-4, giving a total of 32 segments per detector.

## Calibrations

For SeGA, the energy from both the central contact and the segments must be calibrated. The central contact energy is calibrated using a number of radioactive sources. Calibration data are collected and photo-peaks in the resulting raw spectrum for each detector are fit with Gaussian distributions plus a second order polynomial background. The set of photo-peak centroids and known energies are statistically fit with a second order polynomial to calibrate the central contact energy. For the  $^{30}\text{Mg}$  measurement with higher  $\gamma$ -ray energies expected, the calibration data are fit with two connected first order polynomials to ensure that extrapolation of the calibration does not diverge quadratically beyond the last data point at 3.5 MeV. Energy calibration of the individual segments is accomplished using the automated technique discussed in reference [51].

The photo-peak detection efficiency of SeGA is measured using five calibration sources, listed in tables 2.2 and 2.3. Of the five, the  $^{152}\text{Eu}$ ,  $^{133}\text{Ba}$ , and the mixed source had known activity while the  $^{226}\text{Ra}$  and  $^{56}\text{Co}$  did not. Each source was mounted on the target holder and placed in the center of the germanium array at the target position. One to two hours of data were collected for each source in  $\gamma$ -singles mode. The resulting  $\gamma$ -ray spectra were analyzed on a detector-by-detector basis. Photo-peak intensities are extracted by means of a background-subtracted summation of the counts within the photo-peak. The background was determined by a statistical fit of a skewed Gaussian plus quadratic background to the photo-peak. The detection efficiency of the entire array is extracted as shown in equation 2.6. For each  $\gamma$ -ray the intensities  $I(E_\gamma)$  from each detector are summed and corrected by the data acquisition live time  $\ell$  to yield the total intensity. The efficiency is then calculated by dividing the total intensity by the number of  $\gamma$ -rays of energy  $E_\gamma$  emitted, determined by multiplying the source activity  $A_0$  by the duration  $T$  of the collection period and the branching ratio  $b(E_\gamma)$  through the transition.

$$\epsilon_{photo}(E_\gamma) = \frac{\sum_i I_i(E_\gamma)}{\ell b(E_\gamma) A_o T} \quad (2.6)$$

To extend the efficiency measurement to  $\gamma$ -ray energies beyond 1.4 MeV, it is necessary to use the uncalibrated sources. A pseudo-efficiency is extracted for the uncalibrated data points using equation 2.6 with  $A_o = 1$ . A simultaneous least squares fit is then performed with both the calibrated and uncalibrated data points. The model includes a normalization parameter for each of the five sources and two common parameters to define the shape of the efficiency curve as shown in equation 2.7. The extracted normalization for the three calibrated sources are all in agreement with each other, and an average normalization is extracted from these three parameters. The efficiency measurements from each source are then normalized using the average normalization, resulting in a global 3% reduction in the  $^{152}\text{Eu}$  measurement, a 3% increase for  $^{133}\text{Ba}$ , and a 1% reduction for the  $^{137}\text{Ce}$ , all within the uncertainty limits of the respective  $\gamma$ -ray sources. The corrected efficiency measurements for all sources, calibrated and uncalibrated, are shown in figure 2.5.

$$f(x) = (x + p_1)^{-p_2} \quad (2.7)$$

### Detector Saturation Deadtime

The interaction of the secondary beam with the reaction target results in a forward-focused spray of high-energy particles. The interaction of this spray with the germanium detectors can lead to large energy deposition resulting in a saturation of the electronics for periods on the order of microseconds to milliseconds. While saturated, no  $\gamma$ -rays can be observed. To measure this physical dead time, gamma singles data were collected with and without the secondary beam incident on the reaction target. On a detector-by-detector basis, the rates of detected 1460-keV potassium background photo-peak events were extracted for in-beam and no-beam measurements, and the

NSCL Src ID	Species	Activity ( $\mu\text{Ci}$ )	Ref. Date	$E_\gamma$ (MeV)	Branch (%)
E2880	$^{152}\text{Eu}$	14.64(54)	1 Nov 1988	244.7	7.53(4)
				344.3	26.57(11)
				778.9	12.97(6)
				964.1	14.63(6)
				1112.1	13.54(6)
				1408.0	20.85(9)
E2878	$^{133}\text{Ba}$	12.80(36)	1 Nov 1988	276.4	7.147(30)
				302.9	18.30(6)
				356.0	61.94(14)
				383.8	8.905(29)
H7141	$^{137}\text{Ce}$ (Mixed)	2423*	9 May 2000	661.6	

\*Mixed source activity measured in  $\gamma$ -rays per second.

Table 2.2: Calibrated sources used to measure the photo-peak detection efficiency of SeGA.

Species	$E_\gamma$ (MeV)	Branch (%)	Species	$E_\gamma$ (MeV)	Branch (%)
$^{226}\text{Ra}$	609.3	46.1(5)	$^{56}\text{Co}$	846.8	99.933(7)
	768.4	4.94(6)		1037.8	14.13(5)
	934.1	3.03(4)		1238.3	66.07(19)
	1120.3	15.1(2)		1360.2	4.256(15)
	1238.1	5.79(8)		1771.3	15.49(5)
	1729.6	2.92(4)		2598.4	16.96(6)
	1764.5	15.4(2)		3201.9	3.13(9)
	2293.4	0.305(9)			
	2447.9	1.57(2)			

Table 2.3: Uncalibrated sources used to measure the photo-peak detection efficiency of SeGA.

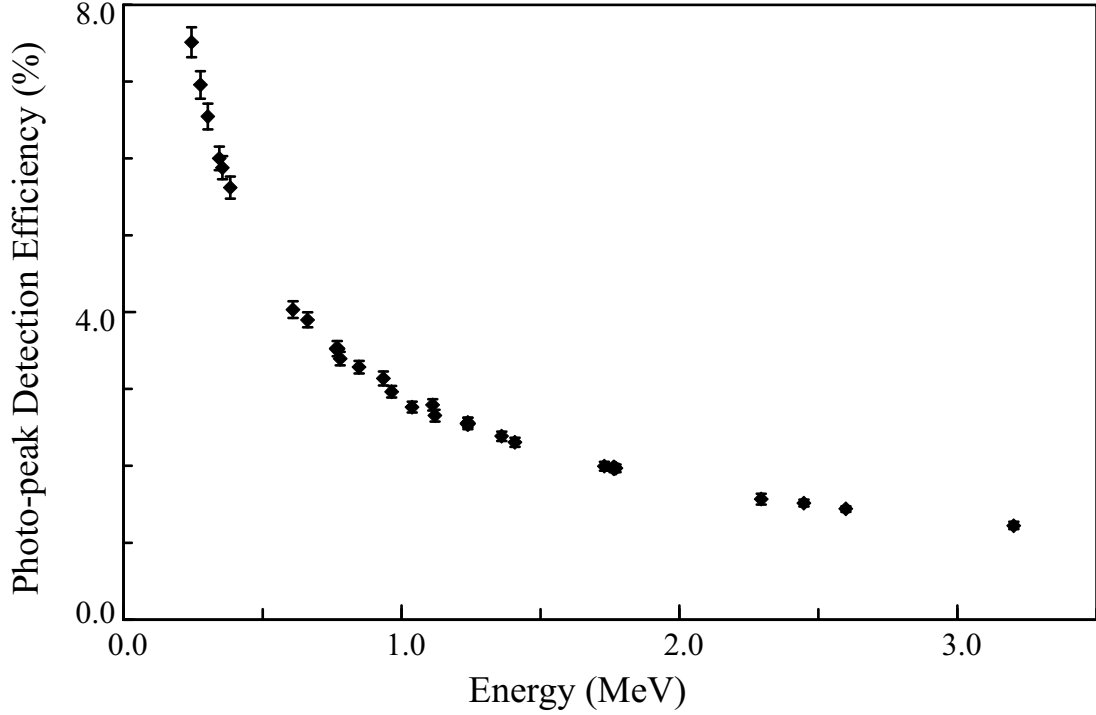


Figure 2.5: Measured photo-peak detection efficiency of SeGA.

ratio taken as the fraction of time that the detector was alive. In the present work, no significant detector dead times were observed. This small effect is attributed to lower secondary beam rates than in measurements in which a significant detector dead time has been observed.

### Doppler Reconstruction

The energy of  $\gamma$ -rays emitted from relativistic particles are subject the the Doppler effect. To produce a  $\gamma$ -ray energy spectrum that accurately portrays the level structure of a nucleus, observed  $\gamma$ -rays must be Doppler corrected to determine the energy in the rest frame of the emitting nucleus. The Doppler effect depends on two parameters: the source velocity and the angle of emission relative to the velocity. Doppler reconstruction is performed using equation 2.8.

$$E_{dopp} = E_{lab} \gamma (1 - \beta \cos(\theta)) \quad (2.8)$$

$E_{dopp}$  and  $E_{lab}$ , in equation 2.8, respectively represent the Doppler-reconstructed  $\gamma$ -ray energy and the energy observed in the laboratory. The  $\gamma$  and  $\beta$  parameters are relativistic variables associated with the moving  $\gamma$ -ray source, and  $\theta$  is the angle between the source momentum and emitted  $\gamma$ -ray in the laboratory frame of reference.

Energy resolution in the Doppler-reconstructed spectrum is dominated by uncertainty in  $\beta$  and  $\theta$ . Since the velocity of the fragment changes inside the reaction target, the velocity used for the Doppler-reconstruction is assumed to be the mid-target value  $\beta_{mid}$ , yet the true velocity ranges, in an approximately flat distribution, from the incoming beam velocity  $\beta_{beam}$  to the post-target velocity  $\beta_{out}$ . The angle of emission is calculated as the angle between the beam axis and the trajectory extending from the center of the reaction target to the center of the germanium segment in which the  $\gamma$ -ray is detected. Since a single  $\gamma$ -ray often interacts at several points in several segments in a single SeGA detector, the position is taken from the segment in which the largest amount of energy is deposited. The emission angle determination is subject to the granularity of the segmented germanium detectors. The SeGA detectors are general placed such that the 1 cm width of the segments along the symmetry axis define the opening angle. With detectors positioned approximately 25 cm from the reaction target, as they are for this work, the measured emission angle is subject to a flat distribution of width 40 mrad. The scattering angle of the fragment is also a source of uncertainty but is generally not significant compared to velocity and granularity effects. The intrinsic resolution of the germanium crystal also has a negligible contribution to the uncertainty in the Doppler reconstruction. With equation 2.8 and estimated RMS deviations for the velocity and angle, the resolution of the Doppler reconstruction can be estimated as shown in figure 2.6.

Physical parameters used for the Doppler reconstruction include the mid-target fragment velocity, the three-dimensional position of the center of the target, and the three dimensional position of each germanium segment. The velocity can be estimated rather accurately using the measured fragment momentum in the spectrograph and

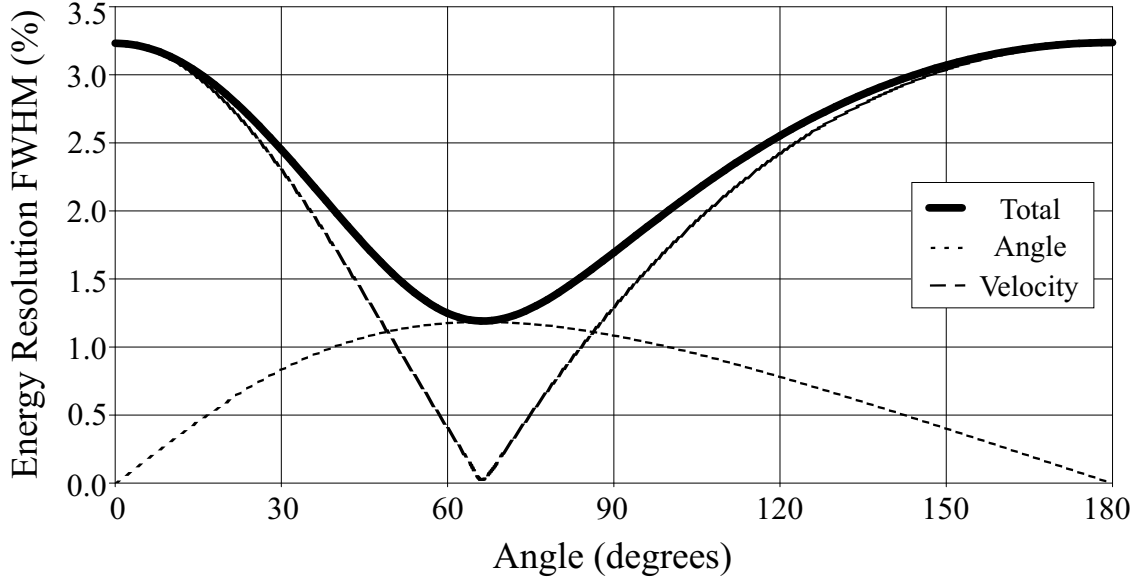


Figure 2.6: Estimated SeGA energy resolution at 1.3 MeV. The dashed (dotted) line represents the contribution to the resolution from the energy loss in the target (open angle of the segments) plotted against the angle with respect to the beam axis. The solid line is the total estimated resolution which also includes a negligible contribution from the intrinsic resolution of the germanium detector.

back-calculating for energy loss through half of the target. The target position is assumed to be the fixed position around which SeGA is positioned during the setup of the experiment. The segment positions were previously measured relative to fixed positions on the exterior of the detector. The position and orientation of each detector is then measured with respect to the target position using surveying scopes, called theodolites. The segment positions are fixed throughout the experiment.

The velocity and the target position parameters are refined in an iterative process by analysis of the Doppler-reconstructed spectrum for each detector. The target position is initially assumed to be at the origin while an initial guess for the velocity is taken from the fragment momentum. The centroid of a strong, sharp photo-peak of known energy is found in the Doppler-reconstructed energy spectrum for each detector. These centroids likely deviate from the known energy, and new parameters are determined that minimize the sum of the squared deviation of the centroid from the known value. This process generally converges after 2-3 iterations with an rms

deviation of a few keV.

For ion beams with velocities on the order  $0.3c$ - $0.4c$ , the Doppler-reconstruction is sensitive to half-lives of emitting states in the range of a few picoseconds up to several nanoseconds. The reaction target used in the present work is a 2 mm thick beryllium plate. At one-third of the speed of light an ion traverses half the target thickness in ten picoseconds. So, for emitting states with half-lives on the order of a few picoseconds, most  $\gamma$ -rays are still emitted from the target, introducing no significant deviation in the emission angle determination. However, the velocity distribution of the emitting particle gets more narrow and is shifted to lower velocities. The result is an observed photo-peak that is narrower than expected. This changing width is illustrated in figure 2.7. For longer half-lives on the order of hundreds of picoseconds, the majority of  $\gamma$ -rays are emitted downstream of the target at a distances subject to an exponential distribution. Although the velocity distribution is now very narrow and centered at  $\beta_{out}$ , large errors in the assumed emission angle lead to a low-energy skew in the Doppler-reconstructed photo-peak. This is illustrated by the rising full-width at one-tenth of the maximum, also plotted in figure 2.7.

For spectra in which the background on which such skewed peaks sit is understood, an analysis of the shape of the Doppler-reconstructed photo-peak gives a reasonable measure of the half-life of the emitting state. In cases, where no such lifetime effects are noted in the photo-peak resolution or shape, an upper limit of approximately 40 ps can be placed on the half-life of the emitting source.

## Simulated Response Functions

Due to the interplay between the Doppler boost and the energy-dependent  $\gamma$ -ray detection efficiency of SeGA, a simulation is used to calculate the response function of the array to  $\gamma$  radiation. The simulation is built from the GEANT3 code and accounts for the geometry of the array, beam pipe, and reaction target. The simulation also includes a Lorentz boost due to the relativistic velocity of the emitting source as well

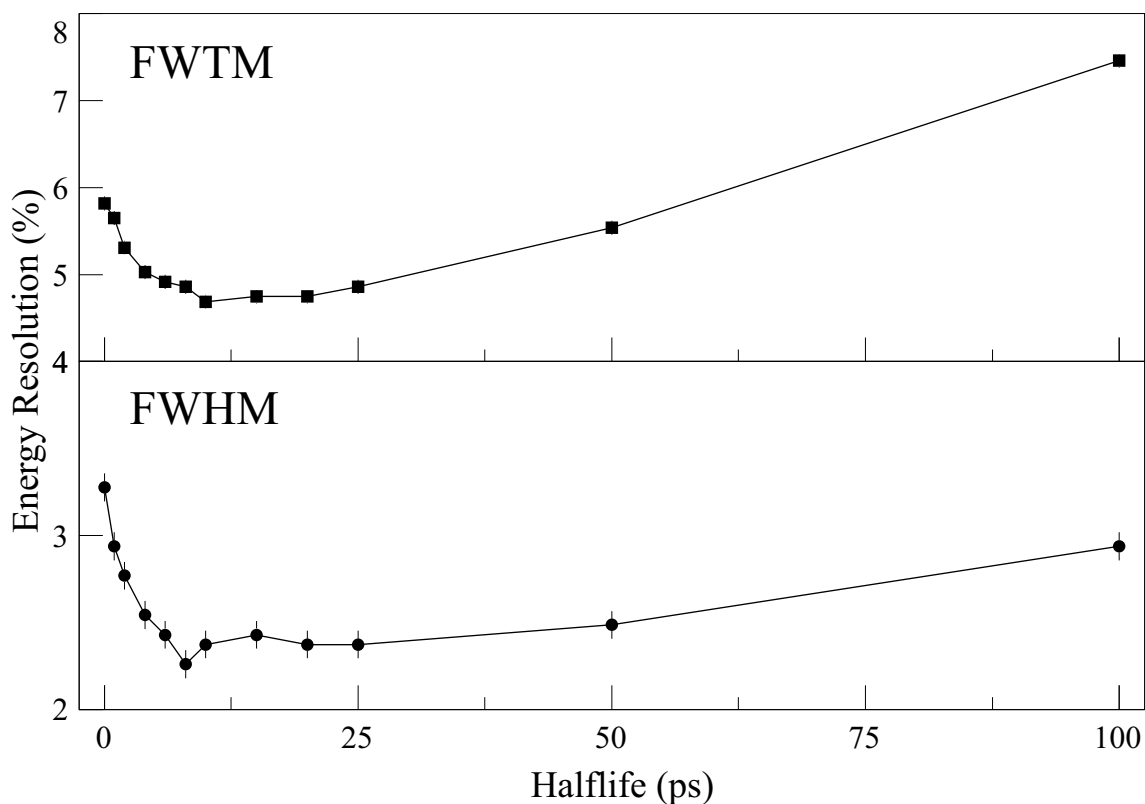


Figure 2.7: Simulated SeGA energy resolution vs. half-life. The full width at half maximum (FWHM, lower panel) and one-tenth (FWTM, upper panel) of simulated Doppler-reconstructed 0.885-MeV photo-peaks are plotted for a number of half-lives up to 100 ps. The post-target fragment velocity is used for the Doppler correction. The FWHM clearly falls to a minimum value at  $\sim 10$  ps where most particles are decaying with  $\beta = \beta_{out}$ . The FWHM is roughly constant up to  $\sim 25$  ps, where half-life effects on the angular reconstruction start to become significant. The FWTM follows this trend as well but shows a more dramatic increase starting at 25 ps.

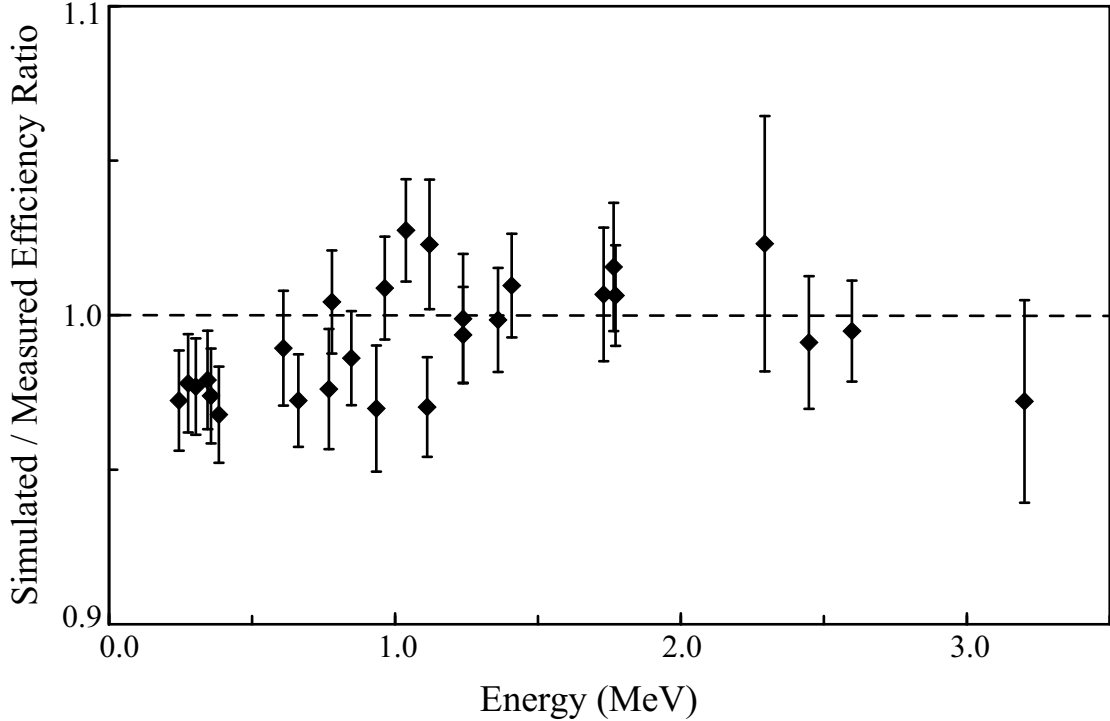


Figure 2.8: Ratio of simulated to measured photo-peak detection efficiency.

as any non-negligible lifetime of the emitting state. The  $\gamma$ -ray angular distribution is assumed to be isotropic in the projectile frame and is properly Lorentz boosted to produce a forward-focused distribution in the lab frame. The detector geometry within the simulation is based on design specifications provided by the manufacturer. However, with this geometry, the simulation over-predicts the photo-peak efficiency of the array at both low and high  $\gamma$ -ray energies. To resolve this, the radius of the active region of the germanium crystal was decreased leaving a dead layer of germanium around the active volume. The radius of the crystal is fixed while the radius of the active volume is adjusted to match the measured photo-peak efficiency. The ratio of the simulated to measured photo-peak efficiency is plotted in figure 2.8 using an active volume radius of 3.387 cm, which gives the most favorable comparison. The simulated efficiency agrees with the measured value to an accuracy of 3%, which defines our systematic uncertainty in measured  $\gamma$ -ray intensities. There appears to be a systematic deviation at low  $\gamma$ -ray energy. Therefore, the efficiency is not extrapolated below 0.25 MeV.

## 2.4 Data Acquisition Trigger

The data acquisition system (DAQ) consists of a combination of the S800 and SeGA data acquisition systems. To work together, these two systems must share the same triggering mechanism. The trigger allows for three possible triggering conditions: particle single (PS), gamma single (GS), and coincidence (COINC). For the  $^{28}\text{Ne}$  and  $^{30,32}\text{Mg}$  measurements two additional conditions were available to accommodate in-beam calibration measurements of the CRDC drift times, but these triggers will not be discussed further.

The PS trigger is taken from the timing signal of the first scintillator in the S800 focal plane, while the GS trigger is taken from a logical OR of all the individual germanium timing signals. The COINC trigger is taken from a coincidence between the PS and GS trigger with a coincidence window of approximately 400 ns. Due to difference in response time for the PS and GS trigger, delays must be added to properly correlate particle/ $\gamma$ -ray coincidences. The delays are tuned for each experiment to place the prompt  $\gamma$ -ray time peak close to the beginning of the coincidence window.

In GS mode, used to record calibration data for SeGA, it is not necessary to read and record data from the S800 electronics. Doing so leads to increased DAQ dead time and perhaps larger uncertainty in photo-peak efficiency measurements. Therefore, the DAQ software is designed to take trigger-specific action such that for a GS event only the SeGA electronics are read. For both the PS and COINC triggers all electronics are read. An oversight in the DAQ programming led to a situation in which COINC triggers were registered but occasionally the GS action was taken, resulting in the loss of S800 data for these events.

To understand this bug, it is necessary to understand that a COINC event is simultaneously a PS and a GS event. Over the course of the  $^{28}\text{Ne}$  and  $^{30,32}\text{Mg}$  measurements, it was necessary to record GS data while collecting statistics on the reactions of interest. To avoid overwhelming the DAQ with GS events, a down-scaler

factor of 30 was applied to this trigger, i.e. only one in thirty GS events were registered as a GS trigger. Therefore, approximately one in thirty COINC events were also registered as GS events, and in these cases the S800 data were discarded leading to an approximate 3% correction that must be applied to the normalization of COINC events gated on S800 PID data.

### 2.4.1 Normalization of $\gamma$ -Ray Intensities

Gamma-ray intensities are determined by a statistical fit of simulated response functions and an appropriate background to observed  $\gamma$ -ray spectra. The response function is generated in a simulation as described in the previous section. Since the simulation is adjusted to match the measured photo-peak detection efficiency, the fit gives the absolute number of  $\gamma$ -rays emitted or the total yield,  $N_\gamma$ . To deduce the absolute  $\gamma$ -ray intensity, the yield must be normalized by the number of reactions, which is measured by counting the number of reaction by-product observed while collecting particle- $\gamma$  coincidences. In the simplest case, when all particle data are recorded while collecting coincidences, the intensity is normalized by dividing by the total number of reaction fragments  $N_\gamma$ . However, in cases where coincidences are collected using a particle- $\gamma$  coincidence trigger and particle-singles are collected subject to a down-scaler, the number of reactions must be corrected for the down-scale factor and the DAQ livetime (since the coincidence and particle-singles triggers are subject to differing livetimes due to the down-scaler). The  $\gamma$ -ray intensity is then given by equation 2.9 where  $\ell_{\text{COINC}}$  and  $\ell_{\text{PS}}$  represent the coincidence and particle-single livetimes and  $DS$  is the down-scale factor. In the simplest case the livetimes are identical and the down-scale factor is unity.

$$I_\gamma = \frac{N_\gamma}{\ell_{\text{COINC}}} \frac{\ell_{\text{PS}}}{N_f DS} \quad (2.9)$$

# Chapter 3

## Analysis and Experimental Results

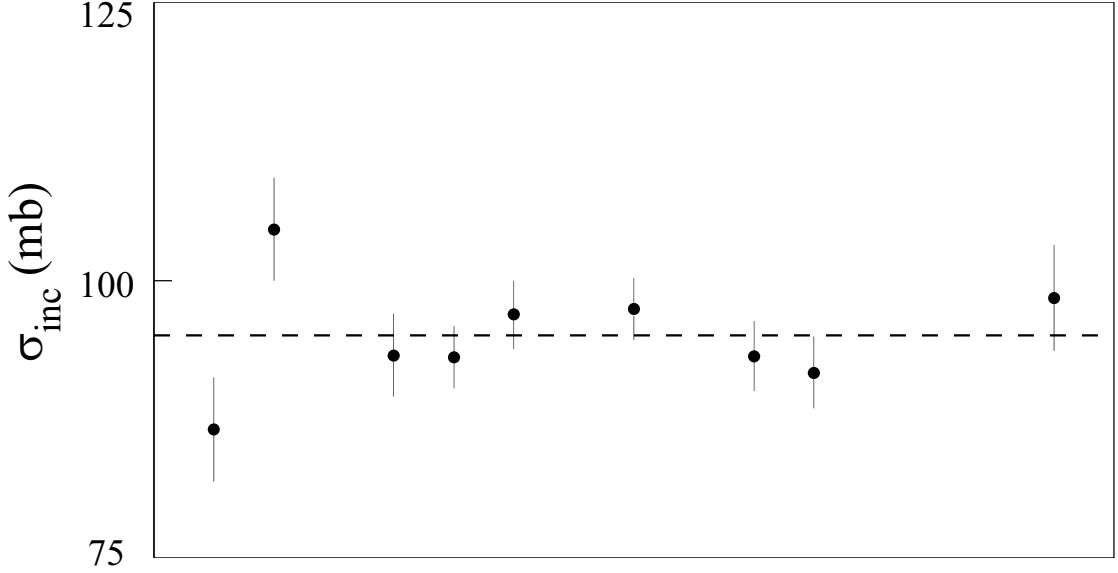
### 3.1 Single-Neutron Removal Data from $^{26}\text{Ne}$

#### 3.1.1 Inclusive Cross Section

The inclusive cross section for the  $^9\text{Be}(^{26}\text{Ne},^{25}\text{Ne})\text{X}$  reaction is determined to be 98(5) mb. This value is reached using equation 2.2 and also includes an S800 acceptance correction of +3%. The inclusive cross section is plotted run-by-run in figure 3.1 with only statistical fluctuations observed. The two normalization runs taken for this measurement give  $^{28}\text{Ne}$  beam rates that differ by approximately 3%. This apparent fluctuation in the beam rate is the dominant source of uncertainty in the measured cross section.

#### 3.1.2 Gamma-Ray Analysis

The Doppler-reconstructed  $\gamma$ -ray spectrum in coincidence with the  $^{25}\text{Ne}$  recoils is shown in figure 3.2. A doublet is observed at approximately 1.7 MeV as well as a small peak at 2.09 MeV. The  $^{25}\text{Ne}$  level structure has been studied in two recent  $\beta$ -decay measurements [36, 52]. The doublet at 1.7 MeV is consistent with the known 1.6-MeV  $\rightarrow$  1.7-MeV  $\rightarrow$  GS cascade. Low statistics and resolution lead to a 15-20 keV



### Data Collection Run

Figure 3.1: Run-by-run plot of  $\sigma_{inc}$  for single-neutron knockout from  $^{26}\text{Ne}$ . The average value is 95(3) mb before acceptance corrections, and only statistical fluctuations are observed.

$E_{level}$ (MeV)	$E_{\gamma}$ (MeV)	I (%)	b (%)	$\sigma$ (mb)
0.000	—	—	47.8(37)	45.4(35)
1.703	1.703	45.4(32)	28.1(20)	26.7(19)
3.316	1.613	18.6(27)	19.5(29)	18.5(28)
2.090	2.090	6.8(19)	7.2(20)	6.8(19)
$\sigma_{inc} = 97.5(53) \text{ mb}$				

Table 3.1: Results for  $^{26}\text{Ne}$ .

uncertainty in the energy of the observed 1.6 MeV transition. Therefore, population of the known 3.324 and 3.135 MeV excited states cannot be decoupled.

The  $\gamma$ -ray spectrum is fit with response functions generated in a GEANT3 simulation for the three observed transitions. The fit also includes a continuum  $\gamma$ -ray distribution. The scale of the continuum is allowed to vary in the fit. However, the shape of the continuum, which is modeled with a double exponential function, is fixed using data from the  $^9\text{Be}(^{33}\text{Cl}, ^{32}\text{Cl})\text{X}$  measurement of Ref. [53] taken with the same setup and in which no  $\gamma$ -ray is observed above 466 keV. The results of the fit are shown in table 3.1.

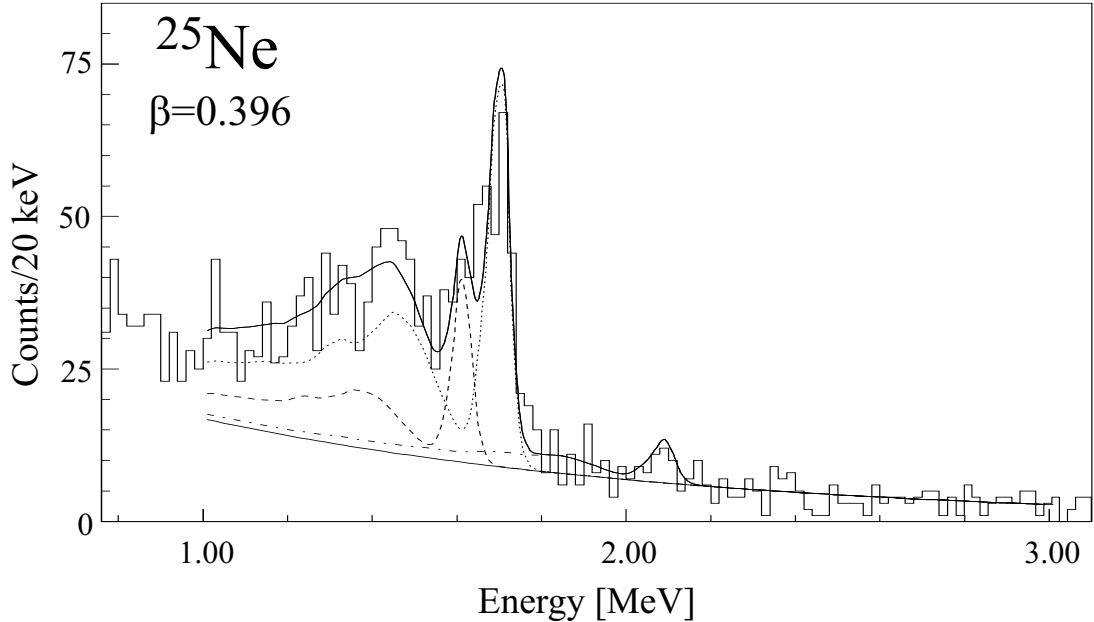


Figure 3.2: Doppler-reconstructed  $\gamma$ -ray energy spectrum for  ${}^9\text{Be}({}^{26}\text{Ne}, {}^{25}\text{Ne})\text{X}$ .

### 3.1.3 Longitudinal Momentum Distributions

The longitudinal momentum distribution is extracted for events in which the 1.7-MeV doublet is populated by gating on observed  $\gamma$ -rays in this region. The contribution from the underlying  $\gamma$ -ray continuum is subtracted to yield the distribution shown in the right panel of figure 3.3. This distribution includes contributions from both the 1.7 and 3.3 MeV levels. The plot is overlaid with theoretical distributions assuming  $\ell=0$  and  $\ell=2$ . The excited state distribution is in good agreement with an assignment of  $\ell=2$ . With the extracted momentum distribution acceptance losses in the spectrograph are estimated to be 5(3)% for events in which these levels are populated. Although it is not possible to extract a momentum distribution for the 2.09-MeV transition, the most recent  $\beta$ -decay study of  ${}^{25}\text{Ne}$  as well as a recent  $d({}^{24}\text{Ne}, {}^{25}\text{Ne})p$  measurement indicate a spin parity assignment of  $3/2^+$  for this levels, corresponding to an  $\ell=2$  momentum distribution for these events. Therefore, the same correction of 5(3)% is assumed.

To extract the longitudinal momentum distribution for events in which the ground state is populated, the excited state distribution, normalized to unity, is scaled by the

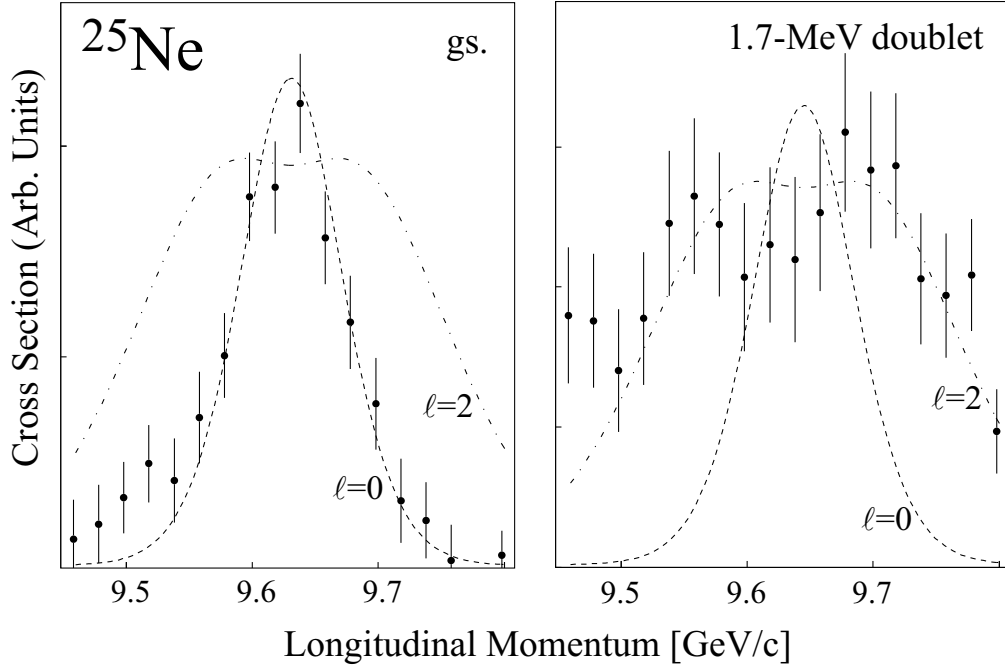


Figure 3.3: Longitudinal momentum distributions for  $^{25}\text{Ne}$ .

summed branching ratio to all excited states and subtracted from the inclusive distribution, also normalized to unity. The resulting distribution is shown in the left panel of figure 3.3 with calculations superimposed. This distribution is in good agreement with an  $l=0$  assignment allowing for the unambiguous spin-parity assignment of  $1/2^+$  for the ground state of  $^{25}\text{Ne}$ . With the narrow width of this distribution, acceptance corrections are negligible.

## 3.2 Single-Neutron Removal Data from $^{28}\text{Ne}$

### 3.2.1 Inclusive Cross Section

For the  $^9\text{Be}(^{28}\text{Ne}, ^{27}\text{Ne})\text{X}$  reaction, the inclusive cross section is measured to be  $66(3)$  mb. This cross section does not include a full correction for acceptance losses as discussed below. The  $^{27}\text{Ne}$  fragment rate is plotted run-by-run with only statistical fluctuations observed. The  $^{28}\text{Ne}$  beam rate, measured several times over the course of the measurement, shows no apparent systematic deviations. The PID efficiency is

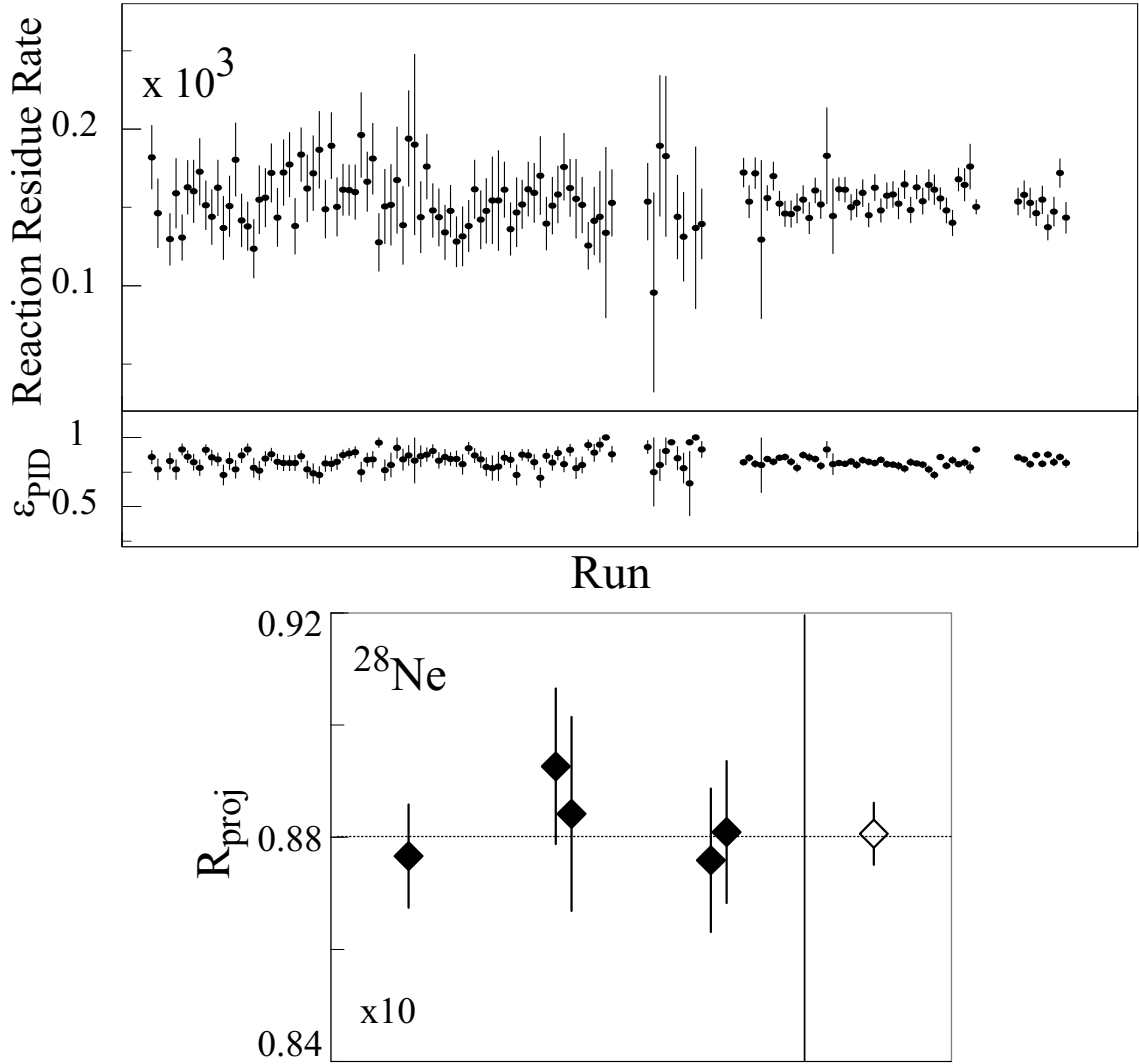


Figure 3.4: Beam and fragment rates for  ${}^9\text{Be}({}^{28}\text{Ne}, {}^{27}\text{Ne})X \sigma_{inc}$  measurement. No systematic deviations are observed in the fragment rate or the beam rate. The weighted average of the beam rate is plotted as an open data point in the lower panel.

also plotted run-by-run in figure 3.4 and averages to approximately 84%.

### 3.2.2 Gamma-Ray Analysis

The  $\gamma$ -ray spectrum coincident with  ${}^{27}\text{Ne}$  reaction residues is shown in figure 3.5. Three de-excitation  $\gamma$ -rays with energies of 0.119 MeV, 0.765 MeV, and 0.885 MeV were identified in coincidence with the reaction residues. Given that the energies of the lower two photo-peaks sum the that of the higher,  $\gamma - \gamma$  coincidences are

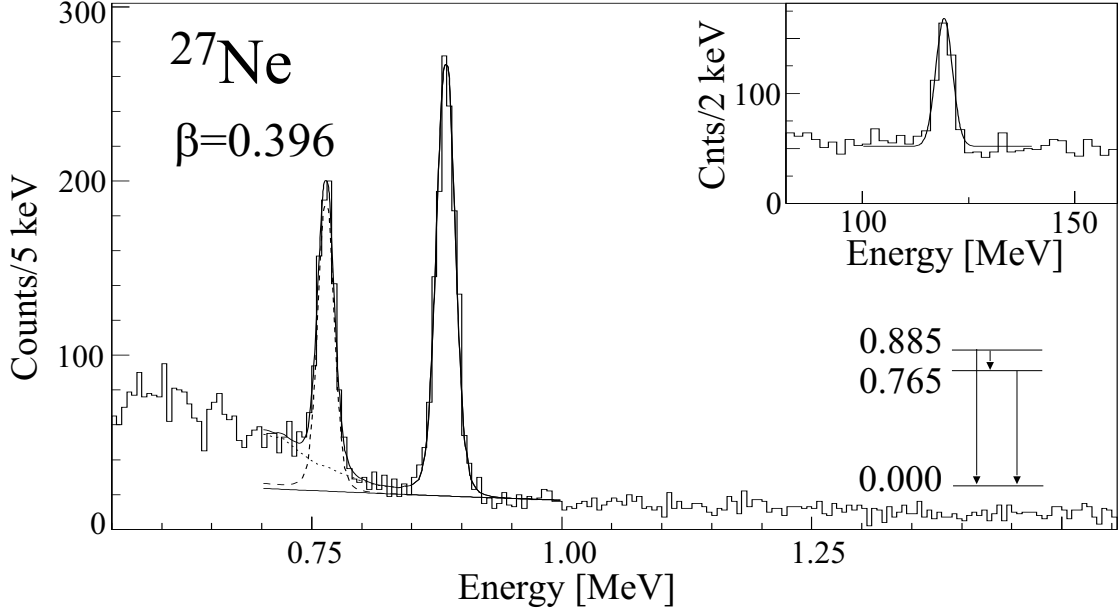


Figure 3.5: Gamma-ray energy spectrum in coincidence with  $^{27}\text{Ne}$ .

analyzed to search for a possible cascade. Since SeGA is not Compton-suppressed, at energies around 0.1 MeV,  $\gamma - \gamma$  coincidence spectra may show structures arising from Compton scattering between detectors. To suppress these structures, a simple add-back procedure is used for analysis of the  $\gamma - \gamma$  coincidences alone. Coincident  $\gamma$ -rays observed less than 16 cm apart are summed. The separation of 16 cm is chosen on the basis of a clear excess of counts below this value in a plot of separation distances of all observed  $\gamma - \gamma$  coincidence for  $^{27}\text{Ne}$ . This analysis, summarized in figure 3.6, reveals that the three  $\gamma$ -ray transitions originate from only two states as is indicated in the proposed level scheme shown in the inset of figure 3.5.

Gamma-ray intensities are determined in a statistical fit to the spectrum with results summarized in table 3.2. For the two higher-energy photo-peaks, response functions are generated in a GEANT3 simulation and are included in the fit along with an exponential continuum with freely varying slope and scale. Determination of the intensity of the 0.119-MeV transition is complicated by SeGA's low energy threshold of approximately 0.1 MeV for this measurement and uncertainty in the accuracy of the simulation at  $\gamma$ -ray energies around 0.1 MeV. Due to the Doppler

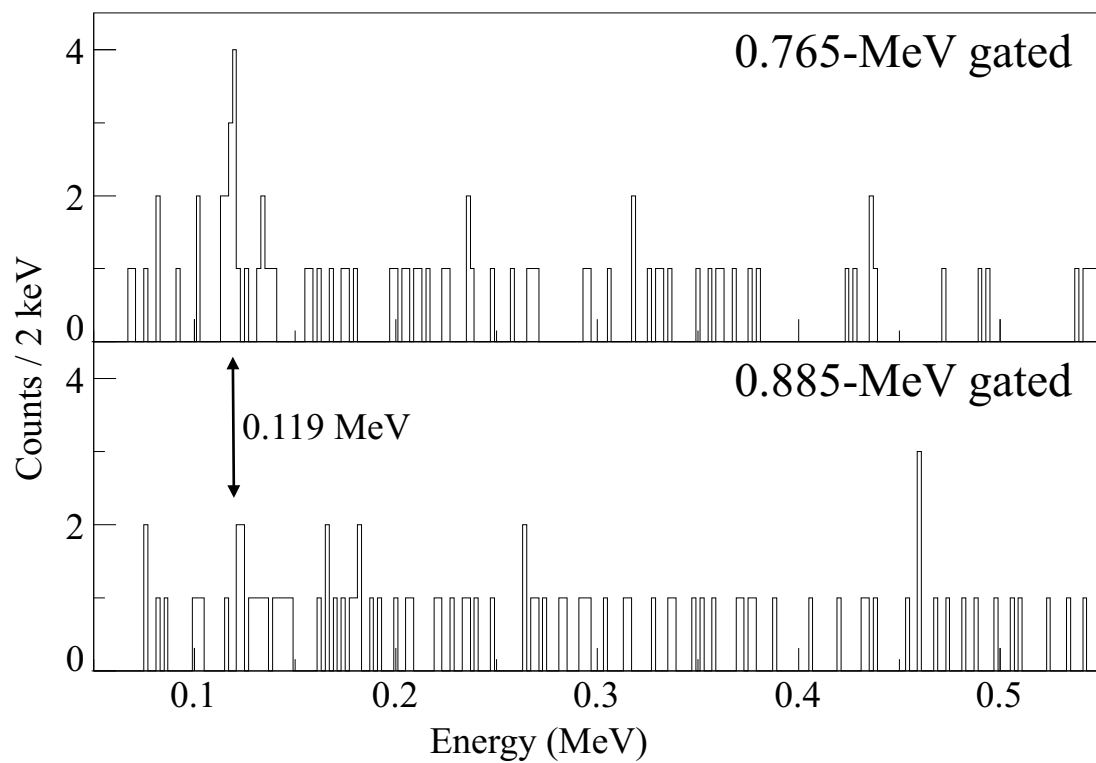


Figure 3.6: Projections from  $^{27}\text{Ne}$   $\gamma - \gamma$  matrix. Projected slices are plotted for  $E_\gamma=0.765$  MeV and  $E_\gamma=0.885$ . Coincidence between the 0.119- and 0.765-MeV transitions is observed while no coincidence is observed between the 0.119- and 0.885-MeV transitions.

$E_{level}$ (MeV)	$E_{\gamma}$ (MeV)	I (%)	b (%)	$\sigma$ (mb)
0.000	—	—	31.3(39)	20.6(28)
0.765	0.765	24.1(16)	15.6(17)	10.3(12)
0.885	0.885	44.6(26)	53.1(32)	35.0(27)
	0.119	8.5(10)		
$\sigma_{inc} = 65.9(33) mb$				

Table 3.2: Results of  $\gamma$ -ray analysis for  $^{28}\text{Ne}$ . Branching ratios  $b$  are deduced by intensity balancing of the listed  $\gamma$ -ray intensities  $I$ . Partial cross sections  $\sigma$  are also included, given as the product of the inclusive cross section and the branching ratios.

boost, the 0.119-MeV photo-peak is only clearly detected in the four forward-most angle pairs at  $24^\circ$ ,  $29^\circ$ ,  $40^\circ$ , and  $60^\circ$ . The 0.119-MeV photo-peak observed in the summed spectrum for these eight detectors was fit with a Gaussian peak shape and a second order polynomial background. The peak area is corrected by the measured photo-peak efficiency for the set of eight detectors.

Intensities of 8.5(10)%, 24.1(16)%, and 44.6(2.6)% relative to the inclusive sum of single-neutron knockout events are determined for the respective 0.119, 0.765, and 0.885 MeV transitions. Intensity balancing is used to determine the ordering of the 0.119 and 0.765 MeV transitions. Branching ratios for the population of the 0.765 and 0.885 MeV states are 15.6(17)% and 53.1(31)%, respectively. The strength of the 0.119 MeV transition is 19.3(25)% relative to the 0.885 MeV intensity.

At fragmentation velocities, the Doppler reconstruction becomes rather sensitive to the lifetime of the emitting state. Reconstruction is performed assuming the  $\gamma$ -ray is emitted from the center of the target. For lifetimes on the order of 10 ps or greater, this assumption leads to a low-energy skew in the reconstructed photo-peak as more and more particle emit  $\gamma$ -rays further downstream. Analysis of the 0.885 MeV photo-peak indicates no observable lifetime with an upper limit of 10 ps for the half-life. With the measured  $\gamma$ -ray branching ratio for the 0.885-MeV state, the half-life for the 0.119 and 0.885 MeV transitions are less than 70 and 12 ps, respectively. These half-life limits are translated into upper limits on reduced transition probabilities, and

comparison with recommended upper limits [54] gives a restriction in multipolarity of E1 or M1 for the 0.119-MeV transition and E1, M1, or E2 for the 0.885-MeV transition.

### 3.2.3 Longitudinal Momentum Distributions

Longitudinal momentum distributions are extracted for events populating the 0.765-MeV and 0.885-MeV photo-peaks. Small contributions from the underlying continuum distribution are subtracted, and the resulting distributions are shown in figure 3.7. Despite the use of focused-mode optics, the momentum resolution for this data is 40 MeV/c FWHM. This is achieved by tracking the momentum of the secondary beam on an event-by-event basis in the S800 analysis line. Theoretical distributions are calculated for knockout to these two states assuming a number of  $\ell$ -value assignments. The narrow distributions clearly indicate an assignment of  $\ell = 0, 1$ , but the relatively large error bars and the similarity between  $\ell=0$  and  $\ell=1$  distributions do not allow for a more definitive assignment.

The ground state momentum distribution is extracted by subtraction of the excited state distribution from the inclusive and is shown in figure 3.7. The gates on the 0.765 and 0.885 MeV photo-peaks were summed to improve statistics in the excited state distribution. With a relatively small branch to the ground state, this subtraction leads to large uncertainties in the ground state distribution. The relatively large uncertainty in the extracted distribution does not allow for a definitive  $\ell$ -value assignment.

The low-momentum tails [55], which are not yet understood, do not allow for an accurate extrapolation of losses outside the acceptance. These corrections, based on extrapolation, affect the measured partial cross sections from the  ${}^9\text{Be}({}^{28}\text{Ne}, {}^{27}\text{Ne})\text{X}$  reaction and are estimated to be approximately 5-10% for excited-state and 15-25% for ground-state events. These estimated corrections are not applied to the reported cross sections.

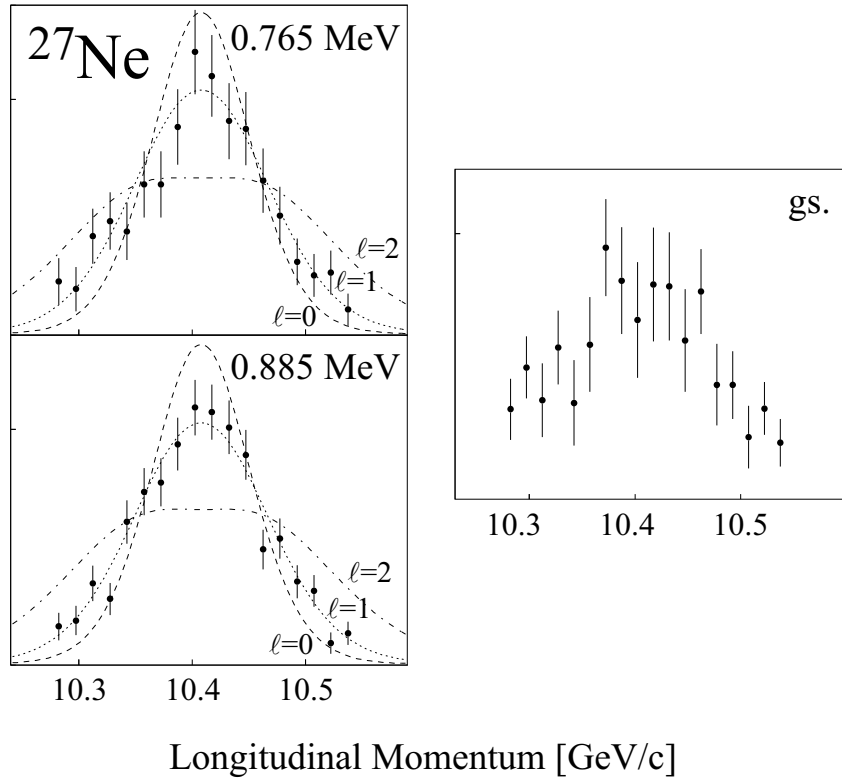


Figure 3.7: Momentum distributions for  $^{27}\text{Ne}$ . The right two panels show momentum distributions extracted for the 0.765- and 0.885-MeV photo-peaks while the left shows the extracted ground state distribution. Overlaid calculated distributions assuming  $\ell=0,1,2$  indicate  $\ell < 2$  for the excited states. The substantial uncertainty in the extracted ground state distribution does not allow for a quantitative analysis of the shape.

### 3.3 Single-Neutron Knockout from $^{30}\text{Mg}$

Particle identification for the  $^{29}\text{Mg}$  fragments was achieved as outlined in section 2.3.1 using a  $\Delta E$  vs TOF method. The inclusive cross section is extracted according to equations 2.2 and 2.3. The projectile and fragment rates are plotted on a run-by-run basis in figure 3.8 with no apparent systematic deviations. The PID efficiency is estimated to be 88% for the fragment rate and 100% for the projectile rate. The inclusive cross section is determined to be 100(5) mb, where the uncertainty is dominated by the variance in the target thickness reported by the manufacturer. Other sources of uncertainty stem from software cuts and the estimation of the PID efficiency. These are approximately 1% each and are negligible compared to the uncertainty in the target thickness.

#### 3.3.1 Gamma-Ray Analysis

The Doppler-reconstructed  $\gamma$ -ray spectrum in coincidence with  $^{29}\text{Mg}$  fragments is shown in figure 3.9. Eight photo-peaks are clearly observed in the spectrum with energies of approximately 0.3, 1.1, 1.6, 2.1, 2.2, 2.5, 2.6, 3.2 MeV. The peak at 0.3 MeV is found to be much broader than the expected 15 keV FWHM for a photo-peak at this energy. This suggests that the emitting state has a relatively long lifetime. Therefore, the low energy region of the spectrum is Doppler-reconstructed with the post-target fragment velocity as the majority of these  $\gamma$ -rays are emitted after the fragment has left the target. The angle for the Doppler-reconstruction is still calculated using emission from the center of the target giving rise to the low-energy tail.

The level structure of  $^{29}\text{Mg}$  has been previously studied by  $\beta$ -decay and by  $\beta$ -delayed neutron emission using high-resolution germanium photon detectors [56, 57]. The transition  $\gamma$ -rays observed in this previous work are used as a basis for the analysis of the present data. The spectrum is analyzed in two segments: the broad

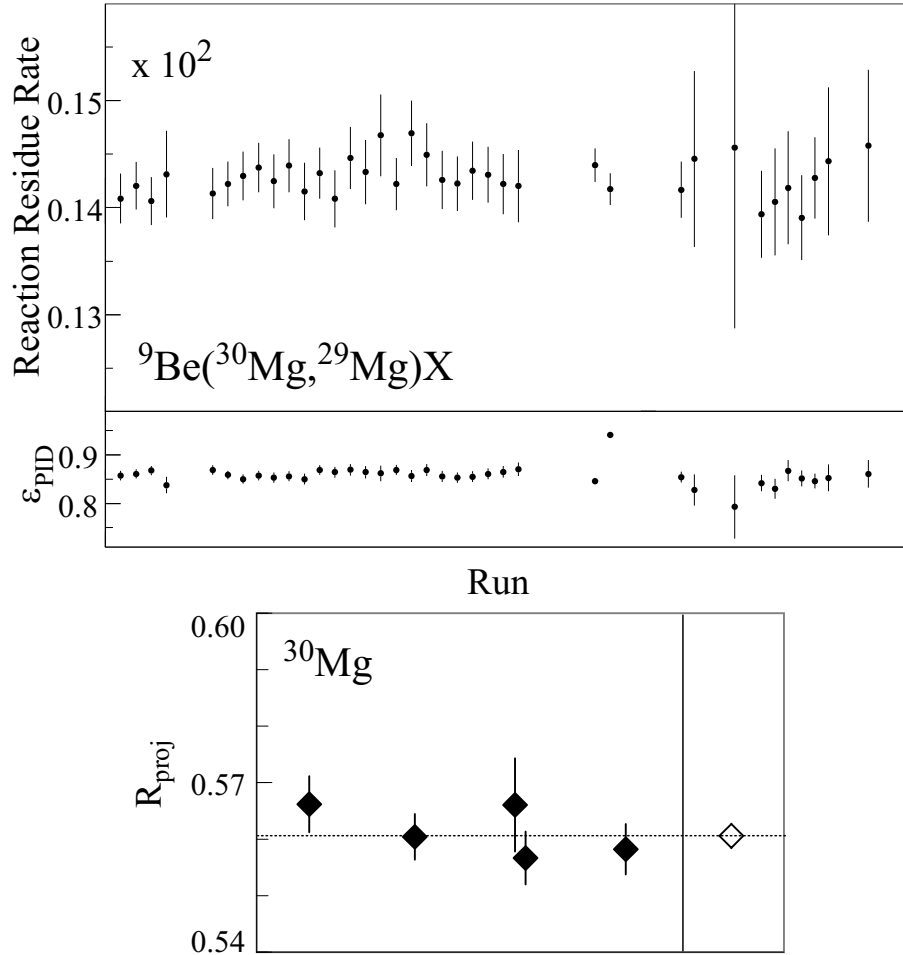


Figure 3.8: Fragment and beam rates for the single-neutron removal from  $^{30}\text{Mg}$ . The upper panel shows the reaction residue, or fragment, rate normalized on the S800 object scintillator. The PID efficiency for the fragment runs is also shown in the upper panel. The lower panel shows the projectile rate measurements. The open data point represents the average rate over all measurements while the closed points represent individual measurements taken at intervals of several hours with the exception of the closely spaced points which were collected in subsequent data runs with nearly no time elapsed between them.

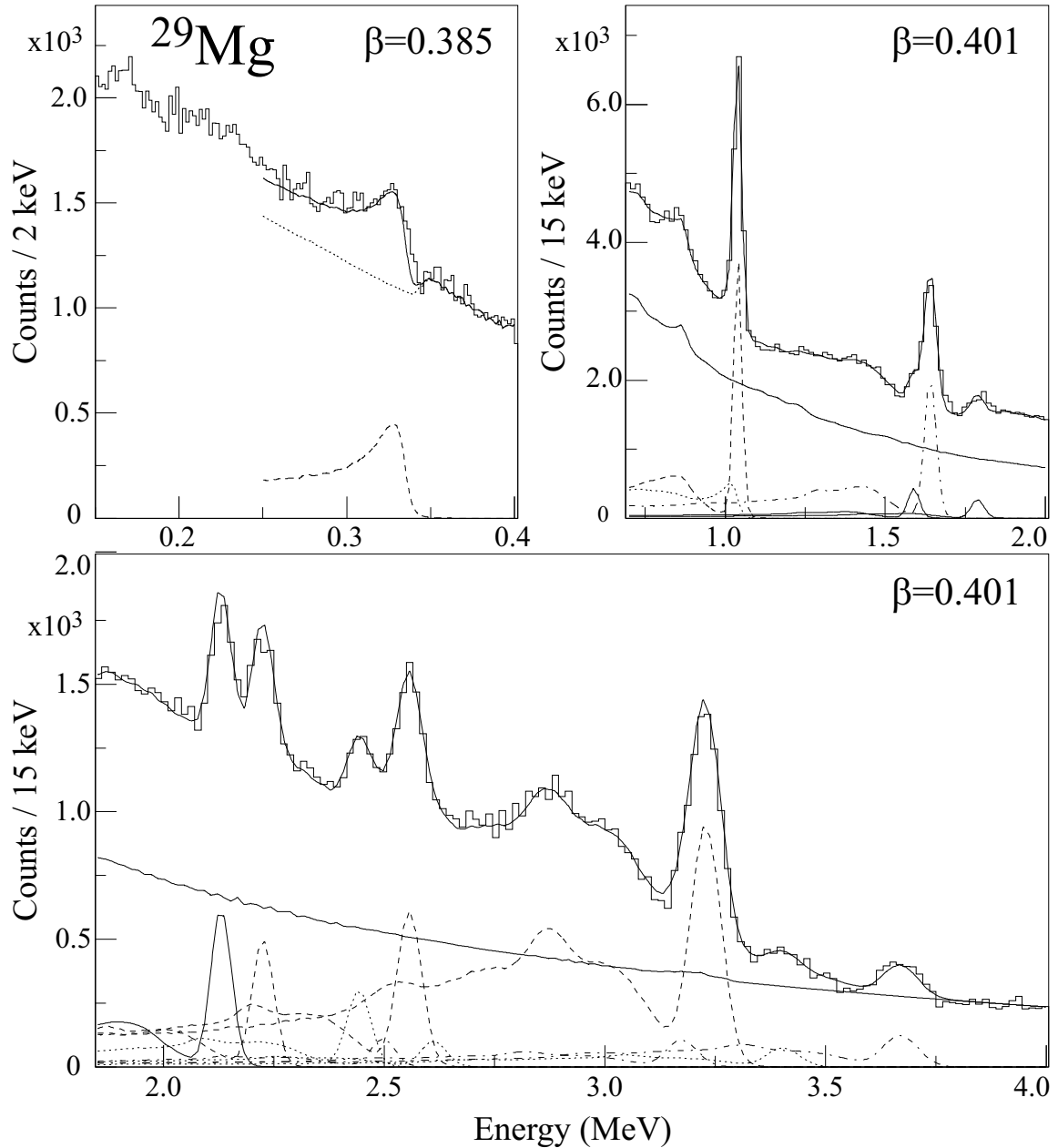


Figure 3.9: Gamma-ray energy spectrum coincident with  $^{29}\text{Mg}$ . The upper left panel shows the low-energy region of the spectrum which is Doppler-reconstructed assuming a post-target fragment velocity while the remainder of the analyzed spectrum, shown in the upper right and lower panel, are Doppler-reconstructed assuming a mid-target fragment velocity. The spectrum is overlaid with the result of a statistical fit which includes a continuum  $\gamma$ -ray distribution as well as simulated response functions for fifteen photo-peaks, each of which is also included in the figure.

region between 0.7 and 4.0 MeV which is Doppler-reconstructed assuming a mid-target velocity and the low-energy region between 0.25 and 0.4 MeV which is Doppler-reconstructed assuming a post-target velocity.

Gamma-ray intensities in the region between 0.7 MeV and 4.0 MeV are taken from a statistical fit to the spectrum which includes simulated response functions for each transition  $\gamma$ -ray and a continuum  $\gamma$ -ray distribution. The shape of the continuum is fixed for energies above 1 MeV using the  $\gamma$ -ray spectra from the  ${}^9\text{Be}({}^{28}\text{Ne}, {}^{27}\text{Ne})\text{X}$  data and from the  ${}^9\text{Be}({}^{31}\text{Mg}, {}^{31}\text{Mg})\text{X}$  data. No coincident transition  $\gamma$ -rays are observed above 1 MeV and 2.5 MeV, respectively, for these reactions. As the background observed for with the  ${}^{27}\text{Ne}$  and  ${}^{31}\text{Mg}$  fragments does not extrapolate well below 1 MeV, a free varying exponential is also included in the fit, which gives a negligible contribution to the fit above 1 MeV after  $\chi^2$  minimization.

The fit is achieved by first including seven known peaks within this region of the spectrum: 1.04, 1.64, 2.13, 2.21, 2.45, 2.56, and 3.23 MeV. A  $\chi^2$  minimization is performed, and additional known peaks are added where they would clearly improve the fit. This process leads to the inclusion of an additional five known transitions. Additionally, the 1.64 MeV transition and three transitions from the doublet at 3.23 MeV (the 2.133 transition needs no shift) are shifted by +5(1) keV while the known 2.211 MeV transition is shifted by +17(3) keV to match the observed spectrum. Finally, two previously-unobserved transitions are added at 1.79 and 3.41 MeV. While the statistics are limited for these low-intensity photo-peaks, both seem to appear in Doppler-reconstructed spectra from the forward ( $24^\circ$ ,  $29^\circ$ ,  $40^\circ$ ), middle ( $60^\circ$ ,  $78^\circ$ ,  $90^\circ$ ), and backward ( $126^\circ$ ,  $139^\circ$ ,  $147^\circ$ ) groups of angle-pairs, suggesting that these  $\gamma$ -rays are emitted from a source moving at approximately beam velocity. The placement of these transitions within the level scheme cannot be determined as the limited statistics do not allow for analysis of the  $\gamma$ -ray coincidences. The 3.41 MeV transition is assumed to feed the ground state doublet given its proximity to the neutron separation energy at 3.672(14) MeV [58]. The 1.79 MeV transition may link one or both of the states in

the 3.23 MeV doublet to the state at 1.431 MeV. This placement is not assumed in the intensity balance. Intensities, branching ratios, and deduced partial cross sections derived from this analysis are listed in table 3.3 and illustrated in figure 3.10.

The 5 and 17 keV shifts included in the fit to the  $\gamma$ -ray energy spectrum represent significant deviations from previously observed transitions in  $^{29}\text{Mg}$ , for which estimated uncertainties in energy are 1 keV or less. Possible sources of uncertainty in the energy of the transition from the present measurement include systematic errors arising from the Doppler-reconstruction parameters as well as shifts in the photo-peak due to the lifetime of the emitting state. Systematic errors due to uncertainty in the Doppler-reconstruction parameters are excluded due to the good agreement of the 1.04 MeV, 2.13 MeV, and 2.56 MeV transitions with previous measurements. Further, systematic deviations due to errors in the Doppler-reconstruction scale with energy, whereas in the present data an identical +5 keV deviation is found at 1.6 and 3.2 MeV. Lifetime effects are also excluded since they lead to a reduction in the centroid energy of the photo-peak while an increase is observed.

The 5 keV shift is found for the 1.64 MeV and 3.23 MeV photo-peaks, both of which are just below excess  $\gamma$ -ray strength in the energy spectrum not observed in previous  $\beta$ -decay measurements. These 5 keV shift may be artificial, resulting from additional  $\gamma$ -ray excesses at the edge observed photo-peaks. The 17 keV shift is more dramatic and may represent population of a previously unobserved state.

Moving to the low-energy region of the spectrum, to accurately determine the intensity of the 0.336 MeV photo-peak, the half-life of the state must first be determined. The half-life is extracted by analysis of the shape of the photo-peak. Given the rather high level of background under the photo-peak, to accurately extract the half-life, the shape of the background must also be known. At energies around 0.3 MeV, the background is dominated by  $\gamma$ -rays that are back-scattered from surrounding lab equipment. Since the shape of the back-scattering  $\gamma$ -ray spectrum is not strongly dependent of the energies of the back-scattered  $\gamma$ -rays it can be taken from the spec-

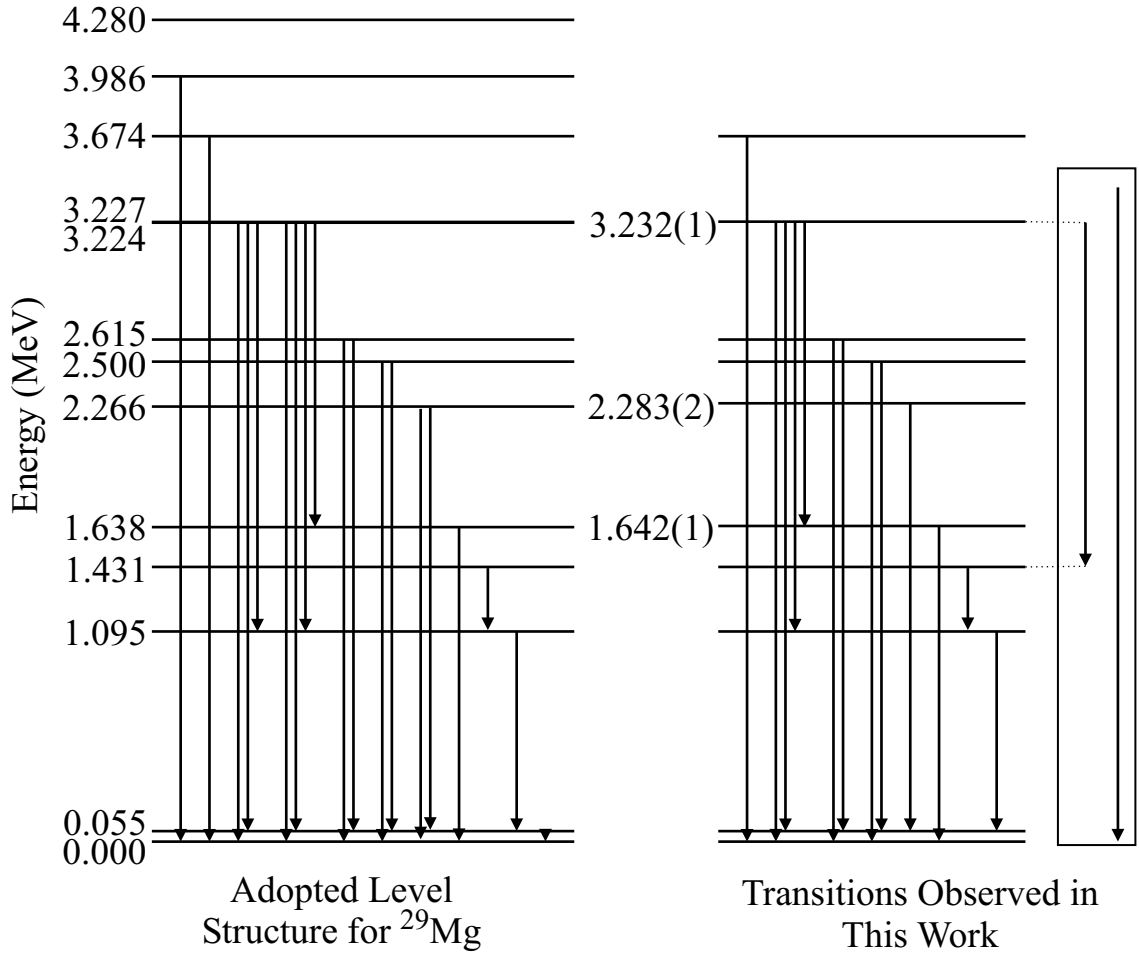


Figure 3.10: Comparison of observed  $\gamma$ -ray transitions to the adopted level scheme of  $^{29}\text{Mg}$ . The adopted scheme and transitions are shown on the left while interpretation of transitions observed in the present work are shown on the right. Energies from the present work are only given where they disagree with adopted values. Two unplaced transitions are shown to the right of the observed level scheme. The 1.79-MeV transition is assumed to connect the 3.23-MeV doublet and the 1.43-MeV state while the 3.41-MeV transition is assumed to feed either the ground state or the 0.055-MeV state since feeding to the next highest excited state would place the originating state 0.7 MeV above the neutron separation energy.

$E_{level}$ (MeV)	$E_{\gamma}$ (MeV)	I (%)	b (%)	$\sigma$ (mb)
0.000				
0.055			49.2(35)	49.2(43)
1.095	1.040	8.5(11)	4.3(15)	4.3(15)
1.431	0.336	$7.2^{+0.1}_{-1.4}$	$5.8^{+1.0}_{-1.8}$	$5.8^{+1.1}_{-1.8}$
1.642	1.642	9.0(11)	7.3(15)	7.3(16)
2.283	2.228	3.7(10)	3.7(10)	3.7(10)
2.500	2.445	2.7(10)	3.7(10)	3.7(14)
	2.500	1.0(10)		
2.615	2.560	5.9(11)	6.9(15)	6.9(15)
	2.615	1.0(10)		
3.232	1.586	1.8(10)	22.9(24)	22.9(24)
	1.79(?)	1.4(10)		
	2.133	4.3(10)		
	3.178	1.5(11)		
	3.232	13.9(13)		
3.674	3.674	2.3(10)	2.3(10)	2.3(10)
???	3.41	1.2(10)	1.2(10)	

Table 3.3: Gamma-ray intensities and branching ratios for  $^{29}\text{Mg}$ .

tra in coincidence with other fragments measured with the same setup. Figure 3.11 shows the low energy  $\gamma$ -ray spectrum from the forward three angles in coincidence with  $^{28}\text{Mg}$  and  $^{24}\text{Ne}$ , which are observed simultaneously with  $^{29}\text{Mg}$  and result from other unspecified reaction channels. A plot of the ratio of these spectra, shown in the inset of figure 3.11, clearly demonstrates the nearly identical shape. This shape is modeled by an quadratic exponential function of the form  $f(x) = a * \exp(-bx + cx^2)$  from 0.175 to 0.400 MeV.

Simulations of the effect of long life-times in Doppler-reconstructed spectra reveal that the forward most detectors ( $24^\circ$ ,  $29^\circ$ , and  $40^\circ$ ) are the most sensitive to the half-life. To determine the half-life of the 1.431-MeV state, response functions for the 0.336-MeV transition were generated for half-lives from zero picoseconds up to thirty nanoseconds. A fit to the forward-angle spectrum was performed for each of the response functions with three free parameters: the scale and position of the response function and the scale of the background. The  $\chi^2$  distribution is shown in figure 3.12

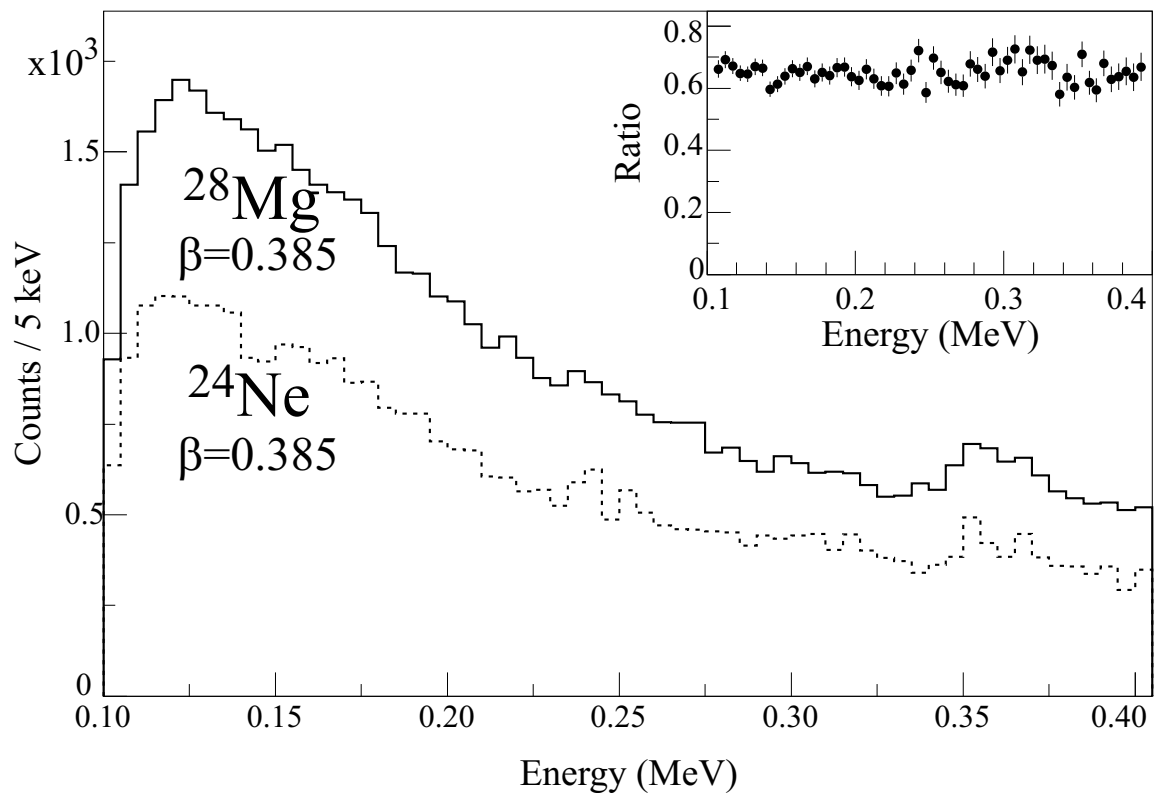


Figure 3.11: Low-energy  $\gamma$ -ray background from fragments collected with  $^{29}\text{Mg}$ . The low-energy  $\gamma$ -ray spectrum is shown in coincidence with  $^{28}\text{Mg}$  (solid) and  $^{24}\text{Ne}$  (dashed) fragments collected simultaneously with  $^{29}\text{Mg}$  fragments. As indicated by the ratio plotted in the inset, the shape of the low-energy spectra is identical for the fragments shown here due to the dominance of back-scattering in this energy range. The shape of the low energy back ground observed here is used in the fit to the low-energy region of the  $^{29}\text{Mg}$  spectrum between 0.2 and 0.375 MeV as that spectrum is also dominated by back-scattering in the indicated energy range.

around the minimum. A rather shallow minimum is found at 1.3 ns. The  $\chi_{min}^2 + 1$  region gives one-sigma uncertainties of +0.03 ns and -0.235 ns such that the half-life is determined to be  $1.30_{-0.24}^{+0.03}$  ns. The intensity of the 0.336 photo-peak is extracted by analysis of the spectrum collected in the entire array using the 1.3-ns response function. Results of this analysis are included in table 3.3 and figure 3.10.

### 3.3.2 Longitudinal Momentum Distributions

Longitudinal momentum distributions for a number of populated states are extracted by gating on the  $\gamma$ -ray spectrum. Distributions are only extracted for photo-peaks clearly visible in the spectrum, which include 0.336, 1.040, 1.638, 2.133, 2.211, 2.445, 2.560, 3.227, and 3.674 MeV. A cut is made encompassing all or part of the photo-peak of interest. However, this cut also includes  $\gamma$ -ray continuum events as well as contributions from the response of SeGA to other de-excitation  $\gamma$ -rays. For the 0.336- and 1.040-MeV photo-peaks, subtraction of these other components is achieved using a distribution gated slightly higher in  $\gamma$ -ray energy.

The background-subtracted 1.040-MeV distribution is shown in figure 3.13 overlaid with calculated distributions assuming  $\ell=0$  and  $\ell=1$ . Both calculated distributions include a 50% by area  $\ell=2$  contribution added to account for the observed indirect feeding of the 1.095-MeV state from the 3.227-MeV doublet. Assignment of  $\ell=2$  for this doublet is discussed below. The background-subtracted 0.336-MeV distribution is also shown in figure 3.13. This raw distribution is taken from a gate which has a 1:5 peak-to-total ratio, resulting in rather large error bars for the subtracted distribution. Calculated distributions assuming  $\ell=3$  and  $\ell=2$  are overlaid with the former showing better agreement. However, due to large error bars and uncertainty in the size and shape of the low momentum tail,  $\ell=2$  cannot be ruled out.

For the rest of the listed photo-peaks, close proximity to other peaks in the spectrum make the above mentioned subtraction procedure unreliable. Therefore, distributions are extracted using a slightly more complicated procedure. The photo-peak

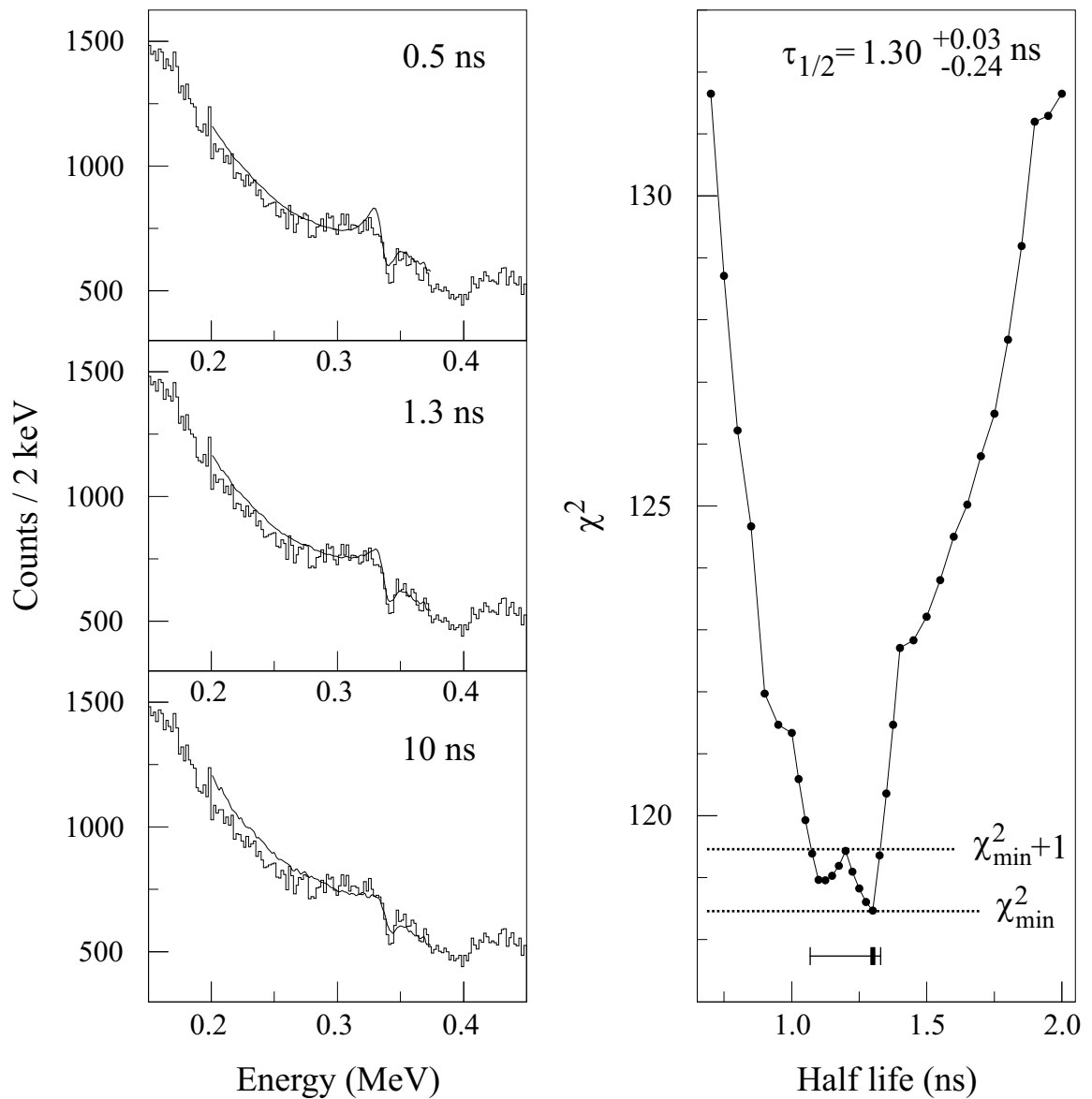


Figure 3.12: Half-life measurement of 1.431-MeV states in  $^{29}\text{Mg}$ . The left panels show fits to the 0.336-MeV photo-peak observed in the forward-angle low-energy  $\gamma$ -ray spectrum coincident with  $^{29}\text{Mg}$  fragments. The spectrum is fit with simulated response functions assuming half-lives of 0.5, 1.3, and 10.0 ns. The spectrum is fit many times assuming a number of half-lives. The right panel shows the  $\chi^2$  distribution around the minimum which indicates a half-life of  $1.30^{+0.03}_{-0.24}$  ns.

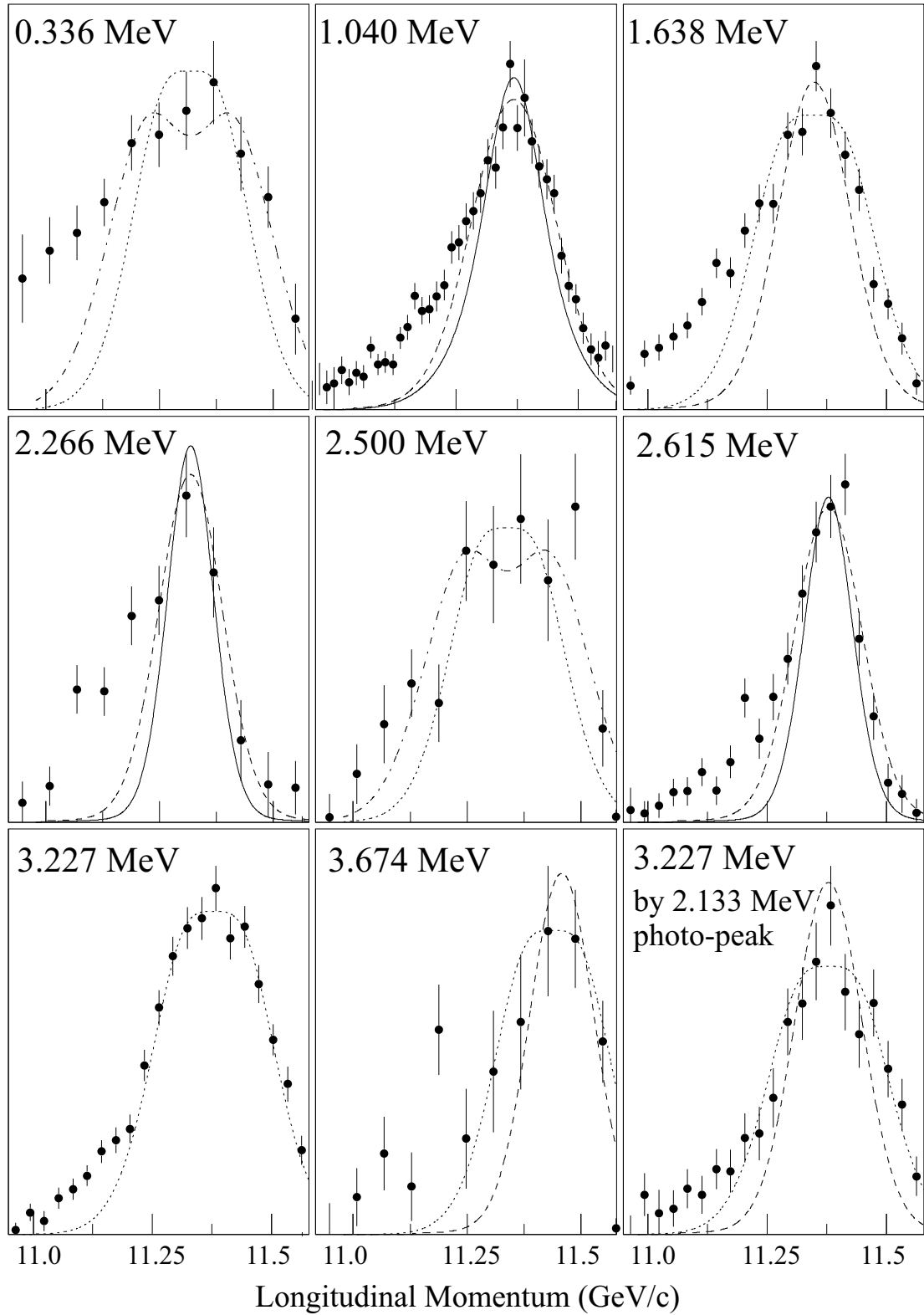


Figure 3.13: Momentum distributions for  $^{29}\text{Mg}$ . Distributions are extracted as described in the text. Each plot is overlaid with calculated distributions assuming  $\ell=0$  (solid),  $\ell=1$  (dashed),  $\ell=2$  (dotted), and  $\ell=3$  (dot-dashed).

and Compton-continuum of the simulated response functions used to fit the  $\gamma$ -ray spectrum agree within 10% with calibration data for energies as low as 0.5 MeV, where back-scattering begins to play a larger role. Therefore, the contribution from each photo-peak for any given slice on the energy axis within the fit range ( $>0.5$  MeV) can be estimated with good accuracy. Eight raw distributions, denoted  $R_i(p_{//})$ , are extracted: the last seven in the list above as well as a continuum distribution gated on  $\gamma$ -rays observed above 4.0 MeV. The fractional contribution to each gate from each populated state are shown in table 3.4. To extract the true distribution for each populated state, denoted  $S_i(p_{//})$ , the matrix equation  $\vec{R} = A \vec{S}$  is formed using data from table 3.4. This equation assumes that both the S and R distributions are normalized to unity. The system is over-constrained due to the fact that both the 2.133 and 3.227 MeV photo-peaks de-excite the same state. Therefore, the 2.133-MeV gate is not included in the matrix as the 3.227-MeV gate is much cleaner. The matrix equation is inverted to find the dependence of the true distributions on the raw. The 2.133-MeV true distribution is obtained by subtracting extracted true distributions from the 2.133-MeV raw distribution with coefficients taken from table 3.4.

As cuts are taken on photo-peaks in the  $\gamma$ -ray spectrum, the emitting state usually has a dominant effect on the extracted raw distribution. This is true of the 1.638 and 3.227 MeV cuts with 42% and 58% contributions, respectively, from the corresponding states. For the 2.133-MeV gate, the dominant 3.227-MeV contribution is only 35% of the total. However, the true 2.133-MeV distribution is in reasonable agreement with the true 3.227-MeV one, suggesting that, even at a peak-to-total ratio of 1:3, accurate distributions are extracted. The 2.266, 2.500, and 3.674 MeV true distributions are extracted from 1:5 peak-to-total raw distributions and are clearly of poorer quality.

All extracted distributions are shown in figure 3.13. The 3.227-MeV distribution, shown with an  $\ell=2$  calculation overlaid, clearly exhibits an  $\ell=2$  character. The 1.638-MeV distribution appears to match an  $\ell=1$  distribution. However,  $\ell=2$  is not excluded. The 2.615-MeV distribution is rather narrow, suggesting an  $\ell=1$  or  $\ell=0$  assignment.

Gate	1.638	2.266	2.500	2.615	3.227	3.674	Continuum	Sum
1.638	0.421	0.034	0.024	0.036	0.097	0.006	0.366	0.983
2.133	—	0.029	0.083	0.127	0.350	0.010	0.394	0.994
2.211	—	0.222	0.082	0.167	0.118	0.012	0.392	0.993
2.445	—	—	0.210	0.089	0.235	0.017	0.436	0.987
2.560	—	—	0.013	0.332	0.259	0.017	0.366	0.986
3.227	—	—	—	—	0.580	0.065	0.330	0.976
3.674	—	—	—	—	—	0.213	0.787	1.000
Continuum	—	—	—	—	—	—	1.000	1.000

Table 3.4: Contribution with  $\gamma$ -ray gates from states populated in  $^{29}\text{Mg}$ . The first column identifies gates taken on photo-peaks in the Doppler-reconstructed  $\gamma$ -ray energy spectrum. The statistical fit to the spectrum is used to estimate the fractional contribution within each gate from each populated state in  $^{29}\text{Mg}$ . The continuum column list contributions from the underlying  $\gamma$ -ray continuum while the continuum row is associated with a gate positioned above the neutron separation energy in the  $\gamma$ -ray energy spectrum. To reduce the size of the matrix used to extract momentum distributions, a few low-intensity photo-peaks were not included in this analysis. The last column shows the sum for each row. Deviations from one reveal the effect of truncated set of photo-peaks used in this analysis.

The 2.266-MeV distribution is narrow, suggesting an  $\ell=0$  or  $\ell=1$  assignment, while the 2.500-MeV distribution is broad suggesting  $\ell=3$  or possibly  $\ell=2$ , depending on the size and shape of the low-momentum tail. An  $\ell=2$  assignment is indicated for the 3.674-MeV distribution but is not definitive due to the poor quality of this distribution.

### 3.4 Single-Neutron Knockout from $^{32}\text{Mg}$

Particle identification for the  $^{31}\text{Mg}$  fragments was achieved as outlined in section 2.3.1 using a  $\Delta E$  vs TOF method. Due to a rather poor TOF resolution an additional gate on TOF versus focal plane dispersive position was used for particle identification. To estimate possible losses in the mass selection cut, which in this case includes gates on TOF versus angle and TOF vs position, a charge-gated TOF spectrum, corrected for angle and position dependence, is generated. This spectrum includes peaks for  $^{30,31,32}\text{Mg}$  with intensities that should give a good estimate of the total number of each detected in the focal plane. The number of  $^{31}\text{Mg}$  fragments extracted in

this way is 10% larger than the number of  $^{31}\text{Mg}$  PID-gated events. This deviation may be the result of true  $^{31}\text{Mg}$  fragments which are not included in the PID gating conditions, scattered beam particles in the spectrograph that erroneously fall in the  $^{31}\text{Mg}$  corrected-TOF peak, or a combination of both. The  $^{32}\text{Mg}$  single-neutron knockout cross section is extracted using the number of fragments obtained from the PID gate. However, a systematic uncertainty of 7% is added to account for possible  $^{31}\text{Mg}$  fragments not included in the PID.

The inclusive cross section is extracted according to equations 2.2 and 2.3. The projectile and fragment rates are plotted on a run-by-run basis in figure 3.14. The fragment rate shows no sign of systematic deviation. However, the projectile rate measurements do not agree within one standard deviation. There are not enough data points to perform a true statistical analysis, but a 2% uncertainty is added to the projectile rate measurement to account for a possible systematic deviation. The PID efficiency is estimated to be 90% for the fragment rate and 100% for the projectile rate. The inclusive cross section is determined to be 94.0(83) mb, where the uncertainty is dominated by the variance in the target thickness reported by the manufacturer and the 7% uncertainty in the particle identification.

### 3.4.1 Gamma-Ray Analysis

The Doppler-reconstructed  $\gamma$ -ray spectrum coincident with  $^{31}\text{Mg}$  fragments is shown in figure 3.15. Two strong photo-peaks are observed at 0.17 and 0.22 MeV with several more at higher energies. The two low-energy photo-peaks are clearly skewed on the low-energy side due to the long lifetime of the 0.221-MeV state from which they are emitted. The half-lives of the 0.221-MeV and the 0.461-MeV state in  $^{31}\text{Mg}$  have been recently measured to be 133(8) ps and 10.5(8) ns, respectively [59]. Durations of 133ps and 10.5 ns correspond to respective distances of 1.5 cm and 1.2 m for particles moving at approximately a third of the speed of light. Therefore, the low energy region of the spectrum is Doppler reconstructed using the post-target beam

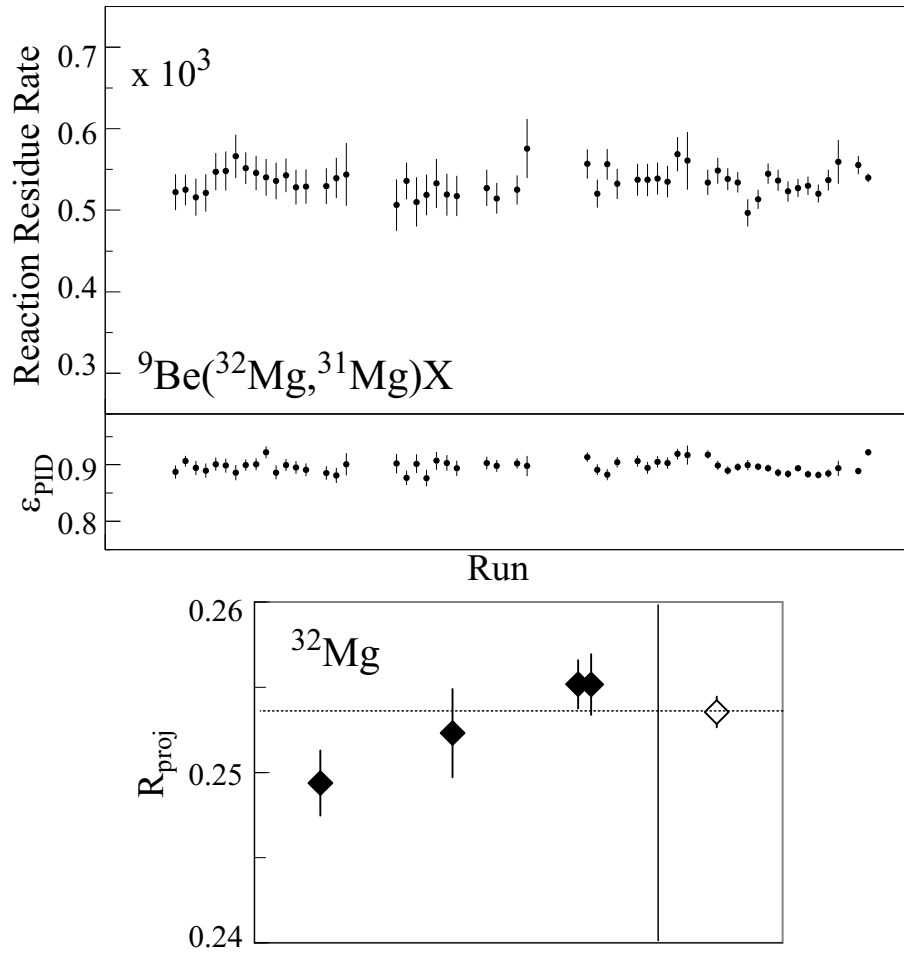


Figure 3.14: Fragment and beam rates for  ${}^9\text{Be}({}^{32}\text{Mg}, {}^{31}\text{Mg})\text{X}$ . Fragment and beam rates normalized on the secondary beam rate observed at the S800 object scintillator are plotted run-by-run. The plot of the fragment rate also includes the estimated PID efficiency plotted run-by-run.

velocity of 0.365c, calculated from the mean fragment momentum, measured with the spectrograph, and is analyzed using simulated response functions which include the known lifetimes. With this reconstruction, a small shoulder is observed in the spectrum on the high-energy side of the 0.221-MeV photo-peak. This shoulder is consistent with the response of SeGA to a 0.240-MeV  $\gamma$ -ray emitted from a state with a half-life of 10.5 ns. Therefore, this response function is also included in the analysis of the low-energy part of the spectrum. The remainder of the spectrum is Doppler reconstructed using a mid-target velocity of 0.380c determined using the procedure discussed in section 2.3.2.

The intensity of the 0.171-MeV photo-peak is obtained from a fit to the spectrum ranging from 0.125 to 0.195 MeV. The fit includes a simulated response function assuming a 133 ps half-life as well as a second order polynomial background. The 0.221 and 0.240-MeV photo-peak intensities are obtained in a fit ranging from 0.178 to 0.400 MeV. This fit includes simulated response functions and a background modeled by the sum of two exponentials. Intensities are reported in table 3.5 which include corrections of +3% and +6% for the 0.221-MeV and 0.171-MeV intensities, respectively, due to deviation of the simulated photo-peak efficiency from the measured efficiency at 0.122 MeV. Results are also summarized in figure 3.16.

The remainder of the spectrum is analyzed in two segments. The region from 0.4 MeV to 1.5 MeV is analyzed at a resolution of 5 keV/bin while the region from 1.8 MeV to 3.0 MeV is analyzed at 10 keV/bin. Intensities are obtained from a fit to the spectrum which includes a background and simulated response function. For the 5 keV/bin region, the background is modeled with a single exponential function with two free parameters. The background in the 10 keV/bin region is also modeled with an exponential function. However, the shape is fixed using data from the  $^{28}\text{Ne}$  single-neutron knockout measurement. The 5 keV/bin region includes photo-peaks at 0.452, 0.623, 0.673, 0.697, 0.808, 0.895, 0.929, and 1.215 MeV, all of which are known from previous measurements [32, 59]. The 10 keV/bin region includes photo-peaks at 2.023,

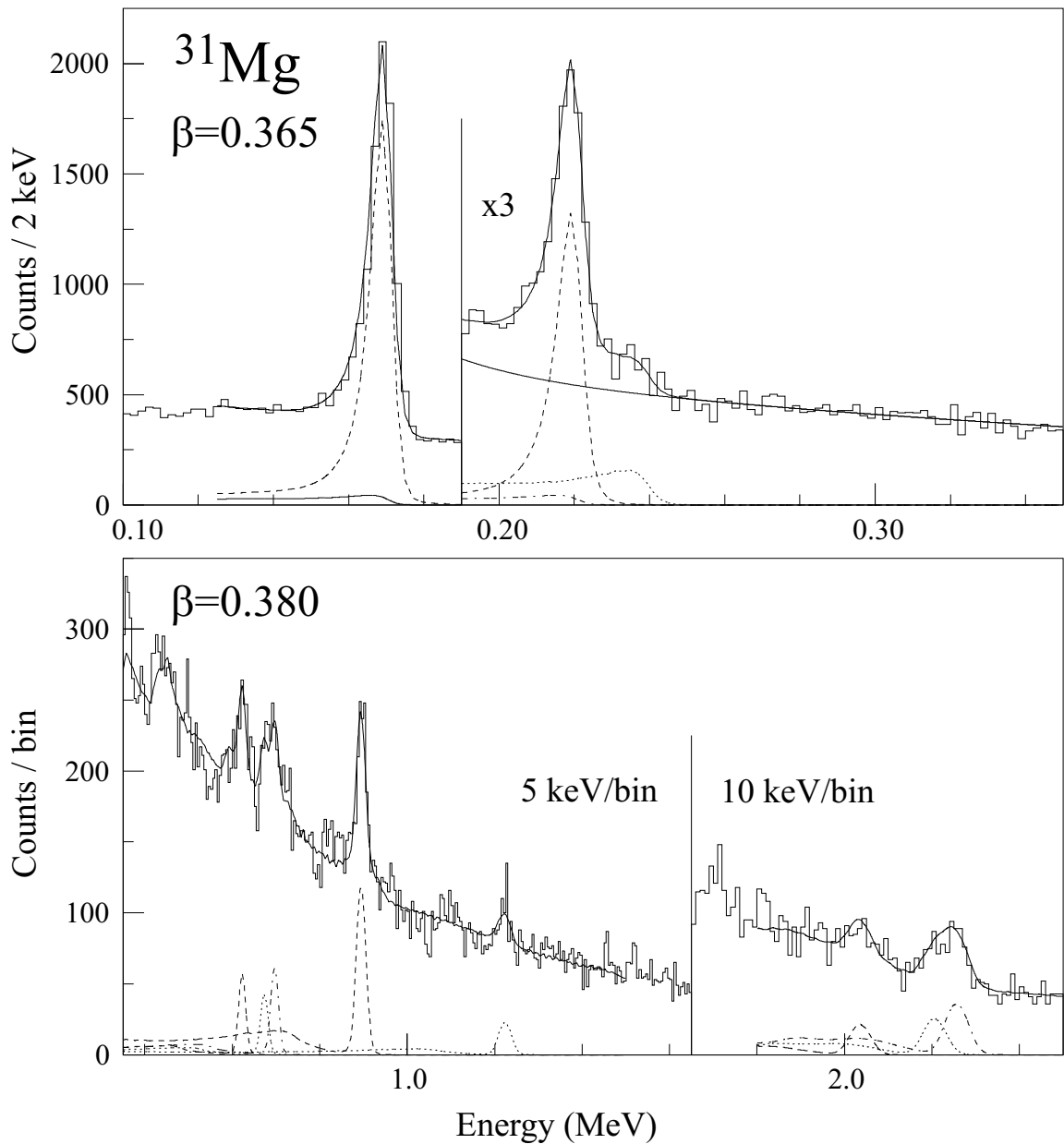


Figure 3.15: Gamma-ray spectrum for  $^{31}\text{Mg}$ . The upper panel shows the low energy region of the spectrum which is Doppler-reconstructed using a post-target fragment velocity. The lower panel shows the remainder of the analyzed spectrum, Doppler-reconstructed using a mid-target fragment velocity. Results of statistical fits to each region of the spectrum are overlaid with individual photo-peak response functions also plotted.

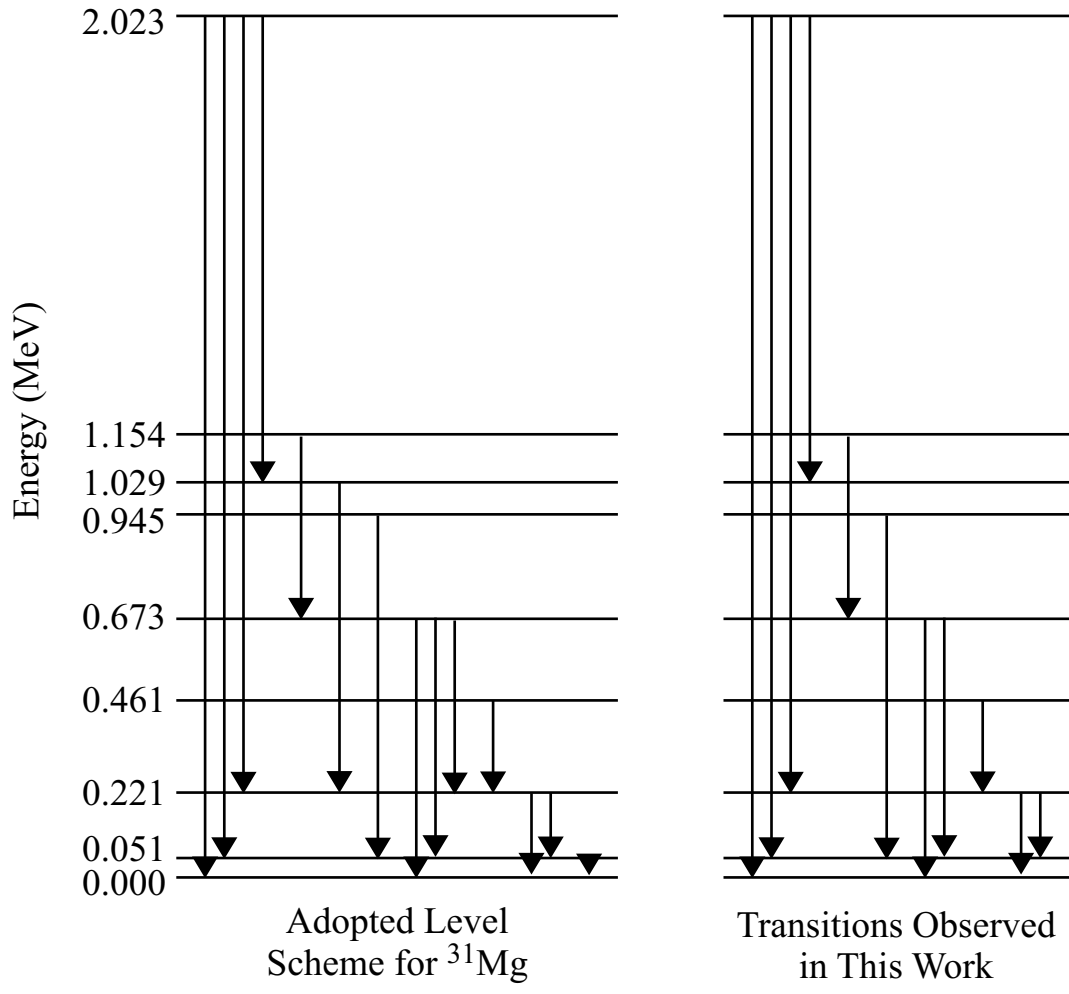


Figure 3.16: Comparison of observed  $\gamma$ -ray transitions to the adopted level scheme of  $^{31}\text{Mg}$ . The adopted scheme is shown on the left while the observed transitions are illustrated on the right. All observed transitions are in agreement with adopted energies to within observational uncertainties.

$E_{level}$ (MeV)	$E_{\gamma}$ (MeV)	I (%)	b (%)	$\sigma$ (mb)
0.0000				
0.0505			34.5(70)	32.4(71)
0.2210	0.2210	6.50(45)	22.5(25)	21.1(30)
	0.1705	19.1(12)		
0.461	0.240	22.1(58)	22.1(59)	20.7(59)
0.6731	0.6731	1.1(11)	2.5(18)	2.4(17)
	0.6226	1.4(11)		
	0.4521	0.0(10)		
0.9451	0.8946	4.8(11)	4.8(11)	4.5(11)
1.154	0.697	1.7(11)	1.7(11)	1.6(10)
1.0286	0.8076	0.0(10)	-1.5(15)	
1.390	0.929	0.0(10)	0.0(10)	
2.2435	2.2435	3.4(12)	8.8(22)	8.2(22)
	2.1930	2.3(11)		
	2.0225	1.7(11)		
	1.2149	1.5(11)		

Table 3.5: Gamma-ray intensities and branching ratios for  $^{31}\text{Mg}$ .

2.193, and 2.244 MeV, also known from previous measurements. Branching ratios are determined by intensity balancing, and results of this analysis are summarized in table 3.5. Several peaks included in the fit have intensities that are consistent with zero and are not included in the table. Unexplained fluctuations in the  $\gamma$ -ray spectrum require that an additional 1% absolute uncertainty be included to intensities extracted above 0.5 MeV.

### 3.4.2 Longitudinal Momentum Distribution

Longitudinal momentum distributions are extracted by gating on photo-peak events in the  $\gamma$ -ray spectrum. Gates are applied to the 0.171-, 0.221-, 0.895-MeV photo-peaks and the doublet at 2.244 MeV. Contributions from the under-lying background in the  $\gamma$ -ray spectrum are estimated using the fit to the spectrum. For the 0.171-MeV and 0.221-MeV distributions, the background distribution is obtained from a gate on  $\gamma$ -ray energies between 0.25 and 0.32 MeV. For the remaining distributions, the background distribution is taken from energies above 2.5 MeV. The 0.171-MeV

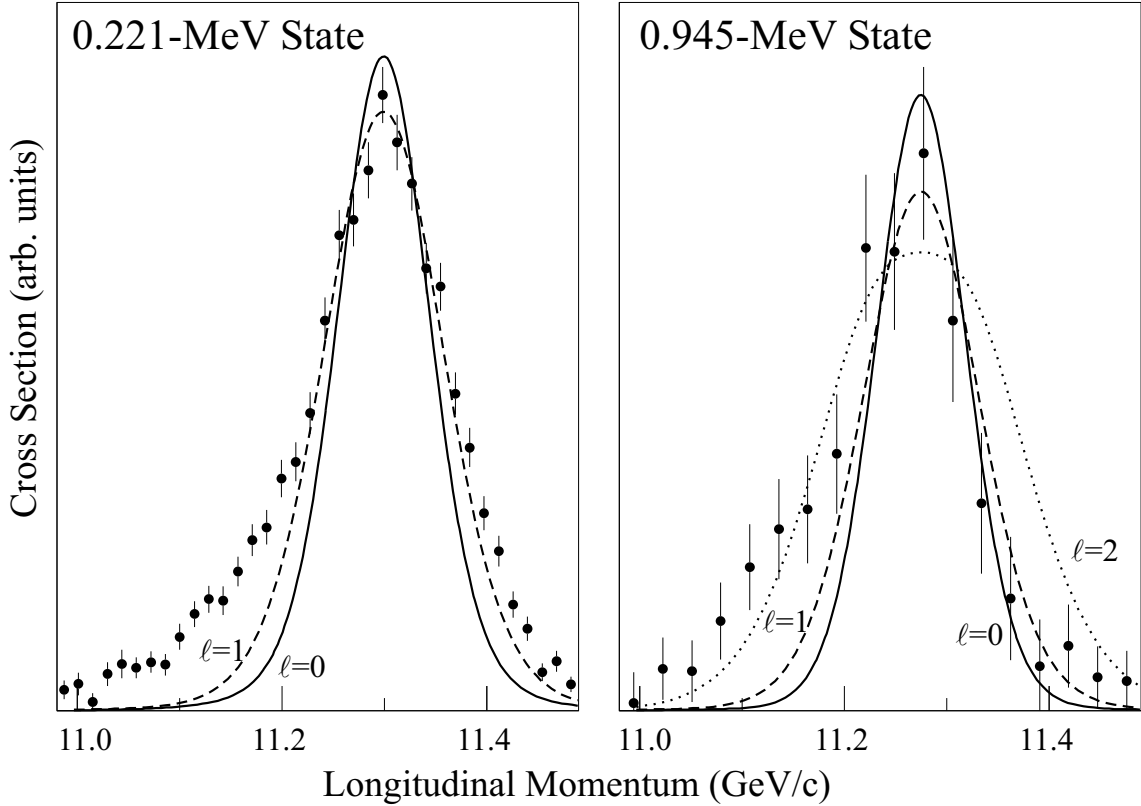


Figure 3.17: Longitudinal momentum distributions for  $^{31}\text{Mg}$ . The panel on the left shows the distribution associated with the population of the 0.221-MeV excited state while the right panel is that for the 0.945-MeV state. Both distributions are overlaid with calculated curves assuming  $\ell=0$  (solid),  $\ell=1$  (dashed), and  $\ell=2$  (dotted).

and 0.221-MeV distributions are identical in shape as would be expected since these  $\gamma$ -rays are emitted from the same state. Therefore, a combined 0.171-MeV and 0.221-MeV gate is used to extract the summed distribution for these two photo-peaks. The background-subtracted and acceptance-corrected momentum distributions are shown in figure 3.17. The distribution for the 0.221-MeV state is extracted with good quality and shows good agreement with  $\ell=1$ . Poor statistics in the 0.895-MeV photo-peak limits the quality of the extracted momentum distributions. However, this distribution is clearly quite narrow, indicating  $\ell=0,1$ . Given the limited statistics and poor peak-to-total ratio for the 0.240 MeV transition, it is not possible to extract a momentum distribution for the populations of this state.

Acceptance corrections are applied within the acceptance window of the spec-

trograph. The momentum distribution for the state at 0.221 MeV is narrow, and extrapolated corrections for this partial cross section are negligible. However, since momentum distributions are not extracted for the other populated final states, no estimation of extrapolated acceptance corrections is possible. Therefore, extrapolated acceptance corrections are not included in the reported results.

# Chapter 4

## Discussion

### 4.1 $^{26}\text{Ne}$

For the  $N = 16$  nucleus  $^{26}\text{Ne}$ , USD calculations predict an enhancement of the  $2s_{1/2} - 1d_{3/2}$  subshell gap. Such an enhancement results in a relatively small  $\nu 1d_{3/2}$  occupancy in the ground state wave function as is shown in table 4.1. The four strongest spectroscopic factors for  $^{26}\text{Ne}$  are also listed in table 4.1. With the exception of a 0.01 spectroscopic factor to a  $3/2^+$  state at  $\approx 3$  MeV, table 4.1 includes all of the USD-predicted spectroscopic strength to states in  $^{25}\text{Ne}$  with excitation energy below the neutron separation energy. The listed spectroscopic strength indicates that the single-neutron knockout reaction on  $^{26}\text{Ne}$  will lead to a strong population of a  $1/2^+$  ground state and two  $5/2^+$  excited states and weak population of a  $3/2^+$  excited state. The states populated in the  $^{25}\text{Ne}$  residue are in qualitative agreement with this prediction, with strong feeding to the  $1/2^+$  ground state and two  $\ell = 2$  excited states and weaker feeding to the  $3/2^+$  state at 2.09 MeV.

A quantitative comparison is given by the ratio of the observed spectroscopic factor to the calculated factor with a center of mass correction applied [60]. These ratios are 1.10(8), 0.59(4), 0.57(9), and 0.88(25) for the  $1/2_1^+$ ,  $5/2_1^+$ ,  $5/2_2^+$ , and  $3/2_1^+$  states, respectively. In general, these ratios are found to be dependent on the binding

$E_{level}$	$\ell$	$\sigma_{exp}$	$\sigma_{sp}$	$C^2S_{exp}$	$J^\pi$	$C^2S_{USD}$	$\langle n \rangle_{USD}$	$\langle n \rangle_{SDPF-M}$
0.000	0	45(4)	30.8	1.48(11)	$\frac{1}{2}^+$	1.25	1.61	1.74
1.703	2	27(2)	19.3	1.38(10)	$\frac{5}{2}^+$	2.17	5.67	5.68
3.316	2	19(3)	17.7	1.05(16)	$\frac{3}{2}^+$	1.70		
2.090		7(2)	18.7	0.36(10)	$\frac{3}{2}^+$	0.38	0.72	0.48
								0.08
								0.02
							$\Sigma = 8$	$\Sigma = 8$

Table 4.1: Deduced and calculated spectroscopic factors and single-particle occupancies for  $^{26}\text{Ne}$ . Spectroscopic factors are labeled  $C^2S$  and are only given from the USD calculation. Single-particle occupancies are labeled as  $\langle n \rangle$ .

of the removed nucleon [37, 40, 61]. For the binding energies of nucleons removed from  $^{26}\text{Ne}$ , the ratio is expected to be in the range of 0.5 to 0.8. The observed  $5/2^+$  and  $3/2^+$  strengths are in good agreement with USD shell model predictions when this systematic reduction factor is included. However, the deduced  $1/2^+$  spectroscopic factor is approximately 1.4(3) to 2.2(5) times larger than predicted. The uncertainty in this factor includes the 20% sensitivity of the calculated single-particle cross section discussed in section 1.6.2.

SDPF-M calculations for  $^{26}\text{Ne}$  are in agreement with the USD predictions, illustrating the absence of intruder effects in the ground state of this nucleus. Spectroscopic factors are not yet available from MCSM calculations. The only quantitative measure of the content of the wavefunction are the occupancies in the various single-particle orbits. These occupancies are listed in table 4.1 next to the corresponding USD calculations. The SDPF-M predicts less occupancy in the  $1d_{3/2}$  orbital than the USD predictions, indicating an even more enhanced  $N = 16$  subshell closure. Occupancy for the  $1f_{7/2}$  and  $2p_{3/2}$  single-particle states, which are outside of the USD model, are predicted to be very small. This prediction is verified by the good agreement between the observed spectroscopic strength and the USD predictions, which include no intruder effects.

$E_{level}$	$\ell$	$\sigma_{exp}$	$\sigma_{sp}$	$C^2S_{exp}$	$J^\pi$	$C^2S_{USD}$	$\langle n \rangle_{USD}$	$\langle n \rangle_{SDPF-M}$
"gs"	2	20.6(18)	21.7		$1d_{3/2}$	1.75	2.18	1.18
	3		19.8		$1f_{7/2}$	—	—	0.89
0.765	(0,1)	10.3(12)	31.6*	0.33(4)	$2p_{3/2}$	—	—	0.24
0.885	(0,1)	35.0(27)	31.6*	1.11(8)	$2s_{1/2}$	1.50	1.93	1.87
					$1d_{5/2}$	—	5.88	5.83

\*This is an average value of the  $\ell = 0$  and  $\ell = 1$  cross sections which differ by only 1%.

Table 4.2: Deduced and calculated spectroscopic factors and single-particle occupancies for  $^{28}\text{Ne}$ . Spectroscopic factors are labeled  $C^2S$  and are only given from the USD calculation. Single-particle occupancies are labeled as  $\langle n \rangle$ .

## 4.2 $^{28}\text{Ne}$

For the  $N = 18$   $^{28}\text{Ne}$  the differences between predictions from the USD and SDPF-M interactions are substantial. The USD and SDPF-M single-particle occupancies are listed in the right-most columns of table 4.2. The occupancies in the  $1d_{5/2}$  and  $2s_{1/2}$  single-particle states are nearly identical between the two calculations, demonstrating the enhanced  $N = 16$  subshell gap predicted by both interactions. However, the USD-calculated occupancy in the  $1d_{3/2}$  state appears to be shared with the  $fp$  states in the SDPF-M results. While the SDPF-M indicates a relatively small occupancy in the  $1p_{3/2}$  single-particle orbit (approximately half of the  $1d_{3/2}$  occupancy in  $^{26}\text{Ne}$ ), the  $1f_{7/2}$  occupancy of 0.89 is nearly as large as that for the  $1d_{3/2}$  single-particle state. With an  $fp$  shell occupancy of 1.13 summed over  $2\hbar\omega$ ,  $4\hbar\omega$ ..., the ground state wavefunction is comprised of  $\approx 45\%$  intruder configurations, if most of the occupancy is assumed to lie in  $2\hbar\omega$  configurations.

USD and SDPF-M results also differ greatly for the residual  $^{27}\text{Ne}$  nucleus. A comparison of the calculated low-energy level structure is shown in figure 4.1. Whereas only one bound excited state is predicted with the USD interaction, SDPF-M calculations indicate three bound excited states. The  $3/2^+$  ground state and  $1/2^+$  0.94 MeV excited state predicted from the SDPF-M interaction correspond to the two USD-predicted states based on the calculated spin, parity, and  $fp$  occupancy. How-

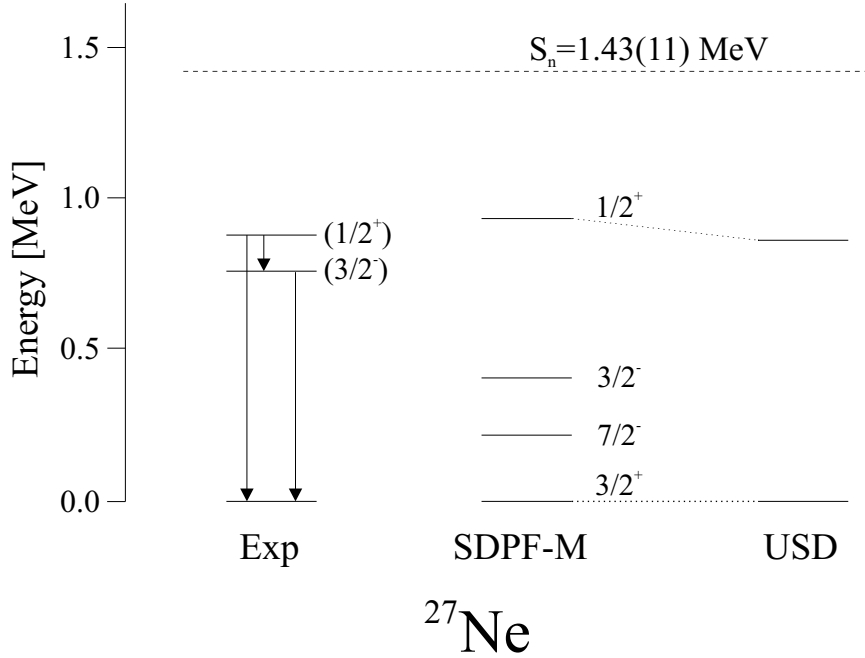


Figure 4.1: Deduced and calculated level scheme for  $^{27}\text{Ne}$ .

ever, the two negative parity states are clearly intruder states outside the model space of the USD interaction. For the case of  $^{27}\text{Ne}$ , the effect of the weakened  $N = 20$  shell gap would be to increase the low-energy level density from two bound states to four.

The  $^{28}\text{Ne}$  single-neutron knockout measurement reveals population of two bound excited states in  $^{27}\text{Ne}$ . The presence of multiple bound excited states is already an indication that intruder effects are important in this nucleus. Further, the longitudinal momentum distributions extracted for the populated excited states suggest an angular momentum assignment of  $\ell = 0$  or  $\ell = 1$  for both excited states. To obtain agreement with the USD interaction, both excited states must be assigned  $\ell = 0$  and a major adjustment of the interaction would be necessary to produce such states at low excitation energy. Therefore, the  $\ell$ -value restriction suggests that at least one of the populated states is an intruder.

The observed spectroscopic strength also shows qualitative agreement with SDPF-M predictions. Given the enhanced  $N = 16$  sub-shell closure and the dominance of  $0\hbar\omega$  configurations, the USD spectroscopic factor should be a good approximation

of the SDPF-M factor for the  $1/2^+$  excited state. The center-of-mass corrected ratio between the spectroscopic strengths to the observed 0.885-MeV state and USD-calculated  $1/2^+$  state is 0.66(4), which indicates good agreement between calculation and observation, while the same ratio for the 0.765-MeV state is 0.20(1), showing poor agreement. Although, there is no estimate of the SDPF-M  $1d_{3/2}$  spectroscopic factor, the  $1d_{3/2}$  occupancy serves as an upper limit. The observed spectroscopic strength for the 0.765-MeV state is comparable to the upper limit for a  $J^\pi = 3/2^-$  state. Given the clear presence of an intruder state and the overall agreement of the observed spectroscopic strength with SDPF-M predictions, the 0.885-MeV and 0.765-MeV states are assigned spin and parities of  $1/2^+$  and  $3/2^-$ , respectively.

The non-observation of a third excited state, namely the  $7/2^-$  state, predicted by SDPF-M calculations seems to put into question the arguments presented so far. However, if the low-lying  $7/2^-$  exists and is not observed in the present measurement, it would be isomeric, decaying by emission of an  $M2$   $\gamma$ -ray to the  $3/2^+$  ground state or by a low-energy  $E2$  to the  $3/2^-$  state, depending on its excitation energy. The long lifetime of this state, which would be on the order of microseconds or longer, leads to a situation in which essentially all photons are emitted beyond the range of the  $\gamma$ -ray detectors. If such an isomer is populated and not tagged, those events would be grouped with the ground state events. The only possibility for delineating such a scenario would be to observe a significant deviation in the “ground state” cross section and/or momentum distribution. Unfortunately in this case, the extracted momentum distribution is of poor quality. This distribution is shown in figure 4.2 with calculated distributions overlaid assuming population of a single  $\ell = 2$  state (USD) and a combination of an  $\ell = 2$  and  $\ell = 3$  state (SDPF-M) weighted according to the corresponding SDPF-M occupancies. The two calculated distributions are rather similar, and both are consistent with the extracted distribution. The same situation hold true for the “ground state” cross section. So, although the existence of the low-lying  $7/2^-$  is not shown in the present results, non-observation in this measurement

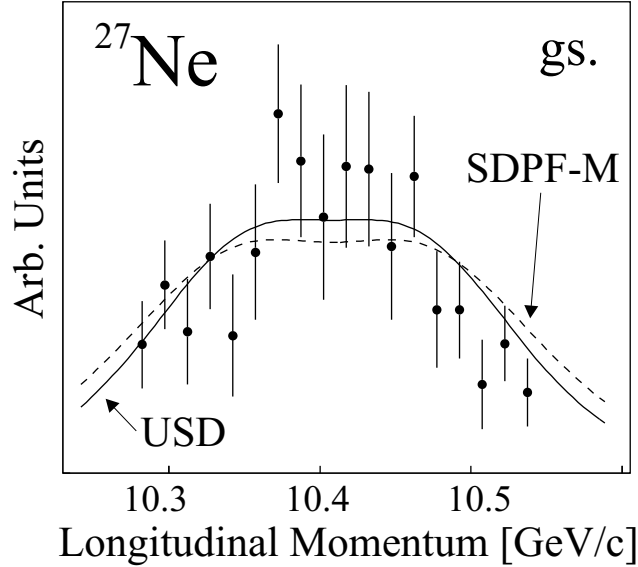


Figure 4.2: Longitudinal momentum distribution for events populating the ground state of  $^{27}\text{Ne}$ . The deduced distribution is overlaid with two calculated distributions. The solid line represents a pure  $\ell=2$  distribution predicted by USD calculations while the dashed line includes both  $\ell = 2$  and  $\ell = 3$  components to accommodate population of the SDPF-M predicted  $7/2^-$  isomer. Both calculations are consistent with the extracted distribution.

is not inconsistent with SDPF-M predictions.

### 4.3 $^{30}\text{Mg}$

Previous results from  $\beta$  decay and  $\beta$ -delayed neutron decay measurements suggest that the states at 1.095 MeV, 1.431 MeV, and 2.266 MeV have negative parity. This conclusion for the 1.095 MeV and 1.431 MeV states is supported in the present work by the observed  $\ell = 1$  and  $\ell = 3$  character of the momentum distributions associated with the population of the respective states. Analysis of the observed momentum distribution allow a restriction of  $(1/2, 3/2)^-$  for the 1.095-MeV state and  $(5/2, 7/2)^-$  for the 1.431-MeV state. Unfortunately, the momentum distribution for the 2.266-MeV state is not well extracted and no such conclusions are drawn for this state. As further evidence of the relative difference in  $J^\pi$  between the 1.095-MeV and 1.431-MeV states, the measured half-life of the latter translates to a  $B(E2)$  of  $103(19) e^2\text{fm}^4$

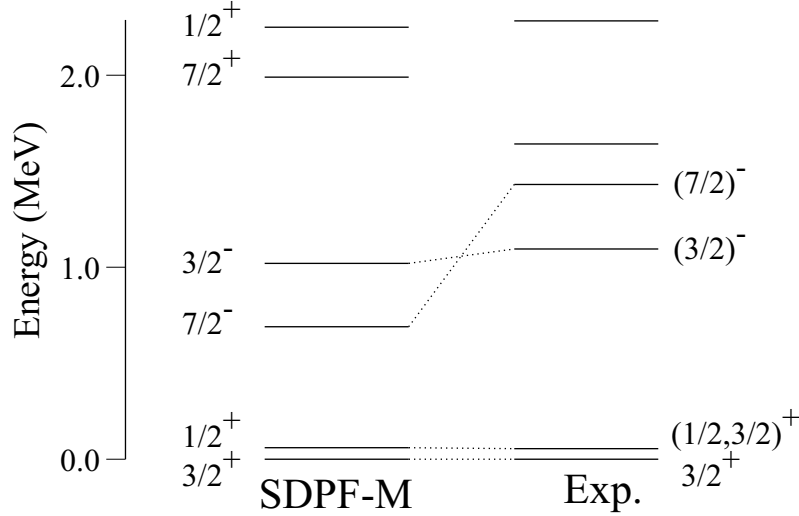


Figure 4.3: Deduced and calculated low-energy level scheme for  $^{29}\text{Mg}$ .

or 19.5(35) W.U. The assumption of  $E1$  or pure  $M1$  lead to hindered transition strengths on the order of  $10^{-5}$  to  $10^{-4}$  W.U., and high multiplicities are excluded by comparison to suggested upper limits [54].

The SDPF-M calculated level scheme is compared to USD predictions and the presently known scheme in figure 4.3. While the low-lying  $\ell = 1$  state is within 0.1 MeV, suggesting a tentative assignment of  $3/2^-$ , the  $\ell = 3$  state is  $\approx 0.7$  MeV higher in energy than the SDPF-M-predicted  $7/2^-$  state. The clear observation of negative parity states at low excitation energy, as concluded from  $\beta/\beta$ -n measurements, suggests the existence of intruder states in the low-energy level structure. Within the constraints provided by the momentum distribution, the  $7/2^-$  assignment for the 1.431-MeV state is the more likely scenario.

With tentative assignments for the two low-lying negative parity states, the ratio of the observed cross section to the calculated single-particle cross section gives the observed spectroscopic strength to each state, given in table 4.3. Although spectroscopic factors are not yet available from MCSM calculations, the observed spectroscopic strength is compared to upper limits provided by the SDPF-M-calculated total occupancy in each single-particle state. The predicted occupancy in the  $\nu 2p_{3/2}$  orbital is rather small at 0.081 neutrons. The observed spectroscopic strength in the

lowest  $3/2^-$  state is already more than twice the predicted full occupancy of the corresponding single-particle state, revealing a significant deviation from SDPF-M calculations. However, given the small predicted occupancy, the approximate factor of two gives only a modest deviation of 0.11(7). The observed  $7/2_1^-$  spectroscopic strength is less than the SDPF-M upper limit, accounting for 70(20)% of the calculated  $\nu 1f_{7/2}$  occupancy.

The observed spectroscopic strength to the lowest two negative parity states appears to be consistent with single-particle occupancies calculated with the SDPF-M interaction. However, there is an additional negative parity state suggested at 2.266 MeV based on  $\beta$ -decay measurements. In the present measurement, significant direct feeding is measured to a state at 2.283 MeV, which is assumed to be the 2.266-MeV state of reference [57]. While the extracted momentum distribution for this state is not of sufficient quality to yield a definitive  $\ell$  identification, the width of distributions makes an assignment of  $\ell = 3$  unlikely. Therefore, if this state is found to be a negative parity state, then the present work indicates a spin constraint of  $(1/2, 3/2)$ . The former perhaps indicating the influence of the  $2p_{1/2}$  single-particle state, which is outside of the SDPF-M model space, and the latter suggesting a more significant under-estimation of the total  $2p_{3/2}$  occupancy in the ground state of  $^{30}\text{Mg}$ .

## 4.4 $^{32}\text{Mg}$

A number of previous measurements constrain the spin and parity assignments in the low-energy level scheme of  $^{31}\text{Mg}$ . Results from  $\beta$  decay and  $\beta$ -delayed neutron measurements suggest three negative parity states at 0.221, 0.240, and 1.39 MeV [32]. Although Klotz *et al.* are able to constrain the multipolarity of several of the transitions in the  $^{31}\text{Mg}$  level scheme, more recent measurements have gone further in determining the transition multipolarities and  $J^\pi$  assignments. The ground state spin and parity have been determined to be  $1/2^+$  [33], and measured lifetimes of the

$E_{level}$	$\ell$	$\sigma_{exp}$	$\sigma_{sp}$	$C^2S_{exp}$	$J^\pi$	$\langle n \rangle_{SDPF-M}$
0.000	(2)	49.2(43)	17.9		$1d_{3/2}$	1.819
0.055	(0)		25.3		$2s_{1/2}$	1.813
1.095	1	4.3(15)	22.8	0.19(7)	$2p_{3/2}$	0.081
1.431	3	$5.8^{+1.1}_{-1.8}$	16.4	$0.35^{+0.07}_{-0.11}$	$1f_{7/2}$	0.515
1.642	2	7.3(16)	16.0	0.46(1)	$1d_{5/2}$	5.773
2.283		3.7(10)				
2.500	(2,3)	3.7(14)				
2.615	(0,1)	6.9(15)				
3.232	2	22.9(24)	15.5	1.48(15)		
3.674		2.3(10)				

Table 4.3: Deduced spectroscopic strengths and calculated single-particle occupancies for  $^{30}\text{Mg}$ . With the exception of  $\ell$ -values given for the ground state doublet, the listed  $\ell$ -values indicate values or constraints deduced in the present work. Values given for the ground state doublet are assumed based on spin and parity assignments from previous measurements.

0.221-MeV, 0.461-MeV, and a newly observed 1.154-MeV excited state [59] along with the measured lifetime of the 0.051-MeV state [32] give more definitive constraints on the multipolarity of the transitions.

Citing recommended transition rate upper limits, the 0.051-MeV, 0.171-MeV, and 0.221-MeV transitions are all dipole transition while an  $E2$  multipolarity is also possible for the 240-keV transition. Results from the present work include a  $\ell = 1$  assignment for the 0.221-MeV state which limits the multipolarity to  $(1/2, 3/2)^-$ , in agreement with the known dipole multipolarity of the transition linking this state to the  $1/2^+$  ground state. As the momentum distribution is not extracted for the 0.461-MeV level, the tentative spin and parity assignment of  $(7/2^-)$  for this level is taken from Mach *et al.*

The observed level structure is compared to SDPF-M predictions in figure 4.4. Contrary to observation, two negative parity states are predicted below the positive-parity  $J = 1/2, 3/2$  doublet. However, the first four known and calculated states are within a range of 0.5 MeV, suggesting no gross contradiction between the two.

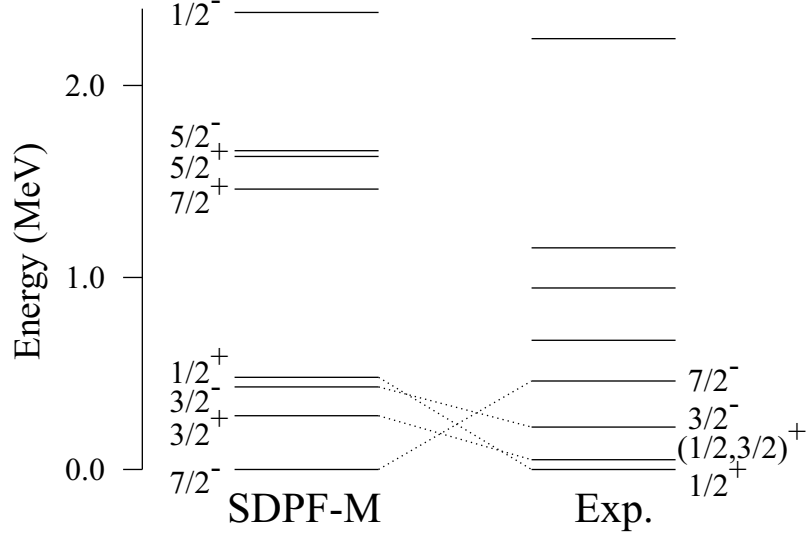


Figure 4.4: Deduced and calculated level scheme for  $^{31}\text{Mg}$ .

Introduction of intruder effects in the effective interaction leads to a  $3/2^-$  and  $7/2^-$  state at low excitation energy in the  $^{31}\text{Mg}$  level scheme. The predicted low-lying  $3/2^-$  state motivates the tentative spin and parity assignment of  $(3/2)^-$  for the 0.221-MeV state, given the constraints discussed in the previous paragraph.

The observed spectroscopic strengths to the tentatively-assigned low-lying  $3/2^-$  and  $7/2^-$  states are listed in table 4.4. Again, as with the  $^{30}\text{Mg}$  measurement, the  $3/2_1^-$  spectroscopic strength is found to exceed the SDPF-M upper limit by more than a factor of two. The higher predicted occupancy in the present case and the similar deviation observed for both  $^{30}\text{Mg}$  and  $^{32}\text{Mg}$  suggest a significant systematic underestimation of the occupancy of the  $2p_{3/2}$  single-particle state in these nuclei. While a significant deviation is observed for the  $3/2_1^-$ , the observed  $7/2_1^-$  spectroscopic strength is consistent with the SDPF-M-predicted upper limit. Further, the observed strength in the  $7/2_1^-$  state is  $\approx 70\%$  of the predicted full occupancy in both the present and  $^{30}\text{Mg}$  cases.

$E_{level}$	$\ell$	$\sigma_{exp}$	$\sigma_{sp}$	$C^2S_{exp}$	$J^\pi$	$\langle n \rangle_{SDPF} - M$
0.000	(0)	32.4(71)	25.9		$2s_{1/2}$	1.897
0.051	(2)		17.4		$1d_{3/2}$	2.119
0.221	1	21.1(30)	26.3	0.80(11)	$2p_{3/2}$	0.323
0.461	(3)	20.7(59)	16.0	1.29(37)	$1f_{7/2}$	1.827
0.673		2.4(17)			$1d_{5/2}$	5.833
0.945		4.5(11)				
1.154		1.6(10)				
2.244		8.2(22)				

Table 4.4: Deduced spectroscopic factors and calculated single-particle occupancies for  $^{32}\text{Mg}$ . The  $\ell$ -values given in parentheses are assumed based in previous measurements while the value for the state at 0.221 MeV is deduced from the present measurement.

# Chapter 5

## Summary

Individual states in  $^{25}\text{Ne}$  and  $^{27}\text{Ne}$  have been populated in one-neutron knockout reactions. For  $^{25}\text{Ne}$ , the level scheme, spin assignments, and spectroscopic strengths are in agreement with USD shell-model calculations. Spin and parity  $1/2^+$  could be unambiguously assigned to the ground state of  $^{25}\text{Ne}$ . USD and SDPF-M shell model predictions agree for this nucleus, indicating that intruder states do not play a role for the low-lying level scheme of this  $N = 15$  nucleus.

With just two neutrons more,  $^{27}\text{Ne}$  is predicted to have low-lying negative-parity intruder states by the SPDF-M Monte-Carlo shell-model calculations, while the USD shell model yields a  $1/2^+$  state as the only bound, excited state. Two excited states have been observed in the present experiment. The  $\ell$ -values deduced from the longitudinal momentum distributions of the  $^{27}\text{Ne}$  knockout residues and the spectroscopic factors obtained in comparison to eikonal reaction theory support the identification of the 0.765 MeV and 0.885 MeV excited states as the  $3/2^-$  and  $1/2^+$  levels, respectively. This result confirms the importance of intruder states in the ground state configuration of  $^{28}\text{Ne}$  and the predictive power of the SDPF-M Monte Carlo Shell Model calculations in this transitional region.

Single-neutron knockout from  $^{30,32}\text{Mg}$  measurements reveal significant direct population of negative parity states in the  $^{29,31}\text{Mg}$  residues, suggesting the pres-

ence of  $N = 20$  cross shell intruder configurations in the  $^{30,32}\text{Mg}$  ground states. With tentative  $J^\pi$  assignments for the  $^{29}\text{Mg}$  excited states at 1.095 MeV and 1.431 MeV and the  $^{31}\text{Mg}$  excited states at 0.221 MeV and 0.461 MeV, spectroscopic factors are extracted which quantify the extent of these intruder admixtures. SDPF-M calculations indicate a small but significant  $fp$  occupancy in the  $^{30}\text{Mg}$  ground state. However, for  $^{32}\text{Mg}$ , the single-particle occupancies appear virtually unchanged from the  $^{30}\text{Mg}$  with the exception of two additional neutrons in  $fp$  orbits. The total observed spectroscopic strength in  $fp$  single-particle states for  $^{30}\text{Mg}$  is  $0.54_{-0.13}^{+0.10}$  while, for  $^{32}\text{Mg}$ , it is more than three times as large at 2.09(39), indicating a dramatic shift in structure with the addition of just two neutrons. The ratio between these observed strengths is in good agreement with SDPF-M predicted  $fp$  occupancies for these two nuclei, again illustrating the predictive power of the SDPF-M interaction in this region. It is noted that while the  $7/2^-$  spectroscopic strengths appear to be consistent with SDPF-M calculations, the observed  $3/2^-$  strengths in the present measurement suggest a systematic under-prediction of these strengths.

# Bibliography

- [1] M. Theonnessen. Reaching the limits of nuclear stability. *Rep. Prog. Phys.*, 67:1187–1232, 2004.
- [2] Aage Bohr and Ben Mottelson. *Nuclear Structure*, volume 1. World Scientific Publishing Company, 1969.
- [3] L. Grodzins. The uniform behavior of electric quadrupole transition probabilities from first  $2^+$  states in even-even nuclei. *Phys. Lett.*, 2:88–91, 1962.
- [4] B. A. Brown. The nuclear shell model towards the drip lines. *Prog. Part. Nucl. Phys.*, 47:517–599, 2001.
- [5] A. Ozawa, T. Kobayashi, T. Suzuki, K. Yoshida, and I. Tanihata. New magic number,  $N = 16$ , near the neutron drip line. *Phys. Rev. Lett.*, 84:5493–5495, 2000.
- [6] P. D. Cottle and K. W. Kemper. Evolution of shell closures in neutron-rich  $Z = 10 - 20$  nuclei. *Phys. Rev. C*, 66:061301, 2002.
- [7] P. Navrátil, J. P. Vary, and B. R. Barrett. Properties of  $^{12}\text{C}$  in the *ab initio* nuclear shell model. *Phys. Rev. Lett.*, 84:5728–5731, 2000.
- [8] B.A. Brown. New skyrme interaction for normal and exotic nuclei. *Phys. Rev. C*, 58:220–231, 1998.
- [9] B.H. Wildenthal. Empirical strengths of spin operators in nuclei. *Prog. Part. Nucl. Phys.*, 11:5, 1984.
- [10] Y. Utsuno, T. Otsuka, T. Mizusaki, and M. Honma. Varying shell gap and deformation in  $N = 20$  unstable nuclei studied by the monte carlo shell model. *Phys. Rev. C*, 60:054315, 1999.
- [11] M. Honma, T. Mizusaki, and T. Otsuka. Diagonalization of hamiltonians for many-body systems by auxiliary field quantum monte carlo technique. *Phys. Rev. Lett.*, 75:1284–1287, 1995.
- [12] T. Otsuka, M. Honma, T. Mizusaki, N. Shimizu, and Y. Utsuno. Monte carlo shell model for atomic nuclei. *Prog. Part. Nucl. Phys.*, 47:319–400, 2001.

- [13] T. Otsuka, R. Fujimoto, Y. Utsuno, B. A. Brown, M. Honma, and T. Mizusaki. Magic numbers in exotic nuclei and spin-isospin properties of the  $NN$  interaction. *Phys. Rev. Lett.*, 87:082502, 2001.
- [14] E. Warburton and B. A. Brown. Effective interactions for the  $0p1s0d$  nuclear shell-model space. *Phys. Rev. C*, 46:923–944, 1992.
- [15] M. Stanoiu, F. Azaiez, Zs. Dombrádi, O. Sorlin, B. A. Brown, M. Belleguic, D. Sohler, M. G. Saint Laurent, M. J. Lopez-Jimenez, Y. E. Penionzhkevich, G. Sletten, N. L. Achouri, J. C. Angélique, F. Becker, C. Borcea, C. Bourgeois, A. Bracco, J. M. Daugas, Z. Dlouhý, C. Donzaud, J. Duprat, Zs. Fülöp, D. Guillemaud-Mueller, S. Grévy, F. Ibrahim, A. Kerek, A. Krasznahorkay, M. Lewitowicz, S. Leenhardt, S. Lukyanov, P. Mayet, S. Mandal, H. van der Marel, W. Mittig, J. Mrázek, F. Negoita, F. De Oliveira-Santos, Zs. Podolyák, F. Pougheon, M. G. Porquet, P. Roussel-Chomaz, H. Savajols, Y. Sobolev, C. Stodel, J. Timár, and A. Yamamoto.  $N = 14$  and  $16$  shell gaps in neutron-rich oxygen isotopes. *Phys. Rev. C*, 69:034312, 2004.
- [16] A. Obertelli, S. Péru, J.-P. Delaroche, A. Gillibert, M. Girod, and H. Goutte.  $N = 16$  subshell closure from stability to the neutron drip line. *Phys. Rev. C*, 71:024304, 2005.
- [17] H. Sakurai, S.M. Lukyanov, M. Notani, N. Aoi, D. Beaumel, N. Fukuda, M. Hirai, E. Ideguchi, N. Imai, M. Ishihara, H. Iwasaki, T. Kubo, K. Kusaka, H. Kumagai, T. Nakamura, H. Ogawa, Yu.E. Penionzhkevich, T. Teranishi, Y.X. Watanabe, K. Yoneda, and A. Yoshida. Evidence for particle stability of  $^{31}\text{F}$  and particle instability of  $^{25}\text{N}$  and  $^{28}\text{O}$ . *Phys. Lett. B*, 448:180, 1999.
- [18] C. Thibault, R. Klapisch, C. Rigaud, A. M. Poskanzer, R. Prieels, L. Lessard, and W. Reisdorf. Direct measurement of the masses of  $^{11}\text{Li}$  and  $^{26-32}\text{Na}$  with an on-line mass spectrometer. *Phys. Rev. C*, 12:644, 1975.
- [19] D. J. Vieira, J. M. Wouters, K. Vaziri, Jr. R. H. Kraus, H. Wollnik, G. W. Butler, F. K. Wohn, and A. H. Wapstra. Direct mass measurement of neutron-rich light nuclei near  $N = 20$ . *Phys. Rev. Lett.*, 57:3253, 1986.
- [20] C. Détraz, D. Guillemaud, G. Huber, R. Klapisch, M. Langevin, F. Naulin, C. Thibault, L. C. Carraz, and F. Touchard. Beta decay of  $^{27-32}\text{Na}$  and their descendants. *Phys. Rev. C*, 19:164, 1979.
- [21] T. Motobayashi, Y. Ikedaa, Y. Ando, K. Ieki, M. Inoue, N. Iwasa, T. Kikuchi, M. Kurokawaa, S. Moriya, S. Ogawa, H. Murakamia, S. Shimouraa, Y. Yanagisawa, T. Nakamura, Y. Watanabe, M. Ishihara, T. Teranishi, H. Okuno, and R.F. Casten. Large deformation of the very neutron-rich nucleus  $^{32}\text{Mg}$  from intermediate-energy coulomb excitation. *Phys. Lett. B*, 346:9, 1995.
- [22] J. A. Church, C. M. Campbell, D.-C. Dinca, J. Enders, A. Gade, T. Glasmacher, Z. Hu, R. V. F. Janssens, W. F. Mueller, H. Olliver, B. C. Perry, L. A. Riley, , and K. L. Yurkewicz. Measurement of  $E2$  transition strengths in  $^{32,34}\text{Mg}$ . *Phys. Rev. C*, 72:054320, 2005.

- [23] E. Warburton, J. A. Becker, and B. A. Brown. Mass systematics for  $A = 29 - 44$  nuclei: The deformed  $A \sim 32$  region. *Phys. Rev. C*, 41:1147, 1990.
- [24] X. Campi, H. Flocard, A. K. Kerman, and S. Koonin. Shape transitions in the neutron rich sodium isotopes. *Nucl. Phys. A*, 251:193–205, 1975.
- [25] A. Watt, R. P. Singhal, M. H. Storm, and R. R. Whitehead. A shell-model investigation of the binding energies of some exotic isotopes of sodium and magnesium. *J. Phys. G*, 7:L145, 1981.
- [26] A. Poves and J. Retamosa. The onset of deformation at the  $N = 20$  neutron shell closure far from stability. *Phys. Lett. B*, 184:311, 1987.
- [27] Y. Utsuno, T. Otsuka, T. Mizusaki, and M. Honma. Monte carlo shell model calculation for unstable nuclei around  $N = 20$ . *Nucl. Phys. A*, 704:50c–59c, 2002.
- [28] Y. Utsuno, T. Otsuka, T. Mizusaki, and M. Honma. Extreme location of f drip line and disappearance of the  $N = 20$  magic structure. *Phys. Rev. C*, 64:011301(R), 2001.
- [29] B.V. Pritychenko, T. Glasmacher, P.D. Cottle, M. Fauerbach, R.W. Ibbotson, K.W. Kemper, V. Maddalena, A. Navin, R. Ronningen, A. Sakharuk, H. Scheit, and V.G. Zelevinsky. Role of intruder configurations in  $^{26,28}\text{Ne}$  and  $^{30,32}\text{Mg}$ . *Phys. Lett. B*, 461:322, 1999.
- [30] O. Niedermaier, H. Scheit, V. Bildstein, H. Boie, J. Fitting, R. von Hahn, F. Köck, M. Lauer, U. K. Pal, H. Podlech, R. Repnow, D. Schwalm, C. Alvarez, F. Ames, G. Bollen, S. Emhofer, D. Habs, O. Kester, R. Lutter, K. Rudolph, M. Pasini, P. G. Thirolf, B. H. Wolf, J. Eberth, G. Gersch, H. Hess, P. Reiter, O. Thelen, N. Warr, D. Weisshaar, F. Aksouh, P. Van den Bergh, P. Van Duppen, M. Huyse, O. Ivanov, P. Mayet, J. Van de Walle, J. Äystö, P. A. Butler, J. Cederkäll, P. Delahaye, H. O. U. Fynbo, L. M. Fraile, O. Forstner, S. Franchoo, U. Köster, T. Nilsson, M. Oinonen, T. Sieber, F. Wenander, M. Pantea, A. Richter an G. Schrieder, H. Simon, T. Behrens, R. Gernhäuser, T. Kröll, R. Krücken, M. Münch, T. Davinson, J. Gerl, G. Huber, A. Hurst, J. Iwanicki, B. Jonson, P. Lieb, L. Liljeby, A. Schempp, A. Scherillo, P. Schmidt, and G. Walter. “Safe” coulomb excitation of  $^{30}\text{Mg}$ . *Phys. Rev. Lett.*, 94:172501, 2005.
- [31] F. Maréchal, D. L. Balabanski, D. Borremans, J.-M. Daugas, F. de Oliveira Santos, P. Dessagne, G. Georgiev, J. Giovinozzo, S. Grévy, P. Himpe, C. Jollet, I. Matea, G. Neyens, F. Perrot, E. Poirier, O. Roig, M. Stanoiu, C. Stodel, J.-C. Thomas, K. Turzó, and D. Yordanov.  $\beta$  decay of  $^{31}\text{Mg}$ : Extending the “island of inversion”. *Phys. Rev. C*, 72:044314, 2005.
- [32] G. Klotz, P. Baumann, M. Bounajma, A. Huck, A. Knipper, G. Walter, G. Marguier, C. Richard-Serre, A. Poves, and J. Retamosa. Beta decay of  $^{31,32}\text{Na}$  and  $^{31}\text{Mg}$ : Study of the  $N = 20$  shell closure. *Phys. Rev. C*, 47:2502–2516, 1993.

- [33] G. Neyens, M. Kowalska, D. Yordanov, K. Blaum, P. Himpe, P. Lievens, S. Mallion, R. Neugart, N. Vermeulen, Y. Utsuno, and T. Otsuka. Measurement of the spin and magnetic moment of  $^{31}\text{Mg}$ : Evidence for a strongly deformed intruder ground state. *Phys. Rev. Lett.*, 94:022501, 2005.
- [34] Y. Utsuno, T. Otsuka, T. Glasmacher, T. Mizusaki, and M. Honma. Onset of intruder ground state in exotic Na isotopes and evolution of the  $N = 20$  shell gap. *Phys. Rev. C*, 70:044307, 2004.
- [35] H. Iwasaki, T. Motobayashi, H. Sakurai, K. Yoneda, T. Gomi, N. Aoi, N. Fukuda, Zs. Fülöp, U. Futakami, Z. Gacsi, Y. Higurashi, N. Imai, N. Iwasa, T. Kubo, M. Kunibu, M. Kurokawa, Z. Liu, T. Minemura, A. Saito, M. Serata, S. Shimoura, S. Takeuchi, Y.X. Watanabe, K. Yamada, Y. Yanagisawa, and M. Ishihara. Quadrupole collectivity of  $^{28}\text{Ne}$  and the boundary of the island of inversion. *Phys. Lett. B*, 620:118–124, 2005.
- [36] S.W. Padgett, Vandana Tripathi, S.L. Tabor, P.F. Mantica, C.R. Hoffman, M. Wiedeking, A.D. Davies, S.N. Liddick, W.F. Mueller, A. Stolz, and B.E. Tomlin. Spectroscopy of  $^{25}\text{Ne}$  and the  $N = 16$  magic number. *Phys. Rev. C*, 72:064330, 2005.
- [37] J. R. Terry, D. Bazin, B. A. Brown, J. Enders, T. Glasmacher, P. G. Hansen, B. M. Sherrill, and J. A. Tostevin. Absolute spectroscopic factors from neutron knockout on the halo nucleus  $^{15}\text{C}$ . *Phys. Rev. C*, 69:054306, 2004.
- [38] Evaluated nuclear structure data file (ENSDF). <http://www.nndc.bnl.gov/ensdf>.
- [39] P.G. Hansen and J.A. Tostevin. Direct reactions with exotic nuclei. *Annu. Rev. Nucl. Part. Sci.*, 53:219–261, 2003.
- [40] B.A. Brown, P.G. Hansen, B.M. Sherrill, and J.A. Tostevin. Absolute spectroscopic factors from nuclear knockout reactions. *Phys. Rev. C*, 65:061601(R), 2002.
- [41] K. Hencken and G. Bertsch. Breakup reactions of the halo nuclei  $^{11}\text{Be}$  and  $^8\text{B}$ . *Phys. Rev. C*, 54:3043–3050, 1996.
- [42] H. De Vries, C. W. De Jager, and C. De Vries. Nuclear charge-density-distribution parameters from elastic electron scattering. *At. Data and Nucl. Data Tables*, 36:495–536, 1987.
- [43] A. Ozawa, T. Suzuki, and I. Tanihata. Nuclear size and related topics. *Nucl. Phys. A*, 693:32–62, 2001.
- [44] ATIMA. <http://www-linux.gsi.de/weick/atima/>.
- [45] A. Navin, D.W. Anthony, T. Aumann, T. Baumann, D. Bazin, Y. Blumenfeld, B. A. Brown, T. Glasmacher, P. G. Hansen, R. W. Ibbotson, P. A. Lofy, V. Madalena, K. Miller, T. Nakamura, B. V. Pritychenko, B. M. Sherrill, E. Spears, M. Steiner, J. A. Tostevin, J. Yurkon, and A. Wagner. Direct evidence of the breakdown of the  $N = 8$  shell closure in  $^{12}\text{Be}$ . *Phys. Rev. Lett.*, 85:266–269, 2000.

- [46] D.J. Morrissey, B.M. Sherrill, M. Steiner, A. Stolz, and I. Wiedenhoever. Commissioning the a1900 projectile fragment separator. *Nucl. Instr. and Meth. B*, 204:90–96, 2003.
- [47] J. Yurkon, D. Bazin, W. Benenson, D.J. Morrissey, B.M. Sherrill, D. Swan, and R. Swanson. Focal plane detector for the s800 high resolution spectrometer. *Nucl. Instr. and Meth. A*, 422:291–295, 1999.
- [48] D. Bazin, J.A. Caggiano, B.M. Sherrill, J. Yurkon, and A. Zeller. The s800 spectrograph. *Nucl. Instr. and Meth. B*, 204:629–633, 2003.
- [49] W.F. Mueller, J.A. Church, T. Glasmacher, D. Gutknecht, G. Hackman, P.G. Hansen, Z. Hu, K.L. Miller, and P. Quirin. Thirty-two-fold segmented germanium detectors to identify  $\gamma$ -rays from intermediate energy exotic beams. *Nucl. Instr. and Meth. A*, 466:492–498, 2001.
- [50] M. Berz, K. Joh, J.A. Nolen, B.M. Sherrill, and A.F. Zeller. Reconstructive correction of aberrations in nuclear particle spectrographs. *Phys. Rev. C*, 47:537–544, 1993.
- [51] Z. Hu, T. Glasmacher, W.F. Mueller, and I. Wiedenhöver. An automatic energy-calibration method for segmented germanium detectors. *Nucl. Instr. and Meth. A*, 482:715, 2001.
- [52] A.T. Reed, O. Tarasov, R.D. Page, D. Guillemaud-Mueller, Yu.E. Penionzhkevich, R.G. Allat, J.C. Angélique, R. Anne, C. Borcea, V. Burjan, W.N. Catford, Z. Dlouhý, C. Donzaud, S. Grévy, M. Lewitowicz, S.M. Lukyanov, F.M. Marqués, G. Martinez, A.C. Mueller, P.J. Nolan, J. Novák, N.A. Orr, F. Pougheon, P.H. Regan, M.G. Saint-Laurent, T. Siiskonen, E. Sokol, O. Sorlin, J. Suhonen, W. Trinder, and S.M. Vincent. Radioactivity of neutron-rich oxygen, flourine, and neon isotopes. *Phys. Rev. C*, 60:024311, 1999.
- [53] A. Gade, D. Bazin, B.A. Brown, C.M. Campbell, J.A. Church, D.-C. Dinca, J. Enders, T. Glasmacher, P.G. Hansen, Z. Hu, K.W. Kemper, W.F. Mueller, H. Olliver, B.C. Perry, L.A. Riley, B.T. Roeder, B.M. Sherrill, J.R. Terry, J.A. Tostevin, and K.L. Yurkewicz. One-neutron knockout reactions on proton-rich nuclei with  $N = 16$ . *Phys. Rev. C*, 69:134311, 2004.
- [54] P.M. Endt. Strengths of gamma-ray transitions in  $A = 5 - 44$  nuclei, iv. *At. Data and Nucl. Data Tables*, 55:171–197, 1993.
- [55] A. Gade, D. Bazin, C.A. Bertulani, B.A. Brown, C.M. Campbell, J.A. Church, D.C. Dinca, J. Enders, T. Glasmacher, P.G. Hansen, Z. Hu, K.W. Kemper, W.F. Mueller, H. Olliver, B.C. Perry, L.A. Riley, B.T. Roeder, B.M. Sherrill, J.R. Terry, J.A. Tostevin, and K.L. Yurkewicz. Knockout from  $^{46}\text{Ar}$ :  $\ell = 3$  neutron removal and deviations from eikonal theory. *Phys. Rev. C*, 71:051301(R), 2005.
- [56] P. Baumann, Ph. Dessagne, A. Huck, G. Klotz, A. Knipper, G. Marguier, C. Miehé, M. Ramdane, C. Richard-Serre, G. Walter, and B. H. Wildenthal.

- Gamow-teller beta decay of  $^{29}\text{Na}$  and comparison with shell-model predictions. *Phys. Rev. C*, 36:765–773, 1987.
- [57] P. Baumann, Ph. Dessagne, A. Huck, G. Klotz, A. Knipper, Ch. Miehé, M. Ramdane, G. Walter, G. Marguier, H. Gabelmann, C. Richard-Serre, K. Schlösser, and A. Poves. Beta decay of  $^{30}\text{Na}$ , experiment and theory. *Phys. Rev. C*, 39:626–635, 1989.
- [58] G. Audi, A. H. Wapstra, and C. Thibault. The AME2003 atomic mass evaluation (II). tables, graphs and references. *Nucl. Phys. A*, 729:337–676, 2003.
- [59] H. Mach, L.M. Fraile, O. Tengblad, R. Boutami, C. Jollet, W.A. Plóciennik, D.T. Yordanov, M. Stanoiu, M.J.G. Borge, P.A. Butler, J. Cederkäll, Ph. Dessagne, B. Fogelberg, H. Fynbo, P. Hoff, A. Jokinen, A. Korgul, U. Köster, W. Kurcewicz, F. Marechal, T. Motobayashi, J. Mrazek, G. Neyens, T. Nilsson, S. Pedersen, A. Poves, B. Rubio, E. Ruchowska, , and the ISOLDE Collaboration. New structure information on  $^{30}\text{Mg}$ ,  $^{31}\text{Mg}$  and  $^{32}\text{Mg}$ . *Eur. Phys. J. A direct (online only)*, 2005.
- [60] A.E.L. Dieperink and T. de Forest. Center-of-mass effects in single-nucleon knock-out reactions. *Phys. Rev. C*, 10:543–549, 1974.
- [61] A. Gade, D. Bazin, B.A. Brown, C.M. Campbell, J.A. Church, D.-C. Dinca, J. Enders, T. Glasmacher, P.G. Hansen, Z. Hu, K.W. Kemper, W.F. Mueller, H. Olliver, B.C. Perry, L.A. Riley, B.T. Roeder, B.M. Sherrill, J.R. Terry, J.A. Tostevin, and K.L. Yurkewicz. Reduced occupancy of the deeply bound  $0d_{5/2}$  neutron state in  $^{32}\text{Ar}$ . *Phys. Rev. Lett.*, 93:042501, 2004.